ABRUPT THAW AND THE PERMAFROST CARBON FEEDBACK

By Heidi Greimel Rodenhizer

A Dissertation

Submitted in Partial Fulfillment

of the Requirements for the Degree of

Doctor of Philosophy

in Biology

Northern Arizona University

May 2022

Approved:

Ted Schuur, Ph.D., Chair

Michelle Mack, Ph.D.

Scott Goetz, Ph.D.

Temuulen Sankey, Ph.D.

ABSTRACT

ABRUPT THAW AND THE PERMAFROST CARBON FEEDBACK

HEIDI GREIMEL RODENHIZER

Air temperatures in the Arctic are rising more than two times faster than the global average (IPCC, 2021), and this is causing permafrost to thaw both gradually, with incremental increases in ALT, and abruptly, with rapid collapse of ice-rich permafrost ground forming discrete thermokarst features. When permafrost carbon that has been frozen for years to thousands of years thaws, it becomes susceptible to microbial respiration and release to the atmosphere as greenhouse gases. This depends, in part, on how much of the permafrost region will undergo abrupt thaw and how susceptible abruptly thawed permafrost carbon is to respiration, as hydrology can shift rapidly with abrupt thaw and lead to conditions more or less suited to plant growth, ecosystem respiration, and methanogenesis. This dissertation investigated the rate of ground subsidence and the impact it has on thawed permafrost carbon stocks, the extent and morphology of abrupt thaw in a warming tundra ecosystem and the role it plays in CO_2 and CH_4 release to the atmosphere at the landscape scale, and the fine scale responses of hydrology to abrupt thaw and how this determines the spatial heterogeneity of CO_2 fluxes. In a permafrost warming experiment, subsidence of up to ~1 m per decade masked the full rate of permafrost thaw and was responsible for doubling the rate of carbon thaw. On the landscape as a whole, abrupt thaw covered 7% of the landscape, with the largest extent being due to water tracks. On an annual scale, abrupt thaw resulted in higher CO_2 and CH_4 release, although CO_2 uptake was higher during the growing season. This highlights the importance of winter emissions in determining tundra carbon balance, particularly when and where abrupt thaw occurs.

Additionally, abrupt thaw caused diverging hydrologic regimes, with the most deeply subsided regions becoming consistently wet and adjacent areas of high relief becoming intermittently dry and wet. Both growing season GPP and R_{eco} were higher in intermittently dry and wet areas, while they were suppressed in the consistently wet areas, relative to areas which did not undergo abrupt thaw, but it is likely that both hydrologic regimes resulted in higher carbon release at the annual scale. Because abrupt thaw could result in emissions of about the same magnitude as gradual thaw over the next century, it is important that abrupt thaw be considered in Earth System Models and climate agreements.

ACKNOWLEDGMENTS

I would like to thank my committee and mentors Ted, Michelle, Scott, and Teki for their guidance and support throughout my PhD journey. They provided invaluable feedback at every step of the research process from developing questions and designing research projects to editing manuscripts. I would not be the scientist I am today without them. Thanks also to the PIs of the 2013 Polaris Project, who are at least partly responsible for setting me on this research journey: Sue Natali, Andy Bunn, John Schade, and Paul Mann. The welcoming and supportive environment they created played an important role in my decision to pursue Arctic research. I also received much help from my friends in the Schuur laboratory, Christina Schädel, Marguerite Mauritz, Meghan Taylor, Gerardo Celis, Erin Trochim, Craig See, Chris Ebert, Justin Ledman, Elaine Pegoraro, Emily Romano, Krystin Hill, AJ Garnello, Allison Kelley, Stephanie Kadej, and Emma Lathrop. You all made my time at NAU more enjoyable and have been immeasurably helpful in navigating graduate school. Special thanks to Julia Stuart and Haley Dunleavy, who sat next to me in the lab every day until Covid, provided entertaining breaks from work, went skiing, hiking, and climbing with me, and were generally awesome friends. And, of course, none of this would have been possible without the love and support of my husband, Chris Keefe; parents, Dave and Debbie Rodenhizer; brother, Brett Rodenhizer, and the rest of my family.

TABLE OF CONTENTS

LIST OF TABLES

LIST OF FIGURES

PREFACE

The chapters included in this dissertation are formatted for publication in scientific peer-reviewed journals. The first chapter is a general introduction which provides the scientific framework of the dissertation. The second chapter, “Carbon thaw rate doubles when accounting for subsidence in a permafrost warming experiment”, was published in the Journal of Geophysical Research: Biogeosciences in 2020. The third chapter, “Abrupt permafrost thaw accelerates carbon dioxide and methane release at a tussock tundra site”, is formatted for submission to Arctic, Antarctic, and Alpine Research. The fourth chapter, “Divergent Hydrologic Responses to Abrupt Permafrost Thaw Drive Spatially Heterogeneous Carbon Dioxide Fluxes”, is formatted for submission to Global Change Biology. The fifth chapter is a combined discussion of the results and conclusions of all chapters. Some redundancy will result from combining these manuscripts within the university formatting requirements.

CHAPTER 1: INTRODUCTION

Arctic air temperature is rising twice as fast as the global mean rate (Overland et al. 2016), thawing permafrost. Permafrost is ground that is <0°C for at least two consecutive years, but often permafrost soils have been frozen for thousands of years (Schuur & Mack, 2018). Permafrost soils contain between 1460 and 1600 Pg of C across the circumpolar region, because decomposition is limited by sub-zero temperatures, allowing the slow accumulation of organic matter from plants and animals (Hugelius et al., 2014; Schuur et al., 2015, 2018), and this is about twice as much carbon as contained in the atmosphere (Houghton, 2007). As permafrost thaws, decomposition of these organic carbon stores will lead to greenhouse gas emissions that will exacerbate human-caused climate change (Schuur et al., 2015). However the magnitude, rate, and the form of future permafrost carbon emissions is an area of ongoing research. The magnitude, rate and form of permafrost carbon emissions are controlled by the balance between gross primary production (GPP; carbon dioxide uptake by photosynthesis) and ecosystem respiration (R_{eco}; carbon dioxide release through autotrophic and heterotrophic respiration), which depends on the size of the unfrozen carbon pool and the environmental conditions (i.e. hydrology and oxygen availability) to which soil organic matter is exposed (Schuur et al., 2018). This is a complex area of research that has been difficult to incorporate into Earth System models (Olefeldt et al. 2016, Turetsky et al. 2020), however, a better understanding is needed in order to inform climate change policy (Natali et al. 2021).

Permafrost temperatures are warming due to climate change (Osterkamp, 2007; Osterkamp & Romanovsky, 1999), and this is causing gradual permafrost thaw, or a deepening of the seasonally thawed active layer (Nyland et al., 2021; Turetsky et al., 2020). As the active layer deepens, soil C that has been frozen for long periods of time is thawed, allowing it to decompose

and enter the modern carbon cycle (Hayes et al., 2014; Lee et al., 2010). However, at the same time, deeper ALT exposes additional nutrients which can stimulate plant growth (Salmon et al., 2016; Schuur et al., 2007). Plant productivity in the Arctic, especially that of shrubs, has increased through time, as observed by increases in the normalized difference vegetation index (NDVI; a measure of plant "greenness") from the satellite record (Berner et al., 2020; Bunn & Goetz, 2006; Goetz et al., 2005) and field studies which show that increasing temperature and nutrient availability stimulates plant productivity (DeMarco et al., 2014; Natali et al., 2011; Schuur et al., 2007). Although there is still uncertainty about whether increased GPP might be able to offset respiration of old permafrost carbon in the future, most lines of evidence point to increasing carbon emissions from permafrost ecosystems as the active layer deepens (Schuur et al., 2018).

The relationship between permafrost thaw and carbon release is further complicated by a process known as abrupt thaw or thermokarst (Olefeldt et al., 2016; Turetsky et al., 2020). Much of the volume of permafrost can be composed of ice, and as the active layer deepens, this ice melts and the ground surface subsides, forming depressions (Kokelj & Jorgenson, 2013). Once initiated, thermokarst features can thaw very rapidly due to internal feedbacks (Farquharson et al., 2019; Jorgenson et al., 2020; Shur & Jorgenson, 2007). One such feedback is thermoerosion, which is the combined impact of heat flow and mechanical erosion by flowing water (Kokelj et al., 2009; Kokelj & Jorgenson, 2013; Morgenstern et al., 2021). Another internal feedback is increased heat transfer through ponding or disturbance to insulating layers of plants or organic matter can increase heat transfer (Kokelj & Jorgenson, 2013). The environmental disturbance which occurs in thermokarst features has implications for carbon cycling (Schuur et al., 2008). Disturbance to plants and eventual succession, rapid mobilization of carbon and nutrients from

permafrost, and water-logging are some examples of environmental changes that impact carbon fluxes (Cassidy et al., 2016; Euskirchen et al., 2017; Lee et al., 2011; Schuur et al., 2007; Vogel et al., 2009).

Hydrologic shifts following abrupt thaw will play a large role in determining the form of permafrost C release. Carbon in permafrost soils can be released both as CO_2 and as CH_4 when decomposition occurs, with dry soils releasing C primarily as CO_2 and waterlogged soils releasing C as both CO_2 and CH_4 (Harden et al., 2012; Schädel et al., 2016). Since CH_4 is 34 times more powerful a greenhouse gas than CO_2 over a 100-year timescale (Myhre et al., 2014), waterlogged soils which release less total C than dry soils can still have a stronger impact on the climate through the strong greenhouse forcing of CH_4 relative to CO_2 (Taylor et al., 2018). Because of this, the relative contribution of CO_2 and CH_4 to total permafrost C release will be important in determining the magnitude of the permafrost C feedback (Schuur et al., in review).

The purpose of this dissertation research was to investigate the impact of abrupt thaw on carbon fluxes from the plot-scale to the landscape-scale in three research projects. In the first research project (Ch. 2 of the dissertation), subsidence was quantified at CiPEHR using GPS and the impact of subsidence on both the depth to permafrost and the rate of permafrost carbon thaw was determined. In the second research project (Ch. 3 of the dissertation), thermokarst features were mapped across an 81 km^2 site using a novel algorithm which can identify depressions from a single elevation image and this classification was combined with carbon fluxes measured by eddy covariance to determine the impact of abrupt thaw on ecosystem carbon balance. Finally, in the third research project (Ch. 4 of the dissertation), the spatial nature of abrupt thaw, hydrologic changes, and carbon dioxide fluxes were investigated using chamber based measurements of carbon dioxide fluxes at CiPEHR.

This work was done at a permafrost warming experiment and nearby natural thaw gradient near Eight Mile Lake (EML) in Healy, AK. The Carbon in Permafrost Experimental Heating Research (CiPEHR) is a soil and air warming experiment established in 2008, which was designed to simulate future climate change (Natali et al., 2011). Soil temperatures have been passively warmed every winter using snow fences which increase snow depth and insulate soils from winter air temperatures well below 0°C, and air temperatures have been warmed during the growing season using clear, open-top chambers. The plots were monitored extensively for changes in environmental conditions, plant biomass, and carbon dioxide fluxes throughout the growing season every year through 2021. At the natural thaw gradient, there are three sites with different abrupt thaw histories, minimal thaw (no thermokarst formation), moderate thaw (thermokarst began in ~1985), and extensive (thermokarst began prior to 1951), which have been monitored since 2003 (Schuur et al., 2007). An eddy-covariance tower located near the thaw gradient has been used to monitor carbon dioxide and methane fluxes and has a footprint that spans areas with and without thermokarst features. Additionally, the National Ecological Observatory Network (NEON) began monitoring a site ~1 km from CiPEHR in the summer of 2017, including collecting airborne LiDAR data and high-resolution imagery.

CHAPTER 2: CARBON THAW RATE DOUBLES WHEN ACCOUNTING FOR SUBSIDENCE IN A PERMAFROST WARMING EXPERIMENT

Heidi Rodenhizer[1], Justin Ledman[1,2], Marguerite Mauritz [1]*, Susan M. Natali[3], Elaine Pegoraro[1], César Plaza[4], Emily Romano[1], Christina Schädel[1,5], Meghan Taylor[1]†, Edward Schuur[1]

[1] Northern Arizona University, Center for Ecosystem Science and Society, Flagstaff, AZ, USA.

[2] Bonanza Creek Long Term Ecological Research Site, University of Alaska, Fairbanks, AK, USA.

[3] Woods Hole Research Center, Falmouth, MA.

[4] Instituto de Ciencias Agrarias, Consejo Superior de Investigaciones Científicas, 28006 Madrid, Spain.

[5] Northern Arizona University, School of Informatics, Computing, and Cyber Systems, Flagstaff, AZ, USA.

Corresponding author: Heidi Rodenhizer (hgr7@nau.edu)

*Current address: University of Texas at El Paso, Biology Department.

†Current address: Yale University, School of Forestry & Environmental Studies, New Haven, CT.

Key Points:

- Subsidence causes a shifting reference frame for measurements of permafrost thaw
- The rate of permafrost carbon thaw doubles when subsidence is accounted for
- Subsidence of up to 6 cm yr^{-1} was observed in a permafrost warming experiment, due to both ice and soil loss

Abstract

Permafrost thaw is typically measured with active layer thickness, or the maximum seasonal thaw measured from the ground surface. However, previous work has shown that this measurement alone fails to account for ground subsidence and therefore underestimates permafrost thaw. To determine the impact of subsidence on observed permafrost thaw and thawed soil carbon stocks, we quantified subsidence using high-accuracy GPS and identified its environmental drivers in a permafrost warming experiment near the southern limit of permafrost in Alaska. With permafrost temperatures near 0°C, 10.8 cm of subsidence was observed in control plots over 9 years. Experimental air and soil warming increased subsidence five-fold and created inundated microsites. Across treatments, ice and soil loss drove 85-91% and 9-15% of subsidence, respectively. Accounting for subsidence, permafrost thawed between 19% (control) and 49% (warming) deeper than active layer thickness indicated, and the amount of newly thawed carbon within the active layer was between 37% (control) and 113% (warming) greater. As additional carbon thaws as the active layer deepens, carbon fluxes to the atmosphere and lateral transport of carbon in groundwater could increase. The magnitude of this impact is uncertain at the landscape scale, though, due to limited subsidence measurements. Therefore, to determine the full extent of permafrost thaw across the circumpolar region and its feedback on the carbon cycle, it is necessary to quantify subsidence more broadly across the circumpolar region.

Plain Language Summary

Permafrost soils, which are perennially frozen soils found throughout cold regions, contain vast quantities of carbon and ice. When permafrost thaws, carbon can be lost to the atmosphere, contributing to climate change. This means it is important to track permafrost thaw,

which is often done using active layer thickness, or the depth of the seasonally thawed surface layer of soil. However, ice volume can be lost from thawing permafrost, causing the soil surface to drop. Conventional measurements do not account for this surface drop and the rate of thaw could therefore be underestimated. We found that experimentally warmed soils dropped at a rate of 6 cm per year, mostly due to loss of ice volume, but also due to the loss of soil mass. When accounting for the change in soil surface height over time, the full depth of permafrost thaw was 49% greater. The increased depth of thaw resulted in more than twice as much carbon being thawed as was estimated with standard methods that did not account for subsidence. These findings suggest that permafrost is thawing more quickly than long-term records indicate, and that this could result in additional carbon release contributing to climate change.

1. Introduction

Arctic temperatures are rising about 2.5 times faster than the global average (IPCC, 2013), and experimental evidence shows that this is causing permafrost ecosystems to shift from an atmospheric carbon (C) sink to a C source (Belshe et al., 2013; Commane et al., 2017; Euskirchen et al., 2017; Schuur & Mack, 2018). Much of the Arctic is underlain by permafrost soils, where freezing conditions have maintained a slow but consistent C sink by protecting soil C from microbial respiration for up to thousands of years (Hicks Pries et al., 2012; Schuur et al., 2015; Tarnocai et al., 2009; Zimov et al., 2006). Permafrost soils contain 1440-1600 Pg C globally (Schuur et al., 2018), which is about twice as much C as is in the atmosphere (Houghton, 2007). However, rapidly increasing temperatures in the Arctic have begun to thaw permafrost and alter ecosystem C balance, determined from the relative contributions of plant production and ecosystem respiration. While plant productivity is expected to increase under future climate change, changes in microbial respiration are likely to be an order of magnitude

higher, causing permafrost ecosystems to shift to a C source over the next century (Belshe et al., 2013; Schuur et al., 2018).

Active layer thickness (ALT), the depth of seasonal permafrost thaw, has been closely monitored as one of the key variables for understanding the impact of climate change on permafrost thaw and ecosystem C dynamics (Brown et al., 2000; Nixon & Taylor, 1998). ALT plays an important role in regulating the response of plant production and respiration to climate change in the Arctic. As the region warms, ALT tends to increase (Brown et al., 2000; Romanovsky et al., 2003; Shiklomanov et al., 2012; Streletskiy et al., 2008), thawing both C and nutrients (Salmon et al., 2018). Greater access to nitrogen can increase plant growth (Chapin et al., 1995; Shaver et al., 1992), while increasing C availability to microbes increases respiration of C that had been thermally protected from decomposition (Hicks Pries et al., 2013; Hicks Pries et al., 2016). Therefore, the Circumpolar Active Layer Monitoring (CALM) network was established to track changes in ALT and near surface permafrost at over 200 sites (Brown et al., 2000).

Permafrost thaw also induces physical changes to the soil profile, impacting its structural stability by causing the ground to compact and subside (Kokelj & Jorgenson, 2013). It is widely accepted that subsidence occurs as permafrost soils thaw, and ice volume is lost (Jorgenson & Osterkamp, 2005; Kokelj & Jorgenson, 2013; Nelson et al., 2001), because permafrost soils contain up to 80% ice by volume (Schuur et al., 2008). Depending on the distribution of ice across the landscape, and other environmental factors including local topography, the morphology of subsidence can vary considerably (Jorgenson & Osterkamp, 2005; Kokelj & Jorgenson, 2013). Many types of thermokarst occurring in soils with high and variable ice content result in highly visible disturbances, including thaw slumps and thermokarst lakes, pits,

and gullies (Jones et al., 2012; Jorgenson & Osterkamp, 2005; Ward Jones et al., 2019). These thermokarst features occur in areas estimated to cover ~20% of the circumpolar region (Olefeldt et al., 2016). However, in soils with relatively low to medium ice content, particularly rocky or gravelly areas, thaw can lead to more gradual, nonpatterned subsidence (Jorgenson & Osterkamp, 2005), which has also been termed isotropic subsidence (Shiklomanov et al., 2013; Streletskiy et al., 2017). Nonpatterned subsidence, due to the lack of visually obvious features, is more challenging to detect without monitoring elevation changes (Jorgenson & Osterkamp, 2005; Shiklomanov et al., 2013). It is also conceivable that areas of recent or gradual permafrost thaw could appear to be nonpatterned to observers on the ground, as subsidence may not have progressed sufficiently to be visible. The combined extent of gradual and nonpatterned subsidence is unknown because elevation change is not monitored extensively in permafrost regions, but due to recent, rapidly changing temperatures in the Arctic, it is potentially broad.

Soil loss could also contribute to subsidence through the release of C to the atmosphere and lateral transport of C in water, if losses are high enough to significantly decrease the volume of organic matter within the soil profile. A significant contribution of peat loss to subsidence has been shown previously in a drained ombrotrophic bog (Grønlund et al., 2008), but to the best of our knowledge, no studies have previously attempted to quantify the impact of soil loss on subsidence in permafrost ecosystems, so it is uncertain whether currently observed rates of soil loss are sufficient to decrease soil volume at a detectable level. However, both release of C to the atmosphere and export in water tend to be higher in areas of thermokarst than in adjacent, undisturbed areas (Abbott & Jones, 2015; Abbott et al., 2015; Cassidy et al., 2016; Euskirchen et al., 2017), meaning that these areas should be the first to show the effect of soil loss on subsidence.

Subsidence is rarely quantified when monitoring permafrost thaw, and this is problematic because long-term measurements of ALT have been shown to underestimate the rate of permafrost thaw (Shiklomanov et al., 2013; Streletskiy et al., 2017; O'Neill et al., 2019). The typical method of monitoring ALT is to insert a metal probe into the ground until it hits permafrost and measure the distance from the soil surface to the bottom of the probe (Hinkel & Nelson, 2003). However, long-term monitoring in some areas has shown little to no change in ALT despite increases in air and permafrost temperatures (O'Neill et al., 2019; Shiklomanov et al., 2013; Streletskiy et al., 2017). Subsidence can explain the lack of change in ALT, as it causes a changing reference frame for ALT probe measurements through time, thereby masking the full depth of thaw (O'Neill et al., 2019; Shiklomanov et al., 2013; Streletskiy et al., 2017). Therefore, relying solely on ALT as a measure of permafrost thaw is also likely to underestimate the amount of soil C being mobilized in permafrost. To account for this discrepancy, some studies have used thaw tubes to measure thaw penetration, the sum of subsidence and ALT (Nixon & Taylor, 1998), however, most studies still rely on ALT without accounting for subsidence.

Subsidence drastically alters the hydrologic conditions within the active layer (Hinkel & Hurd, 2006; Johansson et al., 2013; O'Neill & Burn, 2017), and thereby regulates the fate of permafrost C upon thaw. In Earth System models, permafrost thaw results in drier soils as the permafrost table drops and drainage is increased (Schädel, Koven, et al., 2018), however, experimental data show that subsidence often results in wetter soils and the formation of ponds or lakes, at least in the short term (Hinkel & Hurd, 2006; Johansson et al., 2013; Jorgenson et al., 2013; Mauritz et al., 2017). Wetter conditions increase soil temperatures and accelerate thaw through the high latent heat of water (Subin et al., 2013), and anaerobic conditions in saturated soils cause more C to be released as methane (CH_4) rather than carbon dioxide (CO_2) (Blanc-

Betes et al., 2016; Johnston et al., 2014; Kutzbach et al., 2004; Taylor et al., 2018). Although anaerobic conditions simultaneously slow the rate of decomposition, the increased production of CH_4, which is 45 times more powerful a greenhouse gas than CO_2 over a 100-year timescale (Myhre et al., 2013), more than outweighs the lower rates of C release (Schuur et al., 2008; Taylor et al., 2018). Therefore, both the magnitude and form of C release depend upon how hydrologic conditions develop as permafrost thaws and the ground subsides.

Here we quantified subsidence and thaw penetration over nine years at a permafrost warming experiment near Healy, AK. This site is located within the discontinuous permafrost zone where permafrost temperatures are near 0°C, providing ideal conditions to investigate the impact of experimental warming on subsidence, permafrost thaw, and C dynamics. The overall goal of this study was to determine the factors that drive subsidence and the impact of subsidence on permafrost thaw and the permafrost C feedback to climate. We specifically aimed to determine 1) the amount of subsidence which occurred over 9 years of permafrost warming and the impact of air and soil warming on this process, 2) the relative contributions of ice loss and soil loss to subsidence, and 3) the impact of using thaw penetration, rather than ALT, on estimates of C exposure in the deepening active layer. We hypothesized that 1) soil warming would accelerate subsidence over control conditions, but that air warming would not alter soil temperature sufficiently to impact the rate of subsidence, 2) ice loss would be responsible for nearly all of the observed subsidence and the impact of soil loss on subsidence would be too small to detect, even in areas of thermokarst, and 3) using thaw penetration rather than ALT would increase the estimate of recently thawed C in the active layer by a large margin, because previously observed rates of both subsidence in degrading permafrost and ALT expansion into the permafrost are on the order of centimeters per year.

2. Study Site

The Carbon in Permafrost Experimental Heating Research (CiPEHR) site is located near Healy, Alaska, USA just outside Denali National Park (WGS84, 63°52’59”N, 149°13’32”W). The site is underlain by permafrost owing to the elevation of the foothills of the Alaska Range (670 m, Geoid 12B). The mean annual temperature is -0.94°C with a non-summer (Oct.-Apr.) average temperature of -10.09°C, and a summer (May-Sept.) average temperature of 11.91°C (Healy and McKinley Stations, Western Regional Climate Center and NOAA National Centers for Environmental Information) (Mauritz et al., 2017). The ecosystem is classified as moist acidic tussock tundra, with the predominant vegetation types being the tussock forming *Eriophorum vaginatum* and the deciduous shrub, *Vaccinium uliginosum* (Salmon et al., 2016; Schuur et al., 2007). Soils are Gelisols, with an organic layer of approximately 0.35 m above cryoturbated mineral soils that are composed of glacial till and windblown loess (Natali et al., 2011; Plaza et al., 2017).

CiPEHR was established in 2008 to study ecosystem C responses to rising Arctic temperatures by experimentally warming both soil and air temperatures (Natali et al., 2011). Six snow fences 1.5 m tall and 8 m long were set up every winter in three replicate blocks (A, B, C) that contain two fences, each 5 m apart (Figure 1). The snow fences trap snow on the leeward side, insulating the ground from very cold winter temperatures. Snow depth on the soil warming side typically reached the height of the snow fences by mid-winter, regardless of the ambient snow depth in any particular year (Figure 2). Snow was removed each April to avoid additional water input and delayed snow melt. At each snow fence, four 0.36 m^2 plots were located on the soil warming side and four plots were located on the control side. Additionally, two of the four plots on either side of the fence received air warming using 0.5 m tall clear polycarbonate open

top chambers which were placed over the plots throughout each summer season. After the first two years, deep soil (20 and 40 cm) temperatures remained an average of 0.78°C warmer in soil warming plots throughout the summer season (Mauritz et al., 2017; Natali et al., 2011). By 2015, after 7 years of treatment, soil warming had resulted in a non-summer season increase of 1.49°C in surface soil temperatures (5 and 10 cm) and 1.05°C in deep soil temperatures (20 and 40 cm) (Mauritz et al., 2017). On average, air warming increased air temperatures by 0.3°C during the first summer season and likely does not cause significant soil warming (Natali et al., 2011).

3. Materials and Methods

3.1. Elevation Measurements and Subsidence Calculation

Subsidence was estimated as the change in elevation derived from high-accuracy GPS measurements (Rodenhizer et al., 2019a). We measured elevation at each experimental block at 2 m intervals in an approximately 30x30 m grid in 2009, 2011, and each of 2015-2018 using a Trimble high-resolution differential global position system (dGPS) with real time kinematic correction. A base station was placed at a United States Geological Survey geodetic marker (WGS84, 63.88793°N, 149.2383°W) <1 km from CiPEHR in order to continuously correct for atmospheric disturbances. Each elevation grid point was measured for 3-5 seconds on top of the moss layer. In 2009 and 2011, post-processing was completed with a methodology developed by UNAVCO using Trimble Geomatics Office (Dayton, Ohio). Beginning in 2015, post-processing was completed using a more highly automated methodology developed by the National Park Service using Trimble Business Center (Sunnyvale, California). Trimble Business Center replaced Trimble Geomatics Office when it was discontinued, necessitating a new processing protocol and, despite the shift to a new software platform and a more highly automated protocol, the underlying processing methodology was the same. We transformed all GPS data to the

Alaska Zone 4 State Plane coordinate system with the GRS80 ellipsoid and geoid 12B. We interpolated elevation surfaces using the gstat package (Gräler et al., 2016; Pebesma, 2004) in R (R Core Team, 2018) by building exponential models of empirical semivariograms and interpolating between the points using anisotropic kriging in two directions (across- and down-slope) (Bivand et al., 2008). Standard error of kriging was calculated for each cell and is reported with subsidence values (Figure S1). Subsidence was calculated from the elevation surfaces relative to 2009 using the raster package (Hijmans, 2019). Subsidence for years missing GPS points was interpolated linearly cell-by-cell.

GPS accuracy of individual points was very high, although inconsistencies in data collection may have impacted the accuracy of subsidence. GPS accuracy was measured with two checkpoints located within a few meters of the base station and measured for 2 minutes continuously. GPS horizontal accuracy averaged 0.010 m and vertical accuracy averaged 0.0016 m, however, GPS points were not measured in consistent locations throughout the years of sampling. Through 2016, the grid points were set up by hand using a measuring tape, meaning that points were measured in slightly different locations from year to year. The roughness of the tundra vegetation surface means that elevation can differ by tens of centimeters at points that are only slightly offset from one another, and this could contribute variability to the final subsidence product. For example, sample semivariograms of the raw elevation data indicate that points separated by ~1 m differ by 5-7 cm on average, with certain pairs of points differing by nearly 1 m. In 2017 we realized the potential impact of this data collection method, and from 2017 on, the grid points were loaded onto the GPS ahead of time to allow quick navigation to the same point year after year. It is impossible to estimate the error associated with gap filling elevation in years without GPS data, as the cell-by-cell interpolation does not build linear models with all of the

available data points, but rather fills in missing values by drawing a line through the two closest (temporally) non-missing data points. However, we expect that the error introduced by this step is insignificant relative to the error introduced by the varying offset of GPS points from one year to another.

3.2. Active Layer Thickness and Water Table Depth

Changes in permafrost thaw and hydrologic conditions were characterized with ALT and water table depth measurements between 2009 and 2018. Thaw depth was measured at each of the plots by inserting a metal probe into the ground until it hit frozen soil and ALT was quantified as the thaw depth in mid-September (week 36 of the year) at maximum depth of thaw (Natali & Schuur, 2012; Natali et al. 2012; Pegoraro et al., 2019). Water table depth, the depth to ground water, was measured within PVC lined wells three times a week during the summer season (Schädel, Mauritz, et al., 2018). Between 2009 and 2012, water table depth was measured within two water wells on each side of the snow fences, and between 2013 and 2018, within three water wells on each side of the snow fences.

3.3. Soil Cores

We collected soil cores in May 2009 to measure ice and C content prior to experimentally induced permafrost thaw (Plaza et al., 2017). Two cores were taken per fence, one on the soil warming side and one on the control side. The thawed surface layer (~15 cm) was collected using a serrated knife and the frozen ground underneath was cored using a Tanaka drill with a 7.6 cm diameter hollow bit until gravel halted progress (~85 cm). Cores were stored frozen until processing in the laboratory. The surface vegetation was clipped to the bottom of the green moss, and cores were sectioned in a 5 cm increment at the surface, and 10 cm increments thereafter. Each depth increment was subsampled for moisture content, bulk density, and C content (Hicks

Pries et al., 2012; Pegoraro et al., 2019). Soil gravimetric water content was measured as the water mass over the wet soil mass (g H_2O g Wet $Soil^{-1}$), because using the wet soil mass in gravimetric water content determination performs better in ice-rich mineral soils (Phillips et al., 2015). Bulk density of dry soil was calculated as the mass of a soil sample of known volume (i.e. the total core volume for the section of core, including ice and rocks, as derived from the core dimensions; g cm^{-3}) separated from the mass and volume of rocks. Carbon content was determined using an elemental combustion analyzer (used to combust the samples; ECS4010, Costech Analytical Technologies, Inc., Valencia, CA, USA) coupled with an isotope ratio mass spectrometer (used to measure the C content; Delta V advantage, Thermo Scientific Inc., Waltham, MA, USA).

3.4. Soil Core Calculations

We combined GPS measurements with data on ice and C content from the soil cores to determine the role subsidence has in the quantification of permafrost thaw, as well as the potential driving factors of subsidence. Using the tidyverse package (Wickham, 2017) within R (R Core Team, 2018), we accounted for the effect that the shift in soil surface height had on ALT measurements, calculated the total amount of bulk soil C thawed over the study period, and partitioned total subsidence into the contributions from loss of ice and loss of soil.

To determine the full depth of permafrost thaw over the course of the experiment, we calculated thaw penetration as:

$$ThawPenetration = ALT + Subsidence \quad \text{Eq. 1}$$

where ALT is the depth of thaw during week 36 of the year (late August or early September) and subsidence is the cumulative interannual subsidence through the date of ALT probing (2009-20xx). To determine the cumulative interannual subsidence for each plot in each year, we

extracted the value of subsidence in each year from the kriged surface at the location of each plot (Rodenhizer et al., 2019b). We calculated the amount of bulk soil C that thawed between 2009 (initial) and each following year (final) as the sum of C content at depths between the initial and final thaw penetration (Figure S2). Carbon content from 2009 was used so that the initial quantity of C in the permafrost was accounted for, even though some of the C that thawed between 2009 and the end of the experiment was lost following thaw, either to the atmosphere or laterally in water. This calculation was repeated using ALT and the difference between the two calculations was taken in order to determine the impact of accounting for subsidence on the magnitude of C exposure upon permafrost thaw.

Potential subsidence due to ice loss was determined by calculating the volume of ice divided by the soil core area (ice height) from the soil cores taken in 2009 (representing initial conditions prior to warming). This calculation was based on the volume of ice contained in thawed permafrost, which was considered to be the layer of soil between the initial (2009) thaw penetration and the final (2013 or 2018) thaw penetration (Figure S2). We used final values of both 2013 and 2018, because many of the soil cores were only deep enough to reach the depth of 2013 thaw penetration. We calculated the volume of ice which can contribute to subsidence in two different ways to determine a maximum and minimum value of potential subsidence. The volume of ice for the maximum value was calculated using the total ice content, and should be an overestimate of potential subsidence, because a significant portion of permafrost ice should exist within soil pores that will not collapse upon ice loss (Kokelj & Burn, 2003). The minimum value included only the estimated ice volume associated with excess ice (total ice – pore ice) and should theoretically be a closer estimate of potential subsidence.

To calculate the maximum potential subsidence due to ice loss, we had to first calculate the total mass of ice within the thawed permafrost. We started with the equation for gravimetric water content:

$$GWC(\%) = \frac{WaterMass(g)}{SoilMass(g) + WaterMass(g)} \quad \text{Eq. 2}$$

and replaced water mass with ice mass because, at the time of coring, all of the water content of the thawed permafrost layer was frozen in permafrost. We then rearranged equation 2 to solve for ice mass:

$$IceMass(g) = GWC(\%) * \quad \text{Eq. 3}$$

where BD is the average bulk density of the thawed permafrost layer. Finally, the total ice height was calculated from the ice mass calculated in equation 3:

$$TotalIceHeight(m) = \frac{IceMass(g) * 0.92\left(\frac{cm^3}{g}\right)}{100\left(\frac{cm}{m}\right) * SoilCoreArea(cm^2)} \quad \text{Eq. 4}$$

where 0.92 is the density of ice, and the whole equation is divided by 100 to convert from cm to m.

To remove the possibility of overestimating potential subsidence by including pore ice volume in the calculation, we partitioned the total ice height into components of pore ice and excess ice. As excess ice content was not measured following Kokelj & Burn (2003) when soil samples were originally taken, we instead estimated the excess ice by assuming the pore space of these soils is 50% of the soil volume (Text S1). This value was chosen because soils at a similar site ~1 km SE of CiPEHR are silt loam soils based on sand, silt, and clay percentages (NEON, 2017b), and silt loam soils are estimated to have 50% pore space (Brady & Weil, 2008). Any ice

which did not fit into the estimated pore space was assumed to be excess ice and was included in the calculation of potential subsidence (Figure S3):

$$ExcessIceHeight(m) = \frac{ExcessIce(cm^3)}{100\left(\frac{cm}{m}\right) * SoilCoreArea(cm^2)} \quad \text{Eq. 5}$$

where excess ice was calculated using equations S1-S4 and the soil core area was calculated from the diameter of the soil core.

To determine the contribution of soil loss to subsidence, we estimated the volume of organic soil from which measured C losses derived. Minimum and maximum C losses were estimated from previously published values derived from eddy covariance near CiPEHR (sum of CO_2 and CH_4 fluxes) or soil core measurements at CiPEHR, respectively (Plaza et al., 2019; Taylor et al., 2018). Eddy covariance towers are used to measure C fluxes at the landscape scale and, therefore, incorporate fluxes from varied microsites (Belshe et al., 2012). The eddy covariance tower is located ~1 km from CiPEHR and averages C fluxes in a footprint with a radius of approximately 200-350 m (Celis et al., 2017). Although the eddy covariance tower does not measure fluxes at CiPEHR, the vegetation composition, elevation, aspect, and C flux dynamics are very similar at both sites (Celis et al., 2017). At this site, CO_2 fluxes from eddy covariance are lower than those measured from soil cores, likely in part because eddy covariance measurements do not account for loss of C through lateral transport in ground water (Plaza et al., 2019). However, the C loss estimate from soil cores is about twice as large as that from eddy covariance, indicating a large lateral flux of C in water that has not been verified through other methods. Therefore, we used both estimates to constrain C flux estimates, with eddy covariance data as the lower bound and soil core data as the upper bound.

The potential height of soil previously occupied by lost C was calculated as:

$$SoilHeight(m) = \frac{CLoss\left(\frac{g}{m^2 * yr}\right)}{CContent\left(\frac{gC}{gsoil}\right) * BD\left(\frac{g}{m^3}\right)} * 9(yrs) \qquad \text{Eq. 6}$$

where C loss was the average rate of C loss from either eddy covariance or soil cores, C content was average soil C content in 2009, BD was the average bulk density in 2009, and 9 yrs was the length of the experiment. We divided by C content in order to account for the total mass of soil material that the C fluxes derived from and by the bulk density to estimate the height of soil within the core which had been lost to C fluxes or lateral transport. Because this estimate uses the height of organic soil, not just C, and we have no direct measurements of the loss of elements other than C, both of these estimates could still be high. Average C content and bulk density were averaged from the soil cores at a depth of 5-35 cm, because this layer contains the highest organic matter content and we assume that mineral losses from soil are negligible (Plaza et al., 2019).

3.5. Statistical Analyses

We used mixed effects models to analyze the effects of experimental warming on subsidence and permafrost thaw. All mixed effects models were performed using the lme4 package (Bates et al., 2015) and we included a random effect for repeat measures and for the nested structure of the experiment (plot or soil core nested within fence nested within block). In each model, we examined the model residuals to test for normality and heteroscedasticity.

The impact of experimental air and soil warming on the rate of subsidence was investigated to determine the effect that future warming is likely to have on subsidence. Plot level subsidence was used as the dependent variable and the effects of time, treatment (control, air warming, soil warming, air + soil warming), and the interaction between time and treatment

were considered to evaluate whether rates of subsidence differed in each experimental treatment. Data for all plots were included in the model at each time-step, yielding a total of 48 data points for each year that were evenly distributed across the four treatments. Model fit was evaluated with Akaike Information Criterion (AIC); parameter significance for the best model was shown with 95% confidence intervals determined by bootstrapping with 1000 simulations using the lme4 package (Bates et al., 2015). Differences in slope between groups were determined using the 95% confidence interval in the emmeans package (Lenth, 2018).

The contribution of ice loss to subsidence was estimated using a mixed effects model of subsidence by ice height. Separate models were tested using the total ice height and excess ice height. Subsidence was extracted from the kriged surface at each soil core location and the effect of treatment was considered. This model had a total sample size of 24 soil cores, with half belonging to the control treatment and half to the soil warming treatment. AIC was used to determine the best fitting model and model parameters were evaluated using 95% confidence intervals determined by bootstrapping with 1000 simulations using the lme4 package (Bates et al., 2015).

4. Results

4.1. Subsidence

Subsidence was observed across all blocks and treatments over 9 years of permafrost warming (Figure 3; Movie S1; Movie S2; Movie S3). Subsidence occurred at 1.2 cm yr^{-1} (CI: 1.7, 0.7) in control plots and 1.4 cm yr^{-1} (CI: 2.0, 0.9) in air warming plots, and the rate did not differ significantly between these two groups (Figure 4; Table S1). Subsidence in soil warming plots occurred at 5.4 cm yr^{-1} (CI: 5.9, 4.8), which was over 4 times the rate of the control plots and was significantly different than all other treatments. Air + soil warming plots had the greatest

rate of subsidence at 6.1 cm yr^{-1} (CI: 6.7, 5.6), which was ~5 times the rate of control plots and was also significantly different than all other treatments. The greatest subsidence observed across the footprints of the blocks was 89.2 ± 3.5 cm (mean ± SE of kriging) over 9 years (Figure 3; Figure 4). Starting in 2016, the formation of ponds on the soil warming side of Blocks B and C became evident. Elevation increases of up to 32.6 ± 5.1 cm were also observed within the first several years, however this likely only reflects errors in the GPS time series, as most cells with elevation increases showed <10 cm of increase and the remaining cells occurred near the outer edge of the sampling locations where kriging variance is quite high in some years (Figure 3; Figure S1).

4.2. Permafrost and Carbon Thaw

Thaw penetration was significantly larger than ALT, the traditional method for measuring permafrost thaw (Figure 5). In control plots, ALT was 74.5 ± 1.2 cm and thaw penetration was 88.6 ± 2.3 cm and in soil warming plots, ALT was 92.4 ± 2.7 cm and thaw penetration was 137.4 ± 4.3 cm by 2018 (Figure 5). Using thaw penetration to determine the depth of permafrost thaw over the course of the experiment increased observed thaw by 19 ± 3% in control plots and 49 ± 4% in warming plots. This could mean that rates of permafrost thaw are being underestimated across the circumpolar region, as subsidence is typically not quantified but can be expected wherever permafrost thaw is occurring.

Using thaw penetration to calculate C exposure in the active layer increased the amount of C thaw observed over the course of the study. We found an average of 50.2 ± 1.0 kg C m^{-2} in the active layer in control plots in 2009 (Figure 5). By 2018 there was 67.8 ± 0.9 kg C m^{-2} in the active layer as calculated with ALT and an average of 74.3 ± 1.1 kg C m^{-2} in the active layer as calculated with thaw penetration. Using ALT, 17.5 ± 1.3 kg C m^{-2} thawed over the course of 9

years and 24.0 ± 1.4 kg C m^{-2} thawed using thaw penetration. This meant that in control plots, using thaw penetration to calculate the quantity of newly thawed C resulted in an increase of 37 ± 10% relative to estimates calculated with ALT. In warming plots, we found an average of 41.0 ± 0.8 kg C m^{-2} in the active layer in 2009. By 2018 there was 67.8 ± 1.3 kg C m^{-2} in the active layer as calculated with ALT and 98.1 ± 1.7 kg C m^{-2} as calculated with thaw penetration. Therefore, over the course of 9 years we calculated 26.8 ± 1.5 kg C m^{-2} thawed using ALT and 57.1 ± 1.2 kg C m^{-2} thawed using thaw penetration. This meant that in warming plots, using thaw penetration to calculate the quantity of newly thawed C resulted in an increase of 113 ± 6% relative to estimates calculated with ALT. Although ignoring subsidence does not impact direct measurements of soil C content, using ALT rather than thaw penetration to calculate C exposure in the active layer underestimates the rate of C exposure.

4.3. Drivers of Subsidence

Ice loss was the main environmental driver of subsidence at the site, but soil loss was a significant driver of subsidence, as well. Excess ice height did not correlate with subsidence, but total ice height did (Table S2; Table S3). The magnitude of subsidence was 95% (CI: 52, 138) of total ice height and this relationship did not differ between control and soil warming treatments (Figure 6; Table S3). Given that total ice height is necessarily an overestimate of the contribution of ice to subsidence, as some of the total ice volume must occupy pore space and not contribute to subsidence, the contribution of soil loss to subsidence was used to adjust the estimate of the contribution of ice loss to subsidence. Using eddy covariance data on C loss, we estimated that 9% of the measured subsidence could be due to soil loss, and using soil cores, we estimated 15%. If 9-15% of subsidence was due to soil loss, 85-91% of the measured subsidence remained to be

explained by ice loss, and this corresponded to the loss of ~80-85% of the total ice volume from the thawed permafrost soil layer.

4.4. Hydrologic Response to Subsidence

Subsidence at CiPEHR universally resulted in wetter soils, as subsidence caused the ground surface to drop closer to the water table, and this has consequences for energy transfer and C fluxes. In the most extreme cases in some of the soil warming plots, subsidence resulted in the formation of thermokarst ponds by 2016 and, despite 2017 and 2018 summer seasons having average to below average precipitation (Celis et al., 2018), the ponds rarely dried out in some plots. Even in areas that were not inundated, the water table depth moved closer to the soil surface over 9 years of warming, as the ground surface dropped closer to the water table in all treatments (Figure 7). The average water table depth in control plots in 2009 was 27.6 ± 0.4 cm and in 2018 it was 18.4 ± 0.3 cm, 33% closer to the soil surface. In the soil warming plots, the average water table depth in 2009 was 25.4 ± 0.5 cm and in 2018 it was 6.6 ± 0.3 cm, 74% closer to the soil surface. The increasingly wet conditions are increasing CH_4 fluxes due to anoxic conditions (Taylor et al., 2018) and are likely speeding the rate of thaw through increased energy transfer in water (Jorgenson et al., 2010; Jorgenson et al., 2006; Subin et al., 2013).

5. Discussion

5.1. Subsidence Masks Total Permafrost Thaw

Subsidence was ubiquitous across treatments at CiPEHR and slight increases in temperature were sufficient to dramatically accelerate this process. Both control and experimental warming plots are subsiding at CiPEHR, with gradual subsidence occurring in control plots and more rapid subsidence leading to thermokarst formation in soil warming plots. Gradual subsidence in the control plots left no visible features, despite an average of over 10 cm

of subsidence over 9 years. Rates of subsidence in soil warming plots were over 4x higher than in control plots and ~5x higher in air + soil warming plots, leading to visible thermokarst formation in the most extreme cases. Thermokarst depressions became inundated starting around 2016 and were similar to other thermokarst features that have been identified in the area without experimental warming (Osterkamp et al., 2009). Based on previous research showing that open top chambers mostly affect air temperatures and not soil temperatures (Marion et al., 1997; Hobbie & Chapin, 1998; Shaver et al., 2000), we had not expected air warming to affect subsidence. Despite this, air + soil warming plots subsided more quickly than soil warming plots, although air warming alone had no impact on the rate of subsidence. This could be due to slightly higher deep soil temperatures during the summer season in air + soil warming plots relative to soil warming plots (Mauritz et al., 2017). It is also possible that open top chambers in inundated air + soil warming plots could reduce surface water flow sufficiently to increase water temperature and thereby increase thaw and subsidence at those locations, although we have no measurements of water temperature to confirm this.

ALT measurements at CiPEHR underestimate the thaw of permafrost, and the C it contains, due to the large magnitude of subsidence across all treatments. After 9 years, thaw penetration was 49% greater than ALT in soil warming plots and 19% greater than ALT in control plots. This is similar to the findings of two studies that did not experimentally warm soils, with thaw penetration being ~20% to >50% greater than ALT (O'Neill et al., 2019; Streletskiy et al., 2017). Additionally, we showed that this increased rate of permafrost thaw corresponded to a doubling of the rate of C thaw. This highlights the importance of complementing ALT measurements with subsidence measurements not just for understanding permafrost thaw, but also for understanding the permafrost C feedback to the climate. The

CALM network has made historical ALT measurements in many sites across the circumpolar region. Some of the CALM sites, such as the sites set up in the Mackenzie Valley by the Geological Survey of Canada, use thaw tubes that concurrently track elevation changes (Nixon & Taylor, 1998), but not all sites are accompanied by subsidence measurements. Without concurrent subsidence measurements, it is impossible to determine whether trends in ALT reflect trends in permafrost thaw, especially in the case of gradual, visually undetectable subsidence. Given that thermokarst features are estimated to cover ~20% of the permafrost zone (Olefeldt et al., 2016) and the potential for gradual subsidence to exist without any indication, it is necessary that quantification of subsidence occur at a broader scale and be accounted for when quantifying permafrost thaw. With the expanding availability of LiDAR to determine subsidence rates across entire landscapes, this problem is becoming more tractable, but it is still necessary to track elevation for validation at sites distributed across the circumpolar region.

5.2. Ice Loss and Soil Loss Drive Subsidence

Over 9 years of experimental warming at this site, ice loss was the main contributor to subsidence, accounting for 85-91% of the total subsidence. In permafrost soils, ice exists both within pore spaces and as excess ice that cannot fit within pore spaces, and it is excess ice that is expected to contribute to subsidence (Kokelj & Burn, 2003). However, when we estimated excess ice content using a published value of pore space, excess ice height was far too low to account for subsidence and did not correlate with subsidence (Figure S4; Table S2). This indicates that the published value of pore space we used in our calculations may have been higher than the actual pore space in soils at CiPEHR. Therefore, our estimate of the contribution of ice loss to subsidence was calculated using the total ice volume to get an overestimate, and then adjusted downward using the estimate of the contribution of organic matter loss to

subsidence. Ice loss due to permafrost thaw is recognized as the main contributor to subsidence, including thermokarst formation, where erosion is limited (Jorgenson & Osterkamp, 2005; Kokelj & Jorgenson, 2013; Osterkamp et al., 2009). Since the landscape is relatively flat at this site (~5% slope), we do not observe erosion to be a significant contributor to subsidence as it is in coastal permafrost and retrogressive thaw slumps, for example. The spatial variability of subsidence at this site is likely due to the uneven distribution of ice (observed values of total permafrost ice content prior to thaw in soil cores range from 248-778 g kg^{-1}) and the locations with the highest ice content in the newly thawed active layer tended to experience the most subsidence, as has been observed in previous studies (Jorgenson & Osterkamp, 2005). This heterogeneity both of ice content and subsidence indicates that although subsidence in the control plots was not noticeable without measurements, it cannot be classified as isotropic subsidence, and will likely result in thermokarst pits with continued thaw.

We estimated that 9-15% of the total subsidence was due to soil loss, with the lower bound being estimated from C fluxes to the atmosphere only, and the upper bound being estimated from both C fluxes to the atmosphere and laterally in water. In reality, the soil loss is likely due to both C fluxes to the atmosphere and lateral transport of C in water (Cory et al., 2013; Lee et al., 2010; Plaza et al., 2019; Vogel et al., 2009), but additional direct measurements of lateral rates of C loss at the site are needed to strengthen our confidence in the magnitude of this effect on subsidence. Although this type of partitioning has not previously been published for permafrost ecosystems, we did find one study from a drained ombrotrophic bog in Norway, where 38% of subsidence over a 25 year period following drainage was due to peat loss (Grønlund et al., 2008), indicating that the decomposition of C rich soils can contribute quite significantly to subsidence. Additionally, the contribution of soil loss to subsidence at this site is

supported by several studies in tundra ecosystems that have found lower C content in soils within thermokarst features (Mu et al., 2016; Pizano et al., 2014).

The soil loss we observed can be explained by both the lateral loss of C in the form of dissolved and particulate organic C (Cory et al., 2013; Plaza et al., 2019) and CO_2 and CH_4 fluxes to the atmosphere (Lee et al., 2010; Vogel et al., 2009). Lateral loss of C has been both directly observed at the site, with greater summer season dissolved organic C concentrations in soil warming plots than control plots (Romano, 2018), and also inferred due to greater C loss from soil cores than can be explained by CO_2 and CH_4 fluxes (Plaza et al., 2019). Loss of C to the atmosphere is supported by measurements of CO_2 fluxes both in the area at large (Celis et al., 2017) and at CiPEHR specifically, which show more C loss from warming plots where subsidence is higher (Mauritz et al., 2017). Methane fluxes also correspond to deeper ALT and wetter microsites, and these environmental conditions were observed in soil warming plots which have subsided the most (Taylor et al., 2018).

5.3. Circumpolar Implications

Due to the widespread nature of subsidence in the permafrost zone, ignoring subsidence in measurements of permafrost thaw could be resulting in underestimates of thawed C stocks across the circumpolar region. The size of this underestimate depends mostly upon ice content in permafrost, which is often quite high. For example, on the Beaufort coast of Alaska, ice content varies from 43% in sandy areas to 89% in yedoma (Kanevskiy et al., 2013). Because large portions of the permafrost zone contain high ice volume and loss of ice upon thaw drives the majority of subsidence, it follows that the soil surface height, which serves as a reference for ALT measurements, is shifting across the region. Therefore, it is necessary to quantify subsidence and incorporate it into measures of permafrost thaw, as is done with thaw penetration.

Using thaw penetration as the measure of permafrost thaw across the permafrost region will also improve estimates of the thawed C pool (Nixon & Taylor, 1998). This is especially important because it is estimated that thermokarst features cover ~20% of the permafrost zone and contain ~50% of the C stored in permafrost (Olefeldt et al., 2016) and areas of thermokarst are likely to be the places with the largest discrepancy between ALT and thaw penetration. Of course, while the discrepancy between ALT and thaw penetration is not as great in areas of gradual subsidence, the potential for subsidence to occur without visual indication and the paucity of subsidence measurements means that it could be occurring at broad scales without human knowledge. Additionally, as more C is thawed in permafrost soils and exposed to increasingly wet conditions caused by subsidence, the release of C as both CO_2 and CH_4 could increase, thereby amplifying the warming potential of C fluxes from permafrost ecosystems (Burke et al, 2019; Cassidy et al., 2016; Turetsky et al., 2020; Walter Anthony et al., 2016).

The impact of subsidence on observed permafrost thaw at this relatively southern site serves as a clue of what the future may hold for more northerly sites. Our control plots represent current conditions at the southern extent of permafrost in the discontinuous permafrost zone and, despite the prevalence of abrupt thaw at higher latitudes (Olefeldt et al., 2016; Turetsky et al., 2020), gradual thaw and the resulting subsidence are likely occurring more quickly in the discontinuous permafrost zone than sites at higher latitudes. However, even in more northerly areas with relatively cold permafrost and shallow active layers, subsidence is already having a noticeable impact on observed permafrost thaw. Previously quantified rates of subsidence on the North Slope of Alaska have ranged from a low of 1-4 cm per decade (Liu et al., 2010) to >2.0 cm yr^{-1} over 5 years (Streletskiy et al., 2008), and in the western Canadian Arctic subsidence of 0.4 cm yr^{-1} has been observed over 25 years (O'Neill et al., 2019). These rates are likely to increase

in the near future, resulting in faster C release and irreversible changes to permafrost structure and ecosystem function (Schuur & Mack, 2018; Turetsky et al., 2020). Ecosystem function is likely to shift as hydrologic conditions change following subsidence, making it necessary to incorporate subsidence into estimates of C fluxes in Earth System Models (Ekici et al., 2019). Incorporation of subsidence into Earth System Models must also be accompanied by increased field monitoring to assess model performance and should occur both through the expansion of the network of thaw tubes and remote sensing of subsidence, for example through LiDAR.

6. Conclusions

We observed subsidence rates of 1.2-6.1 cm yr^{-1} at a permafrost warming experiment near the southern extent of permafrost, with the lowest rates occurring in control plots and the highest rates occurring in air + soil warming plots. A 5x increase in subsidence was instigated with warming of only 1-2°C in both air and soil temperatures, as permafrost temperatures are already near 0°C. The subsidence was explained by the combined impact of ice and soil loss, with ice loss driving the majority of subsidence. Additionally, subsidence is causing a shifting reference frame for ALT measurements, the traditional measure of permafrost thaw. Ignoring the impact of subsidence on permafrost thaw underestimates total permafrost thaw over timescales as short as a few years to a decade. We found that using thaw penetration to measure the permafrost thaw in control and permafrost warming plots increased observed permafrost thaw by 19-49% and the observed amount of newly thawed C by 37-113%. Because of the potential for subsidence to impact much of the permafrost zone and the C it contains, it is imperative that studies of permafrost thaw incorporate measurements of subsidence in order to understand the full impact of climate change on permafrost stability and C release from permafrost ecosystems. Future

efforts to quantify subsidence should focus on using LiDAR data, which allow the quick quantification of subsidence over broad scales.

Acknowledgments, Samples, and Data

This work was based in part on support provided by the following programs: U.S. Department of Energy, Office of Biological and Environmental Research, Terrestrial Ecosystem Science (TES) Program, Award #DE-SC0006982 and updated with DE-SC0014085; National Science Foundation CAREER program, Award #0747195; National Parks Inventory and Monitoring Program; National Science Foundation Bonanza Creek LTER program, Award #1026415; National Science Foundation Office of Polar Programs, Award #1203777; NNA: LTREB: The Arctic Carbon and Climate (ACCLIMATE) Observatory: Tundra Ecosystem Carbon Balance and Old Carbon Loss as a Consequence of Permafrost Degradation (Award # 1754839). The National Park Service and Denali National Park, particularly Joel Cusick and Britta Schroeder, contributed their time, technical expertise, and GPS equipment. Jamie Hollingsworth at the Bonanza Creek LTER generously contributed GPS equipment. Many field technicians and graduate students, including Elizabeth Webb and Fay Belshe, made the collection of so many GPS data points possible. Katie Heard and Pat Burns, among many others, contributed to troubleshooting errors in the GPS data. All data are currently available on the Bonanza Creek LTER Data Catalog (http://www.lter.uaf.edu/data/data-catalog). See citations within the methods section for links to specific datasets.

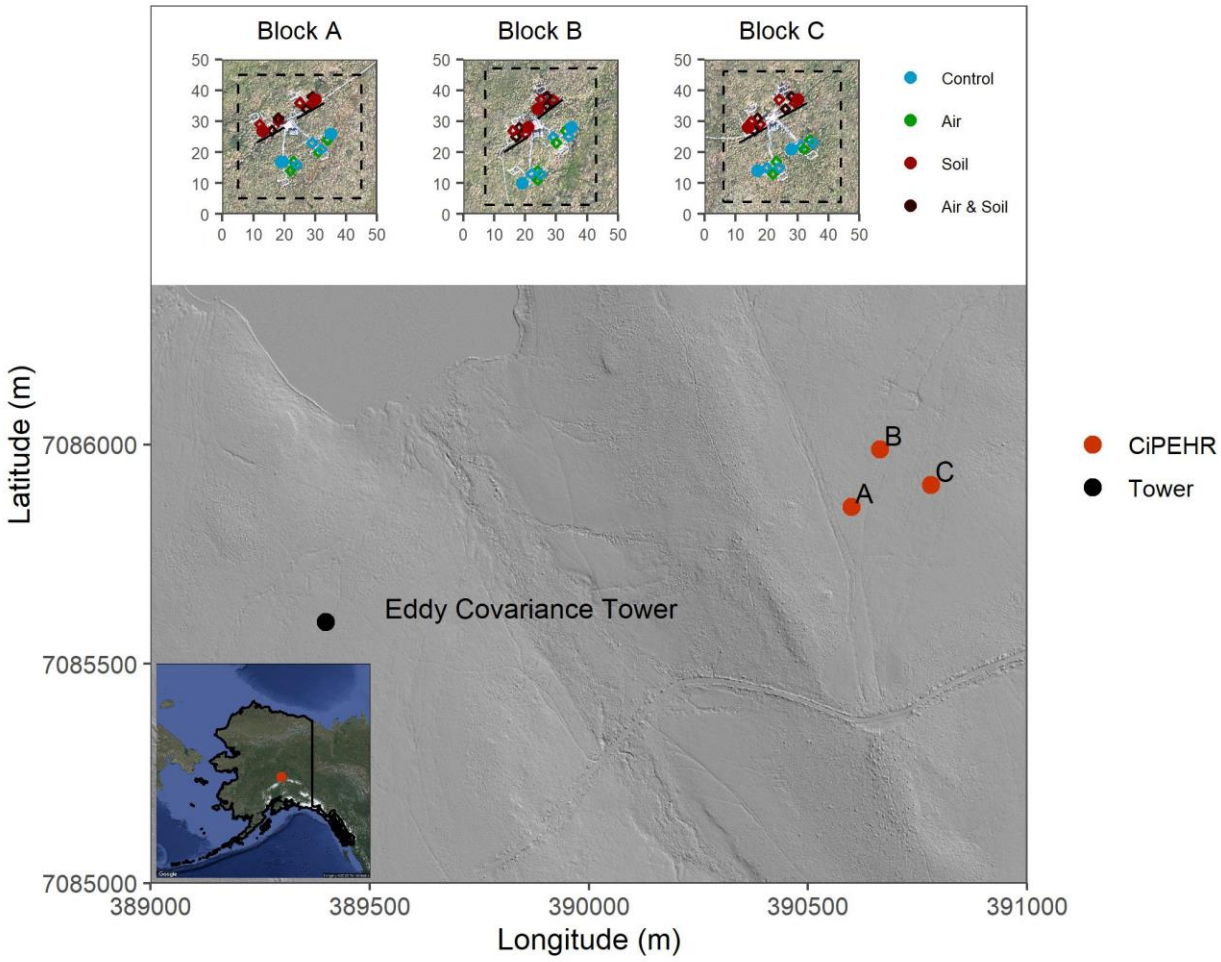

Figure 2.1. The location of the three blocks of CiPEHR and the eddy covariance tower located ~1 km away with the topography shown using a hillshade derived from National Ecological Observatory Network (NEON) airborne Light Detection and Ranging (LiDAR) (NEON, 2017 a). The site is just west of Healy, AK, and Eight Mile Lake is visible at the top left. Axis labels indicate location (m) in UTM Zone 6N. The three insets at the top show the location of soil cores (dots) and plots (open diamonds) within each block over high resolution aerial photographs available from NEON (NEON, 2018). The solid black lines show the location of snow fences and the dashed lines indicates the maximum extent of the GPS transects. The inset at bottom left shows the location within Alaska.

Figure 2.2. Snowpack on the leeward side of the snow fences in April 2016, just prior to snow removal. Photo credit: M. Mauritz.

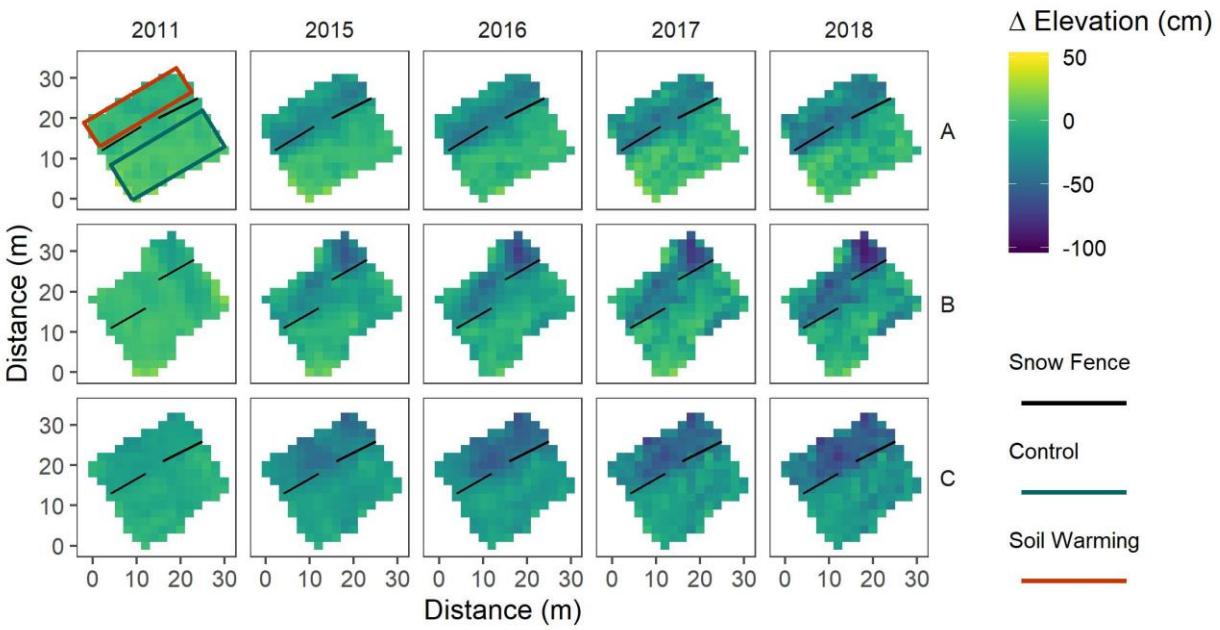

Figure 2.3. The change in elevation relative to 2009 at the three blocks (A, B, C). Years with gap-filled data are not included. Negative values for elevation change indicate areas that have subsided. The locations of snow fences are indicated with solid black lines. The location of control plots and soil warming plots are indicated in the top left facet by blue and red rectangles, respectively, and these relative locations are the same for all blocks.

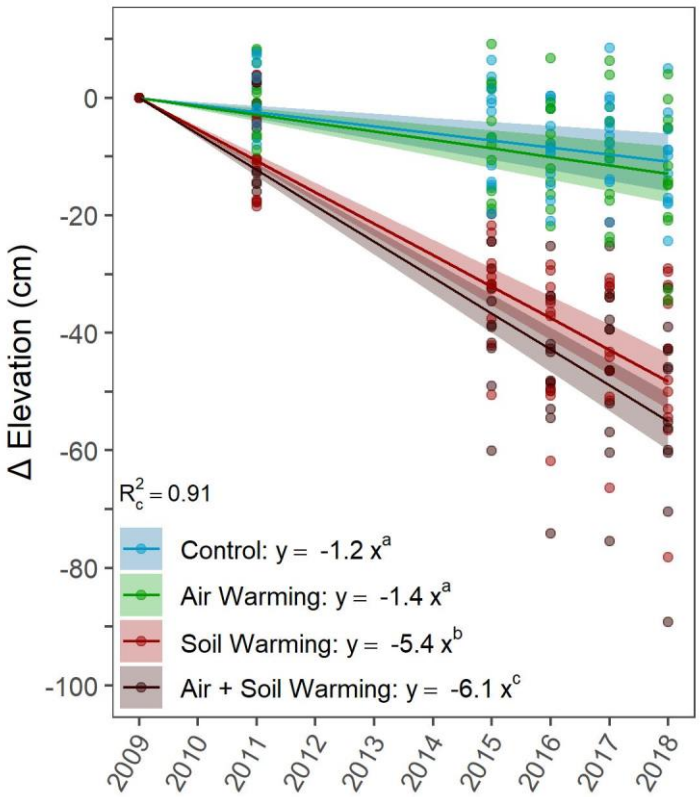

Figure 2.4. A mixed effects model of subsidence (Δ elevation) by time and treatment. All intercepts were forced to zero, as the subsidence is necessarily zero during the first year. Control plots are shown in blue, air warming in green, soil warming in red, and air + soil warming in brown. Each point is a measurement from a single plot. The slope of each treatment is shown in the legend and bands around the regression lines indicate 95% confidence intervals. Superscript letters indicate significant differences in slope. The interaction of time by treatment had a significant impact on subsidence. The slopes of the control and air warming treatments did not differ from each other, but the slopes of the soil warming and the air + soil warming treatments were different from each other and the other treatments.

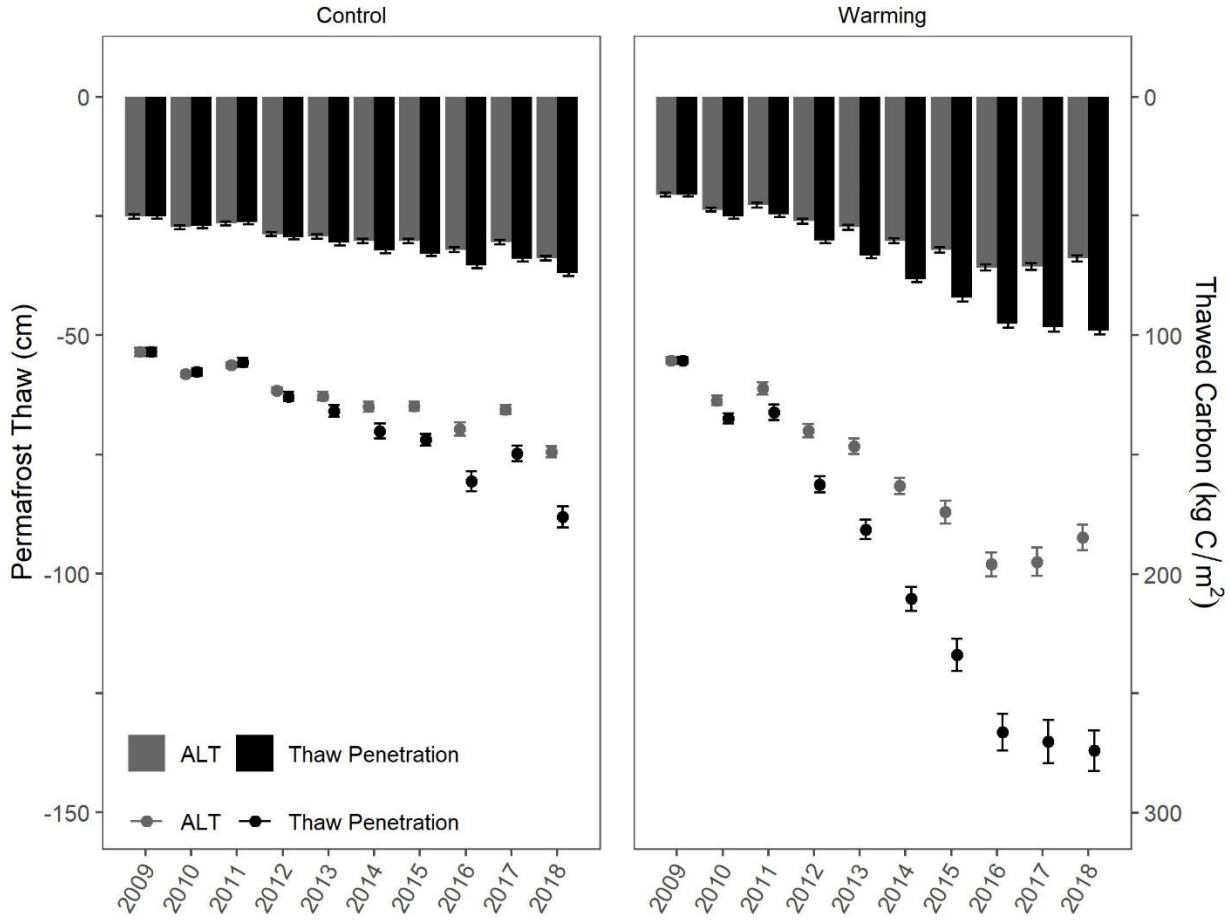

Figure 2.5. The impact of subsidence on observed permafrost thaw and C thaw. The points show permafrost thaw, as measured by ALT and thaw penetration, through time in control and soil warming plots. The bars show the amount of bulk soil C in the active layer, as measured from soil cores, and extrapolated to the field using ALT and thaw penetration. Error bars show SE.

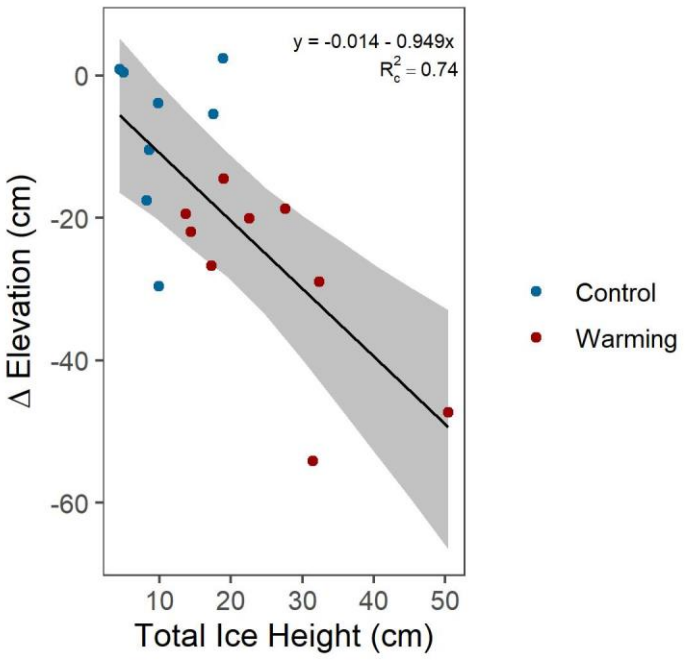

Figure 2.6. A mixed effects model of subsidence by total ice height (sum of 2009 ice volume between the 2009 and 2018 thaw penetration/soil core area). The band around the regression line indicates the 95% confidence interval. Subsidence was 95± 43% the magnitude of total ice height, and experimental treatment did not have an effect on the relationship.

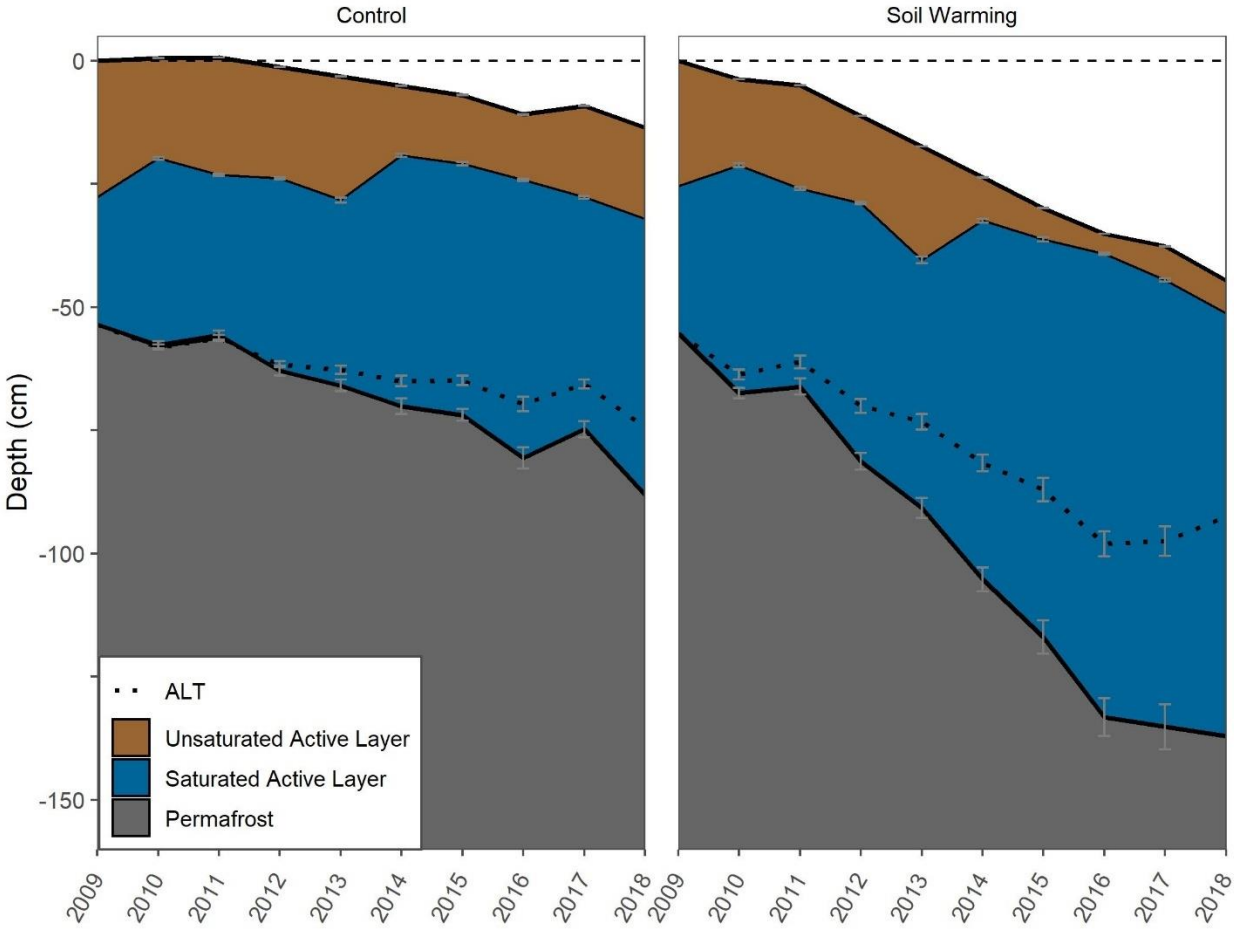

Figure 2.7. The average soil profile in control and soil warming plots. The active layer is between the soil surface and the thaw penetration, both shown as bold lines, and is broken into the layer above the water table and the layer below the water table. The unsaturated active layer (above the water table) is shown in brown, the saturated active layer (below the water table) is shown in blue. Permafrost is shown in gray. The original soil surface is indicated with the dashed line, and the soil surface (upper bold line) has dropped from the original soil surface due to subsidence. The dotted line shows the ALT and the lower bold line shows the thaw penetration. The ALT is shallower than thaw penetration within the soil profile, because using ALT relies on the assumption that the soil surface has not shifted from the original soil surface. The thaw penetration reflects the full depth of permafrost thaw, because it accounts for the change in height of the soil surface. Gray error bars indicate standard error of subsidence, water table depth, ALT, and thaw penetration measurements.

CHAPTER 3: ABRUPT PERMAFROST THAW ACCELERATES CARBON DIOXIDE AND METHANE RELEASE AT A TUSSOCK TUNDRA SITE

Heidi Rodenhizer[a], Fay Belshe[b], Gerardo Celis[c], Justin Ledman[d], Marguerite Mauritz[e], Scott Goetz[a,f], Temuulen Sankey[f], Edward A.G. Schuur[a]

[a]Center for Ecosystem Science and Society, Northern Arizona University, Flagstaff, AZ, USA

[b]Soil and Water Sciences Department, University of Florida, Gainesville, FL, USA

[c]Agronomy Department, University of Florida, Gainesville, FL, USA

[d]University of Alaska Fairbanks, Fairbanks, AK, USA

[e]Biological Sciences, The University of Texas at El Paso, 500 W University Ave, El Paso, TX, USA

[f]School of Informatics, Computing, and Cyber Systems, Northern Arizona University, Flagstaff, AZ, USA

Corresponding Author:

Heidi Rodenhizer, hgr7@nau.edu, ORCID: 0000-0001-5824-3302

600 S Knowles Dr.

Northern Arizona University

Science Laboratory Facilities, Bldg. 17, Rm. 309

Flagstaff AZ, 86011

Fay Belshe, fayray@ufl.edu

Gerardo Celis, celis@ufl.edu, ORCID: 0000-0003-1265-4063

Marguerite Mauritz, memauritz@utep.edu, ORCID: 0000-0001-8733-9119

Temuulen Sankey, temuulen.sankey@nau.edu, ORCID: 0000-0002-6919-8428

Scott Goetz, scott.goetz@nau.edu, ORCID: 0000-0002-6326-4308

Edward A.G. Schuur, ted.schuur@nau.edu

Highlights

- The thermokarst detection algorithm uses one elevation map to identify abrupt thaw
- Water tracks were the most extensive form of abrupt thaw
- Abrupt permafrost thaw promotes carbon dioxide and methane release

Abstract

Abrupt thaw could cause permafrost ecosystems to release more carbon than is predicted from gradual thaw alone. However, our ability to map thermokarst features is limited in scope and the observed responses of carbon fluxes to abrupt thaw are variable. We developed a thermokarst detection algorithm which identifies thermokarst features from a single elevation dataset with 71.5% accuracy, and applied it in Healy, Alaska, USA. Additionally, we investigated the landscape level variation in carbon dioxide and methane fluxes due to abrupt thaw using eddy covariance. 7% of the site was classified as thermokarst, with water tracks being the most extensive form of thermokarst, although small pits were much more numerous. Abrupt thaw promoted higher carbon uptake during the growing season, when increases in gross primary productivity outpaced increases in ecosystem respiration in vegetation-dense water tracks. However, this was outweighed by higher carbon release in thermokarst features during the non-growing season. Additionally, abrupt thaw promoted methane production nearly year-round. Our findings support the hypothesis that abrupt thaw of permafrost carbon will contribute to the

permafrost climate feedback above and beyond that associated with gradual thaw and highlights the need to map thermokarst and incorporate abrupt thaw into Earth System Models.

Keywords: Arctic, Permafrost, Thermokarst, Carbon Dioxide, Methane

1. Introduction

1.1. Permafrost Carbon

Permafrost thaw has been widely documented across the permafrost zone as the climate has warmed (Hinkel and Nelson 2003; Luo et al. 2016; Nixon and Taylor 1998; Osterkamp and Romanovsky 1999; Streletskiy et al. 2008; Veremeeva et al. 2021). This is an issue of growing global importance as it impacts communities located on unstable permafrost ground, and global climate through the release of greenhouse gases (Natali et al. 2019; E. A. G. Schuur and Mack 2018). Permafrost is estimated to contain 1460-1600 Pg of organic carbon (Edward. A. G. Schuur et al. 2018), which is approximately twice as much carbon as is in the atmosphere (Houghton 2007). While permafrost ecosystems have historically been a carbon sink, permafrost thaw is making organic carbon available to microbial use, and release to the atmosphere (Edward. A. G. Schuur et al. 2018).

1.2. Gradual vs. Abrupt Permafrost Thaw

Permafrost thaws both gradually and abruptly. Gradual thaw has been observed across much of the permafrost zone, as the seasonally thawed active layer deepens incrementally (Luo et al. 2016). This type of thaw leads to relatively uniform and steady changes across the landscape. However, in areas of high ice content, permafrost often thaws abruptly, as the loss of excess ice causes ground subsidence and thermokarst (the formation of depressions) (M. Torre Jorgenson, Shur, and Pullman 2006; Nelson, Anisimov, and Shiklomanov 2001). Thermokarst accelerates the rate of permafrost thaw through shifts in hydrology, most commonly ponding or

increases in flow, increasing the rates of heat flow and/or erosion in a positive feedback cycle (M Torre Jorgenson et al. 2010; M T Jorgenson and Osterkamp 2005; S. V. Kokelj and Jorgenson 2013). Although abrupt thaw is not a new phenomenon, the formation of thermokarst features has accelerated as the climate has warmed and extreme weather events have become more common. Abrupt thaw occurs sporadically across the landscape because abrupt thaw is limited to areas where permafrost ice content is high (M T Jorgenson and Osterkamp 2005). Abrupt thaw also tends to occur sporadically through time, as initiation of thermokarst development occurs most often following triggers such as climate extremes or disturbance, but development can occur rapidly following initiation due to positive feedbacks. Weather extremes that trigger abrupt thaw activity include unusually warm (Farquharson et al. 2019; M. Torre Jorgenson et al. 2020; Kanevskiy et al. 2017; Lantz and Kokelj 2008; Lara et al. 2016; Swanson 2021; Veremeeva et al. 2021; Ward Jones, Pollard, and Jones 2019), wet (Kanevskiy et al. 2017; Swanson 2021; Veremeeva et al. 2021), and/or snowy years (M. Torre Jorgenson et al. 2020). Additionally, disturbance to vegetation cover and the ground surface are known to initiate abrupt thaw (Kanevskiy et al. 2017).

Once initiated, abrupt thaw can result in thermokarst features with widely variable morphological characteristics through internal feedbacks that depend on site-specific factors including topography, soil characteristics, soil ice content, erosion, and thermoerosion (M T Jorgenson and Osterkamp 2005; S. V. Kokelj and Jorgenson 2013), resulting in different rates of permafrost carbon thaw, soil temperatures, and hydrologic conditions. On hillslopes, water drainage plays an important role in thermokarst, leading to elongated features in which ponding is not common or extensive (S. V. Kokelj and Jorgenson 2013). In many cases, permafrost soils are directly exposed to the atmosphere due to rapid erosion, accelerating thaw and disallowing

plant establishment (M T Jorgenson and Osterkamp 2005). On flat terrain, inundation is common in thermokarst features, resulting in a less elongated shape (S. V. Kokelj and Jorgenson 2013). These features tend to expose permafrost soils to the atmosphere less often, as erosion is limited, and allowing plant establishment (M T Jorgenson and Osterkamp 2005). Regardless of morphology, all thermokarst features expose older carbon stored frozen in permafrost soils to the dynamics of the modern carbon cycle.

1.3. Permafrost Thaw and Carbon Cycling

Abrupt thaw occurs preferentially in areas of high carbon content, perhaps because wet soils have the potential for both higher ice and carbon content, and increases the likelihood that permafrost carbon is released to the atmosphere. It is estimated that ~20% of the permafrost zone is impacted by abrupt thaw processes, but these areas contain up to half of the carbon stored in permafrost soils, with wetland thermokarst landscapes accounting for a disproportionately high amount of carbon (Olefeldt et al. 2016). When these soils thaw abruptly, carbon release to the atmosphere tends to increase (Cassidy, Christen, and Henry 2016; Eugénie S. Euskirchen et al. 2017; Turetsky et al. 2020), although thermokarst morphology and associated environmental conditions regulate the eventual fate of thawed carbon at individual sites (Olefeldt et al. 2016; Rodenhizer et al. 2020; Turetsky et al. 2020). Field studies have found a range in the response of carbon fluxes to abrupt thaw across sites, likely due to the range of environmental conditions present. In terms of overall ecosystem carbon balance, both increases (higher carbon release) (Cassidy, Christen, and Henry 2016; Eugénie S. Euskirchen et al. 2017) and decreases (higher carbon uptake) in net ecosystem exchange (NEE; the net exchange with the atmosphere) have been observed within thermokarst features (Lee et al. 2011; Vogel et al. 2009). Conflicting responses of NEE are unsurprising, as NEE is the difference between Gross Primary Production

(GPP; photosynthetic uptake of) and ecosystem respiration (R_{eco}; release of through respiration by autotrophs and heterotrophs), both of which can respond to abrupt thaw in divergent ways. GPP has been found to increase in response to abrupt thaw in some studies (Eugénie S. Euskirchen et al. 2017; Lee et al. 2011; Vogel et al. 2009), while it has decreased in others (Cassidy, Christen, and Henry 2016). Increases in GPP can be caused by increased access to nutrients released from the thaw front (Hewitt et al. 2019; 2018; Salmon et al. 2016), or by drought alleviation caused by uneven ground subsidence (Eugénie S. Euskirchen et al. 2017; Lee et al. 2011). Decreases in GPP can be caused by erosion disturbing plant growth (M T Jorgenson and Osterkamp 2005) or by either drought or flooding caused by uneven ground subsidence (Eugénie S. Euskirchen et al. 2017; Mauritz et al. 2017). Similarly, R_{eco} has shown both positive (Abbott and Jones 2015; Eugénie S. Euskirchen et al. 2017; Lee et al. 2011; Vogel et al. 2009) and negative responses to abrupt thaw (Abbott and Jones 2015; Cassidy, Christen, and Henry 2016; Jensen et al. 2014). High rates of erosion in certain thermokarst morphologies can cause export of carbon off-site and limit R_{eco} (Abbott and Jones 2015), while deeper thaw and higher soil temperatures within thermokarst features can allow higher respiration throughout the fall, winter and spring (Vogel et al. 2009; Webb et al. 2016).

Where and when permafrost soils thaw gradually and abruptly is important for understanding the fate of thawing permafrost carbon. When permafrost thaws gradually, carbon and nutrients released incrementally from the permafrost thaw front can stimulate plant growth and carbon uptake at the same time as heterotrophic respiration (E. A. G. Schuur and Mack 2018). Because gradual thaw is nearly ubiquitous across the permafrost zone and changes occur incrementally, it is simpler to include in Earth System Models than abrupt thaw (Natali et al. 2021; E. A. G. Schuur et al. 2008). Abrupt thaw complicates the balance between carbon uptake

and carbon release within permafrost ecosystems, by promoting the rapid thaw of carbon rich soils differentially across the landscape and through time and by causing divergent flux responses depending on thermokarst morphology and associated environmental conditions (Cassidy, Christen, and Henry 2016; Eugénie S. Euskirchen et al. 2017; Lee et al. 2011; Vogel et al. 2009). Because abrupt thaw is more complex than gradual thaw and the spatial distribution is poorly understood, it is difficult to incorporate into Earth System models (Natali et al. 2021; Olefeldt et al. 2016). Therefore, it is necessary to gain a better understanding of where abrupt thaw occurs, which morphological characteristics occur where, how extensive abrupt thaw is, and the impact abrupt thaw has on carbon release from thawing permafrost.

1.4. Spatial Distribution and Remote Sensing of Thermokarst Features

Relatively little is known about the spatial distribution and extent of thermokarst features across the circumpolar region because not all forms of thermokarst are equally visible and due to the difficulty of data collection and processing of high-resolution data over large areas. Across smaller areas (~1,000,000 km^2 or less), high-resolution remote sensing can detect discrete thermokarst features through the observation of subsidence (change detection) or the direct observation of spectral signatures associated with differences in the plant, soil, or water cover from the surrounding landscape (Abe et al. 2020; Belshe, Schuur, and Grosse 2013; Grosse, Morgenstern, and Lantuit 2008; Grosse, Schirrmeister, and Malthus 2006; Jones et al. 2015; 2013; Steven V. Kokelj et al. 2020; Polishchuk et al. 2017). Using subsidence to detect thermokarst requires two digital terrain models (DTMs, a raster image of ground surface elevation) from different points in time at a long enough interval that the magnitude of subsidence is greater than the accuracy of the elevation data. These DTMs can be produced using a variety of remote sensing methods (i.e. Light Detection and Ranging (LiDAR), Interferometric

Synthetic Aperture Radar (InSAR)). Identifying spectral patterns associated with thermokarst features requires only a single spectral image (i.e. airborne multispectral and hyperspectral), but are still limited in the spatial extent over which they can be applied. This is because the spectral patterns used in classification vary over time and space and training separate classifications for each image quickly becomes unwieldy. Therefore, while both repeat imagery and spectral classification methods are highly effective, they are limited in spatial extent. The only study spanning the entire circumpolar region to date relied on expert evaluation to create a map of thermokarst likelihood (Olefeldt et al. 2016), as fully quantitative methods do not exist at that scale.

1.5. Application of A New Thermokarst Detection Method

In this study, we developed a method for detecting thermokarst with fewer spatial limitations by identifying thermokarst depressions from a single elevation image. This method removes the reliance on site-specific relationships and decreases the required number of elevation images. We applied this algorithm at an 81 km^2 site located on permafrost undergoing abrupt thaw within the discontinuous permafrost zone. In addition, we investigated the impact that abrupt thaw is having on this ecosystem through multiple lines of inquiry. First, we analyzed the morphology of all thermokarst features to determine which types of thermokarst features are responsible for the most permafrost carbon thaw. Second, we estimated the change in microtopography and thermokarst percent cover since 2008. Third, we used an eddy covariance (EC) tower to estimate the impact of abrupt thaw on carbon fluxes, as we know that permafrost thaw is causing carbon release, but we have not yet investigated the effect of abrupt thaw specifically, as opposed to gradual thaw.

2. Site

The Eight Mile Lake study site is located North of Denali National Park, USA, at 450-1180 m in the foothills of the Alaska Range (WGS84, 63°52'59"N, 149°13'32"W). Slopes are between 0° and 74°, with a median of 5°. Hillslopes between 3° and 10° cover half of the study area. The mean annual temperature is -0.94°C, with a growing season (May-Sept.) average temperature of 11.91°C and a non-growing season (Oct.-Apr.) average temperature of -10.09°C (Mauritz et al. 2017). Due to the high elevation, much of the study site is moist acidic tussock tundra, although it is located within the boreal forest biome. The site contains some forested areas, particularly near Panguingue creek in the East. The site is located within the discontinuous permafrost zone, but is underlain by continuous permafrost. Soils sampled within tundra at the site are Gelisols and are composed of an organic layer approximately 0.45-0.65 m thick above cryoturbated mineral soils that are composed of glacial till and windblown loess (Natali et al. 2011). The site contains an experimental soil and air warming experiment, the Carbon in Permafrost Experimental Heating Research (CiPEHR), established in 2008 (Natali et al. 2011), and a natural permafrost thaw gradient, which has been monitored since 2004 (E. A. G. Schuur et al. 2007). An EC tower near the natural thaw gradient has measured CO_2 fluxes since 2008 and CH_4 since 2015 (T. Schuur et al. 2021). In 2017, the National Ecological Observatory Network (NEON) began monitoring a site a few kilometers away, providing publicly available data.

3. Methods

3.1. Remote Sensing Data

We utilized airborne LiDAR-derived DTMs from NEON for thermokarst detection and subsidence modeling (NEON 2020a). LiDAR data were collected in July of 2017, 2018, and 2019 in a roughly 10x10 km area centered on their observation site just East of Healy, AK and

containing both CiPEHR and the permafrost thaw gradient. The LiDAR data were collected using an Optech ALTM Gemini discrete LiDAR scanner from a Twin Otter aircraft flying at approximately 1000 m above ground level, resulting in approximately 1-4 returns per square meter. NEON processed the raw LiDAR data into the DTMs we utilized at 1 m resolution by removing vegetation returns and interpolating a continuous surface.

We used two images for validation of the thermokarst feature detection. First, we used high resolution camera data available from NEON (NEON 2020b). The Optech Gemini high resolution digital camera images were collected from the same platform as the LiDAR acquisitions in 2017, 2018, and 2019, and provided color images at 10 cm resolution. Despite the exceptional resolution, visibility of thermokarst features was limited where vegetation was thick, because the images were acquired near peak greenness. When NEON imagery was insufficient to determine the presence or absence of thermokarst, we used an October, 2018 Worldview 2 image, which allowed better visibility through vegetation despite lower resolution and was provided through the Nextview license and accessed through NASA's High-End Computing Program as a part of the Arctic Boreal Vulnerability Experiment. The Worldview 2 sensor has a high-resolution panchromatic band at 0.46 m resolution and 8 spectral bands at 1.84 m resolution, including a red, green, and blue band, which we used to create a pan-sharpened image at 0.46 m resolution.

3.2. Thermokarst Detection Algorithm

We developed the thermokarst detection algorithm, which detects thermokarst features by identifying local elevation minima from a single DTM (Figure 1). Because the thermokarst detection algorithm does not rely on site-specific relationships and requires only one elevation image, it has the potential to be applicable at sites across the permafrost zone. An R-package of

the algorithm is publicly available on github (github.com/HRodenhizer/thermokarstdetection). The algorithm has three steps which were developed using the raster package in R (Hijmans 2021): 1) median elevation is calculated in one or more circular neighborhood(s) of user-defined size around each cell of a DTM, 2) microtopography is calculated by subtracting the neighborhood median elevation from the elevation within each cell, and 3) elevation minima are classified as cells in which microtopography falls below a user-defined threshold.

Using the high performance computing cluster at NAU, we applied the thermokarst detection algorithm separately on each of three annual DTMs (2017-2019). We calculated median elevation multiple times using different neighborhood sizes (15, 25, and 35 m radii), in order to test the ability of different window sizes to discern thermokarst features of varying size (Table S1). Both the elevation and median elevation rasters were cropped to a 9x9 km tile in order to ensure that no edge cells were missing values before continuing. Microtopography was calculated for each of the median elevation rasters. Local elevation minima were determined by reclassifying microtopography using two different thresholds (0 and -5 cm) such that values below the threshold (reflecting local elevation minima or potential thermokarst) received a value of 1 and values above the threshold (reflecting local elevation maxima or non-thermokarst) received a value of 0.

Site-specific post-processing (not included in the R-package) was used to filter out elevation minima which were unlikely to be caused by thermokarst processes. The landscape filter masked elevation minima that coincided with non-thermokarst lakes, steep slopes, and deeply-incised river valleys. Steep slopes in this area are unlikely to contain thermokarst due to the fact that they tend to be extremely rocky and have low soil ice content. Although thermoerosion likely plays a role in forming river valleys, mechanical erosion is likely the main

driver of elevation changes in riverbeds, so these features were removed to ensure a conservative classification. Any elevation minima which fell within one of the filters were removed to create the thermokarst classifications. The hydrology toolset in ArcMap (ESRI, Redlands, CA) was used to model flow accumulation for the river filter, but all other filter steps were completed in R using the raster, sp, and sf packages (Edzer Pebesma 2018; E. Pebesma and Bivand 2005).

To create the slope filter, we calculated slope from the 2018 DTM using the terrain function and, using trial and error to determine a reasonable cut-off value, reclassified the raster to assign values > 25° to 1 and values < 25° to 0. Some small areas with slopes > 25° were removed from the slope filter by using the erode function followed by the dilate function in the raster package, so that the filter would only remove larger and more consistently steep areas. The resulting raster was then buffered to 25 m in order to ensure that areas near steep slopes with potentially high rates of erosion (such as relatively flat riverbeds at the bottom of gullies) were also removed.

To create the river filter, we first filled in sinks in the 2017 DTM using the fill tool in ArcMap 10.6.1, as this is required for hydrologic analysis to avoid cells with undefined drainage direction. We used the flow direction tool to determine the direction of flow from the filled DTM and the flow accumulation tool to calculate flow accumulation values from the flow direction raster. The flow accumulation raster was then reclassified in R using several different cut-off values to identify rivers of varying sizes, with flow accumulation values greater than the cutoff being assigned to 1 (river) and values less than the cutoff being assigned to 0 (not river). We determined flow-accumulation cutoff values of 7,000,000, 8,000,000, and 20,000,000 based on the level of incision as determined by visual inspection of the high-resolution camera data. Each of the three river rasters was buffered, as this analysis only allows rivers to be one cell wide in

any location, but the actual riverbeds are typically wider. Since the riverbed width tends to increase with increased flow, we used a visual inspection of the imagery to decide on a 50 m buffer for the smallest rivers, a 100 m buffer for medium-sized rivers, and a 250 m buffer for the largest rivers. These three buffered river layers were combined into one raster such that a cell that had a value of 1 in any layer remained 1 and a cell that was 0 in all layers remained a 0.

To create the non-thermokarst lake filter, we intersected lake and stream maps of the study site. We assumed all sinks were lakes, and sinks were determined by subtracting the 2018 filled DTM from the 2018 DTM and converting this raster to polygons using the sf package. The river raster with the lowest cut-off value was converted to a vector river layer, and the lake polygons and rivers were intersected to retain only those lakes which intersected a river, i.e. a lake with an inlet and/or outlet. These polygons were converted back to raster format, with 1 representing non-thermokarst lakes and 0 representing everything else. The resulting raster had a few holes in the only non-thermokarst lake at the site, Eight Mile Lake, so we dilated the raster twice and then eroded the raster twice to fill in any holes.

Finally, the three filter rasters (steep slopes, river buffer, and non-thermokarst lakes) were combined such that any cell with a value of 1 in at least one layer remained 1 and any cell with a value of 0 in all layers remained 0. This combined landscape filter was overlaid with the filled elevation minima rasters in order to remove the thermokarst classification from any cells unlikely to be thermokarst due to landscape features. The filter raster was subtracted from the elevation minima rasters on a cell by cell basis and reclassified such that values of 1 reflected thermokarst features which remained after filtering and values of 0 reflected cells that were non-thermokarst, regardless of whether they had never been classified as thermokarst or were filtered out.

Visual inspection of the thermokarst classification at this point indicated that many of the thermokarst features contained small groups of cells that were classified as non-thermokarst within an otherwise contiguous thermokarst feature. We filled in these holes as well as possible by using the dilate and erode functions within the mmand package (Clayden 2020). We ran dilate twice and then ran erode twice using the rook's case for adjacency. The dilate function works by centering a kernel on each non-zero value in order to extend the non-zero values to all cells specified in the kernel, while the erode function does the opposite by centering on zero values to erase all cells within the kernel. In addition to filling in non-thermokarst holes within larger thermokarst features, this process results in reducing the number of thermokarst polygons associated with a single, fragmented thermokarst feature (for example a single water track that the thermokarst classification identified as many smaller, adjacent thermokarst features).

The thermokarst classifications derived using different neighborhood sizes were combined into multiple classifications using different combinations of neighborhood sizes (see Table S1 for all combinations), because we expected that a smaller neighborhood size would result in a greater number of small thermokarst features and more holes in the middle of large thermokarst features, while a larger neighborhood size would result in fewer small features and fewer holes in large features. These combinations were validated alongside each of the models which used one neighborhood size (Table S1).

In order to select the best method of thermokarst detection, we determined the presence of thermokarst using the high-resolution aerial and satellite imagery in 200 sample cells. We used ~100 samples in each of the thermokarst and non-thermokarst classes. The sample order was scrambled and any information that would identify the sample cell's classification was removed prior to visual inspection of each point. We first studied the NEON camera image, due to its

higher resolution, but if identification proved difficult due to thick vegetation, we also studied the Worldview 2 image. We considered any visible small ponds, gullies, and depressions to be thermokarst in our validation process. In addition, any cells that fell within more heavily vegetated water tracks (tracks that route water downslope but may or may not have surface water) were considered thermokarst, even though it was nearly always impossible to see through the vegetation in either validation image in these regions. Given the presence of increased vegetation, which likely indicates a deeper active layer and, therefore, subsidence, we decided to include all these cells in the thermokarst category. We calculated the overall, producer's (how likely a real feature on the ground is to be classified correctly on the map), and user's (how likely a class shown on the map will be present on the ground) accuracies for each of the thermokarst rasters (Congalton and Green 2019), including the combined rasters. The raster classification with the highest overall accuracy was converted to vector format (polygons) and holes smaller than 25 m^2 within polygons were filled in to reduce polygon complexity for subsequent analysis using the packages sp and sf (Edzer Pebesma 2018; E. Pebesma and Bivand 2005). The thermokarst classification map (raster format) with the highest overall accuracy and producer's accuracy was converted to vector format (polygons) and, within a single polygon, holes smaller than 25 m^2 were filled in using the packages sp and sf to reduce polygon complexity for subsequent analysis.

3.3. Analyses

All analyses were performed in R (R Core Team 2021). Spatial data were handled using the raster and sf packages, while non-spatial data were handled using the tidyverse (Wickham et al. 2019) and data.table (Dowle and Srinivasan 2021). Visualizations were created with ggplot2

(part of the Tidyverse), viridis (Garnier et al. 2021), ggnewscale (Campitelli 2021), and ggpubr (Kassambara 2020).

3.3.1. Thermokarst Morphology Analysis

Using the vector thermokarst classification map created in section 3.2, morphological characteristics of thermokarst features were calculated on a polygon by polygon basis. The size of each feature was calculated as the number of 1 m^2 cells within each polygon. To determine thermokarst shape for each feature, we used the Polsby-Popper test, which is a metric of the "compactness" of a shape. This metric falls between 0 and 1, with values near 0 indicating shapes that are not very compact (long or convoluted thermokarst features such as water tracks) and values near 1 indicating a high degree of compactness (round thermokarst features such as thermokarst pits and lakes). Thermokarst depth was approximated using microtopography, because microtopography is the difference between the actual elevation of a cell and the median elevation in the neighborhood surrounding it at one point in time. This should be more accurate than the subsidence observed over the study period, because many thermokarst features at this site are decades old, while our LiDAR data only span two full years. However, microtopography is an underestimate of depth because the 1 m^2 resolution results in average elevations which exclude the most extreme values (Wu and Li 2009) and inundation and/or thick moss growth often obscures the ground surface. In each cell, we extracted the minimum microtopography from the three layers created with different neighborhood sizes in section 3.2 and calculated the mean for each polygon. Feature volume was calculated as the product of feature size and mean depth. Finally, we binned thermokarst features separately by size and shape classes. Within each class, we determined the prevalence as the number of features of that class divided by the total

number of features, thermokarst percent cover as the sum of thermokarst feature sizes divided by the area of the study site, the mean depth, and the mean volume.

3.3.2. Thermokarst Subsidence Analysis

We compared subsidence (2017-2019) between non-thermokarst areas, the edges of thermokarst features, and the centers of thermokarst features. Subsidence was calculated as the difference between the 2017 and 2019 LiDAR-derived DTMs. We identified the edges of thermokarst features as the 1 m wide ring of cells that fell immediately outside the thermokarst feature outline. Subsidence was then extracted from a stratified random sample of ~500 cells in each thermokarst class (total: 1500) and the average subsidence and standard error were calculated for each class. Differences in the magnitude of subsidence between groups were tested using a pairwise contrast in emmeans (Lenth 2021). To validate the LiDAR-derived subsidence, we calculated subsidence over the same time period using high-precision GPS measurements taken at CiPEHR (Rodenhizer, Mauritz, et al. 2021).

3.3.3. Eight Mile Lake Watershed Decadal Change Analysis

We investigated thermokarst development since 2008, as these changes could impact hydrology and carbon fluxes. To estimate change in the extent of thermokarst features, we compared our results to a previous study, which quantified thermokarst features within the Eight Mile Lake Watershed using a high resolution spectral classification from 2008 (Belshe, Schuur, and Grosse 2013). We calculated the percent cover of thermokarst (mean of 2017-2019) within the Eight Mile Lake Watershed using the methods described in the Thermokarst Morphology Analysis section (3.3.1). To calculated the change in microtopography since 2008, we used an approximate footprint of the EC tower (225 m radius circle) which ensured the inclusion of all areas previously investigated in Belshe et al. (Belshe et al. 2012). For this analysis, we re-

calculated microtopography following Belshe et al. (Belshe et al. 2012), which differs from section 3.2 in that mean elevation was calculated by aggregating elevation to 30 m resolution and then resampling to 1.5 m resolution, instead of using a moving circular window to calculate median elevation. The change was calculated as the difference between the 2008 microtopography raster and the 2017-2019 average microtopography raster. To investigate the relationship between surface roughness and extent of abrupt thaw, the approximate EC tower footprint was split into 360 1° slices. Within each slice, we calculated the thermokarst percent cover following the methods described in section 3.3.1 and surface roughness as the standard deviation of microtopography.

3.3.4. Carbon Flux Analysis

We used EC tower data to investigate the role that abrupt thaw plays in regulating CO_2 and CH_4 fluxes at the site. Raw (10Hz) flux tower measurements taken between May 1, 2017 and April 30, 2020 were processed to 30 minute NEE in EddyPro 7 (Rodenhizer, Celis, et al. 2021). During the growing season day (GS Day), R_{eco} was estimated using a Night Respiration model from the same time period, and GPP was taken as the difference between NEE and R_{eco}. At night and during the non growing season (NGS/Night; defined as PAR < 10), GPP was assumed to be 0 and R_{eco} was set equal to NEE (Reichstein et al 2005). For more details about the post-processing and QA/QC of the CO_2 flux data see Schuur et al. (2021). 30 minute CH_4 fluxes between May 1, 2016 and December 31, 2019 were filtered using the REddyProc package (Wutzler et al. 2018) and gap filled using artificial neural networks as a part of FLUXNET-CH_4 (Delwiche et al. 2021).

To estimate carbon fluxes by thermokarst percent cover, we used the two-dimensional parameterization for Flux Footprint Prediction in R (Kljun et al. 2015) to model the flux footprint

for each flux and calculate the contribution of thermokarst affected land to the flux. The boundary layer height was calculated following Appendix B of Kljun et al. (2015) for neutral and stable conditions and set to 1500 m for convective conditions. At each half hour time step, the flux footprint raster was multiplied by the average 2017-2019 thermokarst classification and all cells were summed to calculate the thermokarst percent cover for that flux.

We used linear regression to investigate the impact of abrupt thaw on carbon fluxes. CO_2 fluxes were separated into GS Day and NGS/Night groups in order to separate conditions with and without photosynthesis. For each group (GS Day, NGS/Night) and carbon dioxide flux (NEE, GPP, and R_{eco}), excepting NGS/Night GPP, which is theoretically impossible, we tested a maximum model of carbon flux ~ thermokarst percent cover*month, because we expected variation in the impact of thermokarst on fluxes throughout the year depending on divergent soil thermal conditions within and outside of thermokarst features. For CH_4 fluxes, we removed pulses of CH_4 release or uptake which were more than 3 standard deviations from the mean in a 2-week rolling window. We tested a maximum model of CH_4 flux ~ thermokarst*month. Due to the small number of methane pulses and extreme non-normality of the data, we did not run statistical models for methane pulses. For each regression model, we tested residuals for the assumption of normality and spatial autocorrelation. Because model residuals were not normally distributed, we bootstrapped confidence intervals for model coefficients rather than using p-values for hypothesis testing. We did not find strong evidence of spatial autocorrelation in the model residuals. We used backward stepwise selection based on AIC to remove unnecessary variables and select the best model.

4. Results

4.1.Validation of Thermokarst Classification

We found that thermokarst classification performance differed depending on both the neighborhood size used to calculate median elevation and the threshold used to classify elevation minima, with models that combined multiple neighborhood sizes generally performing better than models which used only a single neighborhood size. The thermokarst classifications ranged in overall accuracy from 61.5% (large neighborhood) to 71.5% (both small combination and complete combination) (Table 1, Table S1). Because there was a tie between two combinations for the best classification, we chose the complete combination (which included all three neighborhood sizes) based on the following lines of reasoning: 1) the small combination, which lacked thermokarst detected at the largest neighborhood size, tended to leave gaps in large, contiguous thermokarst features, and the complete combination was better able to fill these in, and 2) both of the best performing classifications were more likely to miss the presence of thermokarst features than to identify non-thermokarst as thermokarst, indicating that the less conservative combination was a better choice in order to balance missing fewer thermokarst features and the possible inclusion of false positives.

4.2. Site-Wide Thermokarst Statistics and Morphological Characteristics

Overall, we found that thermokarst features covered 7% of the landscape, or 5.7 km^2, with considerable variability depending on slope and glacial history (Figure 2). The dendritic pattern of water tracks were found across large swaths of the low-angle hillslopes at the site. Small thermokarst pits occurred in clumps, most frequently along the inner EML moraine (Thorson 1986). Additionally, thermokarst features were evident along paths of human disturbance, including roads and dogsled/ATV tracks. Across all thermokarst shapes, the average feature size was 25 m^2. The deepest thermokarst feature had a maximum depth of 3.6 m. Across the site, thermokarst features averaged 0.07 m deep at their deepest point and had an average

depth of 0.03 m. Erosion seemed to play a minor role in thermokarst formation as the slopes with high thermokarst activity were shallow (3-10°) and exposure of mineral soils or disturbance to plants was only observed in recently inundated thermokarst pits.

Across the entire study area, we observed subsidence (2017-2019) of 0.03 m in non-thermokarst areas ($p < 0.0001$) and 0.02 m in thermokarst edges ($p = 0.066$) but subsidence of 0.01 m in thermokarst centers was not significant ($p = 0.33$). The rate of subsidence did not differ statistically between any of the thermokarst classes (Figure S1). Using our GPS data at CiPEHR over the same time frame, we observed subsidence across all thermokarst classes, with thermokarst centers and thermokarst edges subsiding more quickly (0.05 m) than non-thermokarst areas (0.01, $p < 0.0001$). The magnitude of LiDAR-derived subsidence at CiPEHR was 0.01-0.02 m smaller than the GPS derived subsidence ($p < 0.0001$), but showed the same patterns across classes.

We found that thermokarst morphology varied by both feature size and shape (Figure 3). Small features were the most prevalent (51%) and prevalence declined exponentially as size increased. The largest class, 100,00 m^2 - 1 km^2, had a total of only 9 features (0.001%). For shape, the most compact features, which tended to be small thermokarst pits and ponds, were most prevalent (52%), and the least compact features, which tended to be extensive water tracks, were the least prevalent (1%). Thermokarst percent cover showed very different patterns than prevalence across size and shape classes. Mid-sized thermokarst features (1000 - 10,000 m^2) had the greatest extent (2%), while both larger and smaller features were less common. For shape, percent cover showed a pattern of exponential decay from the least compact features (5%) to the most compact features (0.1%). Percent volume of thermokarst features showed similar, but more pronounced, patterns to percent cover. Relatively large features (1000 - 10,000 m^2 and 10,000 -

100,000 m^2) had the highest percent volume (38% each), while smaller and larger features had lower percent volume. For shape, the least features had the highest percent cover by far (85%) and percent volume dropped exponentially, such that the most compact shape class accounted for very little of the thermokarst volume (<1%). Mean depth of thermokarst features varied considerably by size class, but very little by shape. Thermokarst feature classes smaller than 1000 m^2 all had a mean depth of less than 0.05 m, while thermokarst feature classes between 1000 m^2 and 1 km^2 all had mean depths near or greater than 0.15 m. In contrast, all thermokarst shape classes had a mean depth around or below 0.05 m, with only a slight tendency toward shallower features at shapes in between the two extremes.

4.3. EML Decadal Change

Within the EML watershed, we found a higher degree of thermokarst impact than across the study area as a whole. Within the watershed, 12%, or 1.3 km^2, of the landscape was impacted by thermokarst, compared to 7% within the larger study area, and exactly the same as in 2008. Much of the watershed was covered by water tracks and a small stream feeding into EML, which was likely responsible for the elevated thermokarst percent cover relative to the rest of the study area. Additionally, the watershed has a higher ratio of road miles to area than the rest of the study area and the road is flanked by thermokarst features for nearly its entire length. Finally, there are more dogsled/ATV tracks in the vicinity of the lake and road than in other regions of the study area, although these features cover much less area than water tracks.

Thermokarst percent cover and roughness varied considerably across the EC tower footprint, with higher thermokarst percent cover and roughness occurring N and NW of the tower (Figure 4). This trend was driven by a system of deeply incised water tracks primarily in the N and NW regions of the EC tower fetch and a patch of small thermokarst features in the NE region of the

fetch (Figure 2c, S3). There was a non-linear relationship between surface roughness and thermokarst. Surface roughness increased with increasing thermokarst to about 30% cover and then declined somewhat with greater thermokarst percent cover. Since 2008, we found that average microtopography at the EC tower increased by 1.62 cm (Belshe et al. 2012), which may indicate that the landscape is subsiding more quickly than older thermokarst features.

4.4. Response of CO_2 Fluxes to Abrupt Thaw

Abrupt thaw drove higher CO_2 release (Figure S4), with thermokarst percent cover being a strong predictor of all CO_2 fluxes (NEE, GPP, R_{eco}), particularly during the GS Day (Figure 5). All selected models included thermokarst percent cover, month, and the interaction between the two. Thermokarst percent cover explained more variation in GPP (r2 = 0.56) and R_{eco} (GS Day: r2 = 0.49; NGS/Night: r2 = 0.24) than in NEE (GS Day: r2 = 0.39; NGS/Night: r2 = 0.22). During the GS Day, GPP and R_{eco} increased with thermokarst percent cover, with the response peaking during the growing season. During the NGS/Night, there was a noticeable seasonal trend in the relationship between thermokarst percent cover and R_{eco}, with very little impact of thermokarst on R_{eco} during the winter and early spring and stimulation of R_{eco} by thermokarst during the GS and early fall, particularly August and October. During the GS Day, abrupt thaw stimulated GPP more than R_{eco}, resulting in higher carbon uptake, particularly during peak growing season in July. During the NGS/Night, however, abrupt thaw stimulated carbon release in all months except February. In February, the relatively strong stimulation of the CO_2 sink by thermokarst appears to be confounded by wind speed and wind direction. This was because winter storms, which release CO_2 trapped in snow or cracks in the soil, primarily came from the SW which happens to have low thermokarst percent cover. On an annual scale, the impact of

abrupt thaw on R_{eco} was stronger than the impact on GPP, resulting in greater CO_2 release (Figure S4).

4.5. Response of CH_4 Fluxes to Abrupt Thaw

Abrupt thaw was a significant, but small, predictor of CH_4 fluxes, with the strongest relationship occurring during the growing season and fall (Figure 6, r2 = 0.071). For all months except January and February we found that CH_4 release increased with thermokarst percent cover, with the strongest relationships between June and October, and weaker relationships in the winter and early spring. In contrast, in January and February CH_4 release was exceptionally high at low thermokarst percent cover, which was largely due to high wind speed during storms coming from directions with low thermokarst percent cover, likely releasing CH_4 trapped in snow. During the GS Day, CH_4 pulse release showed some evidence of being influenced by thermokarst percent cover, as higher release tended to occur from areas of higher thermokarst percent cover (Figure S5), but soil moisture had a stronger influence on CH_4 pulse release. During the NGS, wind speed had a strong influence on CH_4 pulse release and thermokarst percent cover did not appear to play a strong role.

5. Discussion

5.1. Thermokarst Morphology and Impact on Carbon Fluxes

We found that at least 7% of the site was impacted by thermokarst and the impact of these features on carbon thaw and flux varied by thermokarst size and shape (Figure 3). Small thermokarst pits, most common on the inner EML moraine and previously glaciated low-angle slopes to the East of the moraine, were by far the most numerous thermokarst features. Given the glacial history of these areas, these features could be the result of the thaw of buried glacial ice based on the glacial history of the site (Harris and Murton 2005; Thorson 1986) and the presence

of glacial till (Osterkamp et al. 2009). By area, a much smaller number of larger, less compact features accounted for the vast majority of thermokarst impacted land. These features tended to be extensive systems of water tracks which were longer and deeper than the smaller pits. Because of this, these features had an outsized impact on the ecosystem by thawing more permafrost and the carbon it contains. At this site, we previously found that subsidence associated with abrupt thaw can thaw carbon at twice the rate expected from that of gradual thaw alone (Rodenhizer et al. 2020). With 7% of the landscape currently undergoing abrupt thaw, this could mean that, at the landscape-level, permafrost carbon is thawing 7% faster than increases in active layer thickness indicate. It is important to note, however, that this rate will change as thaw progresses into deeper soils with lower carbon content.

Thermokarst percent cover, in combination with month, explained between 22% and 56% of GPP, R_{eco}, and NEE, indicating that it captures some of the long-term variability associated with a wide variety of environmental predictors of carbon fluxes, although it only explained 7% of CH_4 flux (Figure 5). Given that carbon fluxes respond to many environmental variables in complex ways, the high r2 values in our linear models indicated that thermokarst was a proxy variable for several environmental variables, with the ability to explain ~50% of GS Day GPP and R_{eco} when month is also considered. Because thermokarst typically occurs over the course of years to decades, it may be a proxy for environmental variables such as deep soil temperature, talik formation, and nutrient availability, which exert slower, long-term control on fluxes than environmental variables like light level or air temperature, which can change drastically throughout the course of a day (Belshe et al. 2012; Lee et al. 2011; Lee, Schuur, and Vogel 2010).

Net carbon dioxide release was promoted by abrupt thaw at this site (Figure S4). Changes in NEE depend on the balance between GPP and R_{eco}, both of which can shift in divergent directions in response to abrupt thaw. Although we found that plant growth was promoted within thermokarst features during the growing season daytime, resulting in higher annual GPP, it was not sufficient to offset higher R_{eco} at night and during the non-growing season (Figure S4, Figure 7). This reinforces the idea that winter respiration rates have a very important role in determining annual CO_2 balance across the northern permafrost region (Natali et al. 2019; Watts et al. 2021). This site is already a CO_2 source in most years (Plaza et al. 2019; T. Schuur et al. 2021), due to the combined impacts of gradual and abrupt thaw. Our findings isolated the response of CO_2 flux to abrupt thaw abrupt thaw and indicate that this site is likely to become an even stronger CO_2 source as abrupt thaw expands. Higher NEE (more release of CO_2) from thermokarst features has also been found in previous studies at EML (Trucco et al. 2012; Vogel et al. 2009) and elsewhere (Cassidy, Christen, and Henry 2016; Eugénie S. Euskirchen et al. 2017) and in modeling studies (Parazoo et al. 2018; Turetsky et al. 2020), supporting our results. At the same time, the opposite pattern (lower NEE) has also been documented at EML (Lee et al. 2011) and elsewhere (E. S. Euskirchen et al. 2014; Wickland et al. 2020). The varied net CO_2 response of thermokarst features across sites is likely due in part to thermokarst morphology, which regulates environmental conditions such as soil temperature (Lee et al. 2011; Mauritz et al. 2017), soil moisture (Eugénie S. Euskirchen et al. 2017; Mauritz et al. 2017; Rodenhizer et al. 2020), and rates of erosion (Abbott and Jones 2015). Because these changes in environmental conditions can result in either increases or decreases in GPP and/or R_{eco}, the overall effect on NEE is highly variable, and the opposite responses observed across sites and through time is not unexpected. Despite the wide variability of NEE response to abrupt thaw, the balance of the evidence

suggests that the ability of abrupt thaw to rapidly thaw permafrost carbon results in substantial release of carbon that was previously stored in permafrost soils.

Abrupt thaw promoted higher GPP during the growing season (Figure 5), as highly-vegetated water tracks were the most extensive form of thermokarst. Although we have previously observed die-off of plants in young, recently inundated thermokarst features at this site (Rodenhizer et al. 2020; M. Taylor et al. 2021), GPP was stimulated by abrupt thaw in the current study, likely due to the response of extensive (and typically older) water tracks (Curasi, Loranty, and Natali 2016). Higher GPP in water tracks at this site was likely due to warmer soil temperatures (Lee et al. 2011), the release of nutrients from the deepening thaw front (Hewitt et al. 2019; 2018; Salmon et al. 2016), low rates of erosion allowing the establishment of wet-adapted plants (M T Jorgenson and Osterkamp 2005). Because this site is relatively wet, we do not believe that the alleviation of drought in thermokarst features played a strong role in increasing GPP, as was observed in Euskirchen et al. (2017). Since water tracks are the most widespread thermokarst morphology at our site, this site is likely seeing an overall increase in photosynthesis and vegetation biomass as abrupt thaw progresses.

Abrupt thaw promoted R_{eco} year-round (Figure 5), outpacing increases in GPP and resulting in the loss of old permafrost carbon (Figure S4). Increases in R_{eco} were due partially to higher root respiration associated with higher plant growth in water tracks (Hicks Pries et al. 2016; 2015; 2013; Lee, Schuur, and Vogel 2010). However, increasing year-round heterotrophic respiration must be responsible for the overall shift to higher net carbon release, despite its smaller magnitude. This is because carbon release through autotrophic respiration offsets only about half of carbon uptake through photosynthesis (Collalti and Prentice 2019). The increase in heterotrophic respiration is likely due to higher availability of carbon as a microbial energy

source, increasing soil temperatures, and the presence of taliks, which provide unfrozen soil conditions year-round (Natali et al. 2019; E. F. Pegoraro et al. 2020). Although erosion can limit R_{eco} through the rapid export of permafrost carbon (Abbott and Jones 2015), this did not appear to play a noticeable role due to the low rates of erosion at this site. Because this site is relatively wet and prone to anaerobic conditions (which can protect soil carbon from mineralization), the increase in heterotrophic respiration has previously been shown to be particularly strong during dry years when waterlogging is alleviated (E. F. Pegoraro et al. 2020). Some of the carbon being respired from thermokarst has likely been stored in permafrost for hundreds to thousands of years (Hicks Pries, Schuur, and Crummer 2013; E. Pegoraro et al. 2019; E. F. Pegoraro et al. 2020), particularly as the thaw front deepens rapidly into layers of older carbon.

Abrupt thaw promoted higher CH_4 release nearly year-round (Figure 6), likely due to anoxic conditions in waterlogged soils and longer periods of unfrozen conditions in thermokarst (M. A. Taylor et al. 2018; M. Taylor et al. 2021). Unlike the varied responses of NEE to thermokarst, there is high agreement that CH_4 release is promoted by abrupt thaw in the literature (Burke et al. 2019; Cooper et al. 2017; Kutzbach, Wagner, and Pfeiffer 2004; Lindgren et al. 2016; Nauta et al. 2015; Wickland et al. 2020). We found that the stimulation of CH_4 release by abrupt thaw was strongest between spring thaw and early winter. Although CH_4 production occurs in taliks throughout the winter, it is often trapped by snow cover until spring thaw, explaining the strong response of CH_4 flux to abrupt thaw that we observed in March-May (Pirk et al. 2017; Raz-Yaseef et al. 2017; Song et al. 2012; Tagesson et al. 2012; M. A. Taylor et al. 2018; Tokida et al. 2007). Additionally, warmer soil temperatures and the presence of taliks in thermokarst features promotes more rapid and deeper thaw throughout the growing season (E. A. G. Schuur et al. 2007). Combined with higher soil moisture increasing the likelihood of anoxic

conditions in thermokarst depressions (E. A. G. Schuur et al. 2007), this provides conditions prone to CH_4 production (M. A. Taylor et al. 2018). During the early winter, an increase in the length of the zero curtain (the time during freeze-up when soils are unfrozen but near 0°C), particularly in thermokarst features, could be allowing methanogenesis to continue later into the non-growing season (Arndt et al. 2019; Bao et al. 2021; Zona et al. 2016). The increase in CH_4 release has the potential to shift the radiative forcing of the site significantly, even though CH_4 fluxes are much smaller than CO_2 fluxes. Methane is 45 times more powerful a greenhouse gas than CO_2 over 100 years (Myhre, Shindell, and Pongratz 2014; Neubauer and Megonigal 2015), meaning that a small shift from CO_2 production to CH_4 production under wet soil conditions can have a large impact on the radiative forcing of carbon emissions. As CH_4 is responsible for 61% of the radiative forcing due to carbon emissions at this site (M. A. Taylor et al. 2018), the stimulation of CH_4 release by abrupt thaw is likely to have a large impact on the radiative forcing of the site, despite the smaller magnitude of fluxes and weaker relationship. Overall, we found that ecological changes associated with abrupt permafrost thaw are playing an important long-term role in exacerbating net carbon release, even as GPP increases.

5.2. Subsidence and Thermokarst Development Through Time

Across the study site, we saw evidence of expansion and initiation of thermokarst, rather than deepening of established features. Greater extent of thermokarst resulted in lower surface roughness and could indicate that hydraulic connectivity is slowly increasing at the site, as thermokarst features expand and taliks interlink (Devoie et al. 2019). This could eventually result in better drainage and drier surface soils (Teufel and Sushama 2019). We draw on three lines of reasoning to support the conclusion that the extent of abrupt thaw is increasing, which are outlined here and described in detail in the following paragraphs. First, across the site,

subsidence occurred most rapidly in areas not classified as thermokarst and old thermokarst features did not subside noticeably. However, small, recently initiated thermokarst features (~1 decade old or less) within CiPEHR subsided rapidly. Second, aerial imagery dating to 1954 and anecdotal evidence at the site indicates the initiation of thaw pits and the expansion of water tracks upslope through time. Additionally, the observed lack of change in thermokarst extent between Belshe et al. (2013) and the current study is explained by differences in methodology resulting in the current study being more conservative in the classification of thermokarst. Third, a slight increase in microtopography from Belshe et al. (2012), despite widespread subsidence, is consistent with the initiation of new thermokarst features and the expansion, but not deepening, of old thermokarst features.

Across the study site, the lack of subsidence in thermokarst centers between 2017 and 2019 indicated that pre-existing thermokarst features did not deepen significantly, while the highest rate of subsidence in non-thermokarst areas indicated that there may be thermokarst initiation and expansion occurring (Figure S1). The lack of subsidence in thermokarst centers across the site may indicate that these older features have already thawed near-surface permafrost with the highest ice content and reached a more stable depth (French and Shur 2010). This supports the idea that older thermokarst features were primarily expanding rather than deepening. In addition, new features may have formed across the landscape, contributing to the higher rate of subsidence in non-thermokarst areas. At CiPEHR, however, the rates of subsidence indicate they were both deepening and expanding, as thermokarst features were initiated recently (experimental warming started in 2008), and were still actively forming (Osterkamp et al. 2009). Our inability to statistically distinguish the rate of subsidence between thermokarst classes using LiDAR data may be partially due to the opposite responses of thermokarst features of different

ages and partially a consequence of insufficient image resolution to precisely distinguish thermokarst edges.

Documenting change in thermokarst over a decade was a challenge because methodological differences resulted in a more conservative classification than in Belshe et al. (2013). There is evidence of thermokarst expansion at the site from aerial photography dating back to 1954 in tandem with both rising air and permafrost temperatures (Osterkamp et al. 2009). On the ground more recently, we have documented increases in active layer thickness and subsidence of over 1 cm yr -1 (Rodenhizer et al. 2020) and seen the expansion of water tracks on the ground (necessitating the relocation of the EC tower). Additionally, our classification indicated that water tracks extended farther upslope than in 2008 and we found a larger number of small features, which could indicate thermokarst expansion and initiation. However, this was counterbalanced by a larger number of non-thermokarst cells within thermokarst features in the overall extent, which seems to be due primarily to differences in the theoretical approach to thermokarst classification. Belshe et al. (2013) used spectral data to classify thermokarst based primarily on the visible changes to vegetation associated with thermokarst. This means the presence of thicker, greener vegetation in water tracks (Curasi, Loranty, and Natali 2016), resulted in a thermokarst classification with fewer gaps in their study. In our study, on the other hand, areas within a thermokarst feature would get classified as non-thermokarst if their elevation was even slightly higher than the surrounding landscape, despite increased vegetation productivity that would indicate the location is undergoing abrupt thaw. While resolution must also play some role in the different distribution of thermokarst between the two studies, we were able to confirm that resolution did not impact the overall extent by finding very little change in thermokarst extent when we resampled our classification to 3 m resolution (as in Belshe et al.

2013). Taken together, all of this leads us to conclude that our thermokarst classification is more conservative than that of Belshe et al. (2013) and that thermokarst percent cover within the EML watershed has likely exceeded 12% (as found in both studies) in the past decade.

The slight increase in microtopography since 2008 could also be an indication of the increasing extent of thermokarst with limited deepening of older features (Figure S3). As thermokarst features have expanded and the landscape as a whole has subsided, the average landscape elevation has decreased, while thermokarst features may no longer have been subsiding where ground ice had already thawed (Figure S1). Since microtopography was calculated as the average neighborhood elevation subtracted from the local elevation, a decrease in average elevation necessarily results in an increase in microtopography for cells which subsided more slowly than the landscape average. Therefore, we conclude that the slight increase in microtopography was an indication of the increasing ubiquity of thermokarst at the site.

5.3. Discussion of validation and utility

The thermokarst detection algorithm presents a unique opportunity for the detection of thermokarst anywhere a single ground elevation map is available, rather than relying on change detection from two or more elevation maps at different time points. Removing the necessity of repeat-imagery to identify thermokarst means that this method could be applied to a broader range of sites than is otherwise possible, as airborne LiDAR availability is limited and satellite imagery does not achieve the necessary spatial resolution (Kääb 2008; Westermann et al. 2015). However, applying the analysis on multiple DTMs and combining the classifications into one result, as we did, can help alleviate errors. Additionally, it may be possible to scale this method to larger regions as access to elevation data improves. Unfortunately, the ArcticDEM (Porter et al. 2018) is not suitable for detecting many types of thermokarst features, as it uses the elevation

of the vegetation canopy rather than the ground surface. It could, however, potentially be used to detect features with high levels of erosion or inundation that have limited vegetation or features which are deeper than the tallest vegetation. This would build upon our current understanding of the distribution of thermokarst, as circumpolar studies of thermokarst have not yet mapped discrete features. There are, however, some limitations to the thermokarst detection algorithm. First,a high-resolution elevation data set is required, because poor resolution could lead to the detection of larger landscape features, like valleys, rather than thermokarst, as in the case of the similar topographic position index (De Reu et al. 2013). In this study, we used elevation at 1 m resolution. We expect it would be possible to use up to 10 m resolution data to detect large features, based on the fact that thermokarst features 100 m^2 or smaller covered only ~1.5% of our site (Figure 3). These larger features were responsible for the vast majority of permafrost thaw, indicating that they may play a larger role in carbon dynamics, despite the prevalence of small thermokarst pits. Second, the necessity of high-resolution data requires more processing power than is readily available at this point, although Google Earth Engine could alleviate this issue. Despite these limitations, the increasing availability of high-resolution elevation data across the circumpolar region means that this method can be applied across an increasingly broad range and shows promise for improving our understanding of the distribution and extent of thermokarst across the Arctic.

6. Conclusion

Abrupt thaw is contributing to carbon release above that caused by gradual thaw at EML. At least 7% of the site as a whole and at least 12% of the EML watershed is undergoing abrupt thaw, with evidence of new thermokarst initiation and expansion driving abrupt thaw processes rather than deepening of older thermokarst features. We identified a large number of small,

relatively shallow thermokarst pits, but deeper and larger water tracks were more extensive and were responsible for thawing more permafrost than small features. There was strong evidence that abrupt thaw correlated with increases in both GPP and R_{eco}, but because R_{eco} responded more strongly to thaw, the net result was higher CO_2 release. This is likely due to the high percent cover of water tracks, which tend to have much thicker vegetation, enhancing photosynthesis during the GS and ecosystem respiration both during and outside the GS. Additionally, abrupt thaw accelerated the release of CH_4 in nearly all months, which is responsible for about 61% of the greenhouse gas radiative forcing of the site (M. A. Taylor et al. 2018). As the climate continues to warm, thermokarst features will expand to cover more of the landscape, thaw more permafrost carbon, and push more permafrost ecosystems towards becoming carbon sources for the first time in thousands of years. With many modeling studies and field studies, including this one, indicating that abrupt thaw could increase carbon release significantly, it is imperative to understand where abrupt thaw is occurring and to work to include abrupt thaw processes in Earth System Models.

Acknowledgements

This study made use of imagery that was collected as part of the Arctic-Boreal Vulnerability Experiment. Resources supporting this work were provided by the NASA High-End Computing Program through the NASA Center for Climate Simulation at Goddard Space Flight Center. Particular thanks to Elizabeth Hoy and Tristan Goulden for their help with ABoVE and NEON datasets.

Funding

This work was supported by the NSF: NNA: LTREB: The Arctic Carbon and Climate (ACCLIMATE) Observatory: Tundra Ecosystem Carbon Balance and Old Carbon Loss as a Consequence of Permafrost Degradation (Award # 1754839). Supplemental funding provided by the Bonanza Creek LTER, a partnership between the University of Alaska Fairbanks, and the U.S. Forest Service. Significant funding for collection of these data was provided by the National Science Foundation Long-Term Ecological Research program (NSF Grant numbers DEB-1636476, DEB-1026415, DEB-0620579, DEB-0423442, DEB-0080609, DEB-9810217, DEB-9211769, DEB-8702629) and by the USDA Forest Service, Pacific Northwest Research Station (Agreement # RJVA-PNW-01-JV-11261952-231).

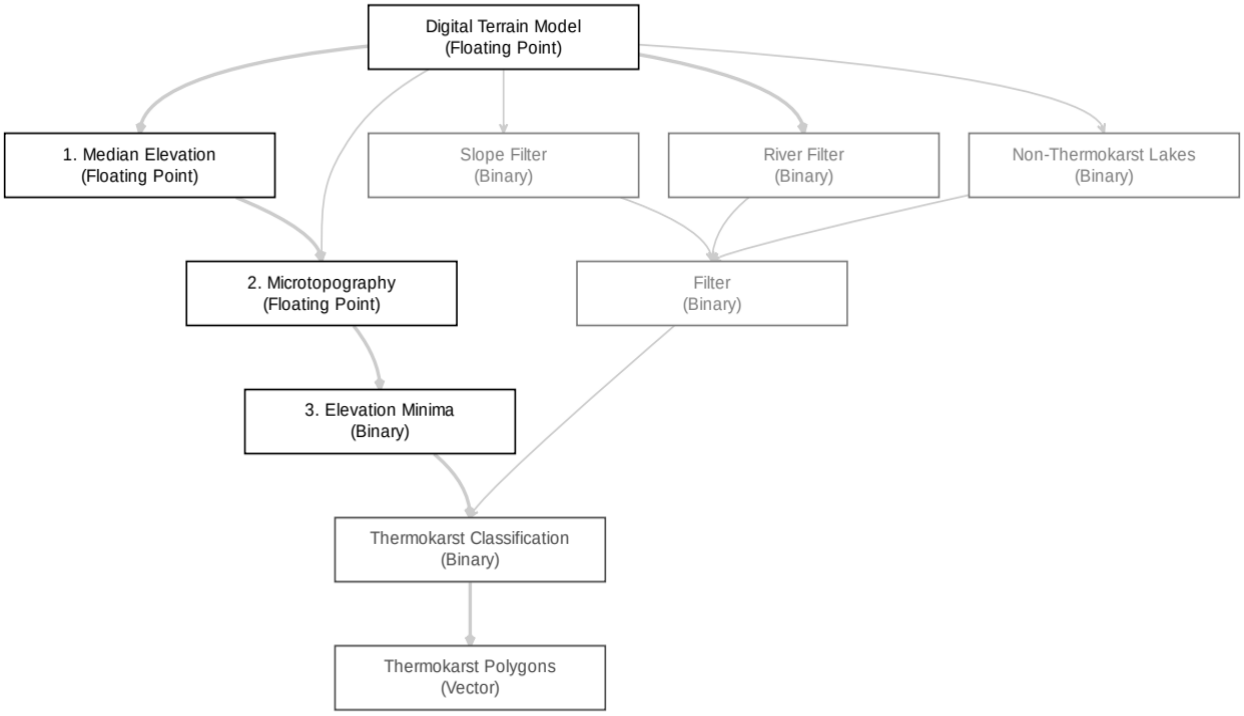

Figure 3.1. A conceptual diagram of the thermokarst detection algorithm (black), which is available as an R package, with the non-thermokarst landscape filters (light gray) and final processing steps (dark gray), neither of which are included in the R package. As part of the R package, 1) median elevation is calculated for each cell of a DTM using a moving circular neighborhood (we tested 15, 25, and 35 m radii individually and in combination), 2) microtopography is calculated by subtracting the median elevation from the DTM, and 3) elevation minima are classified as microtopography values below a threshold (we tested 0 cm, local elevation equal to the median elevation, and -5 cm, local elevation 5 cm below the median elevation). As part of the post-processing not included in the R package, 1) steep slopes, deeply incised rivers, and non-thermokarst lakes were filtered out from the elevation minima, 2) combinations of thermokarst classifications were created to determine the best combination of neighborhood size and threshold value to detect different thermokarst sizes and, 3) the best classification was converted to vector format for analysis.

Table 3.1. Accuracy of the thermokarst detection algorithm when using the best combination of neighborhood sizes. “Ground” indicates the number of cells which are of that class on the ground and “map” indicates the number of cells which are of that class on the map. User’s accuracy is the accuracy from the point of view of a map user: how likely a class shown on the map will be present on the ground. The commission error is the complement of this value (100% - user’s accuracy): how likely a class on the map is classified incorrectly. Producer’s accuracy is the accuracy from the point of view of the map maker: how likely a real feature on the ground is to be classified correctly on the map. The omission error is the complement of this value (100% - producer’s accuracy): how likely a real feature on the ground is misclassified.

		Ground		
		Non-Thermokarst	Thermokarst	Total
Map	Non-Thermokarst	80	36	116
	Thermokarst	21	63	84
	Total	101	99	200
User’s Accuracy			**Commission Error**	
Non-Thermokarst	80/116 =	69.0%	31.0%	
Thermokarst	63/84 =	75.0%	25.0%	
Producer’s Accuracy			**Omission Error**	
Non-Thermokarst	80/101 =	79.2%	20.8%	
Thermokarst	63/99 =	63.6%	36.4%	
Overall Accuracy	**71.5%**			

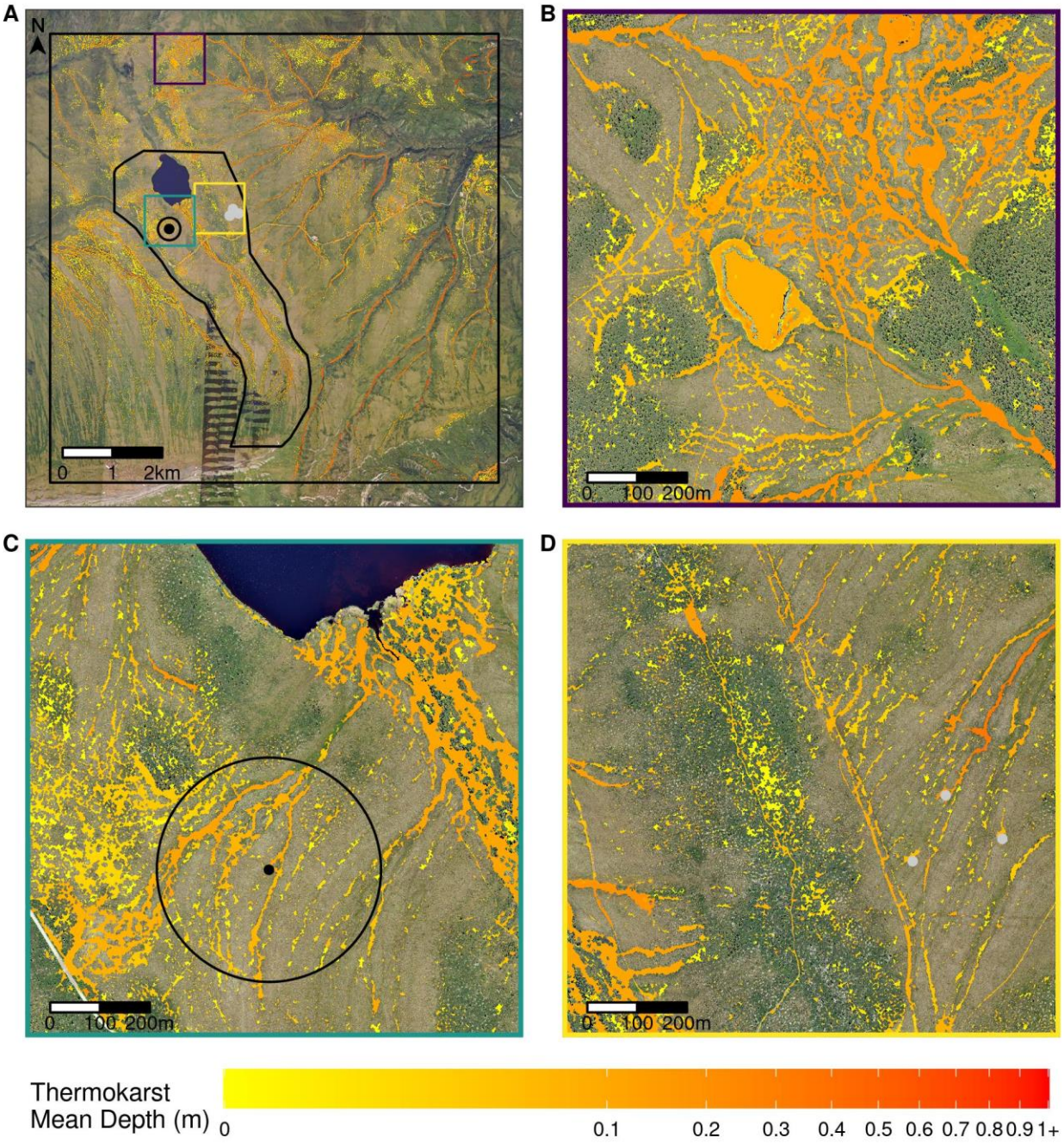

Figure 3.2. A) The mean depth of thermokarst features (2017-2019) across the study extent (9 x 9 km black box). The EML watershed is outlined in black with the EC tower and approximate tower footprint shown as a point within a circle. The three gray points show the location of the three experimental blocks at CiPEHR. Colored squares indicate insets shown in B-D. B) The largest thermokarst pond we identified in one of the most heavily thermokarst affected areas within the study extent. In addition to naturally formed features, dogsled/ATV tracks are visible

throughout the area. 26% of the inset was classified as thermokarst. C) Thaw ponds and water tracks which drain into EML surrounding the EC tower. 19% of the inset was classified as thermokarst. D) Extensive small thermokarst pits on the terminal moraine East of EML (the greener, shrubby area), dogsled/ATV tracks, and thermokarst pits caused by soil warming at CiPEHR. 11% of the inset was classified as thermokarst.

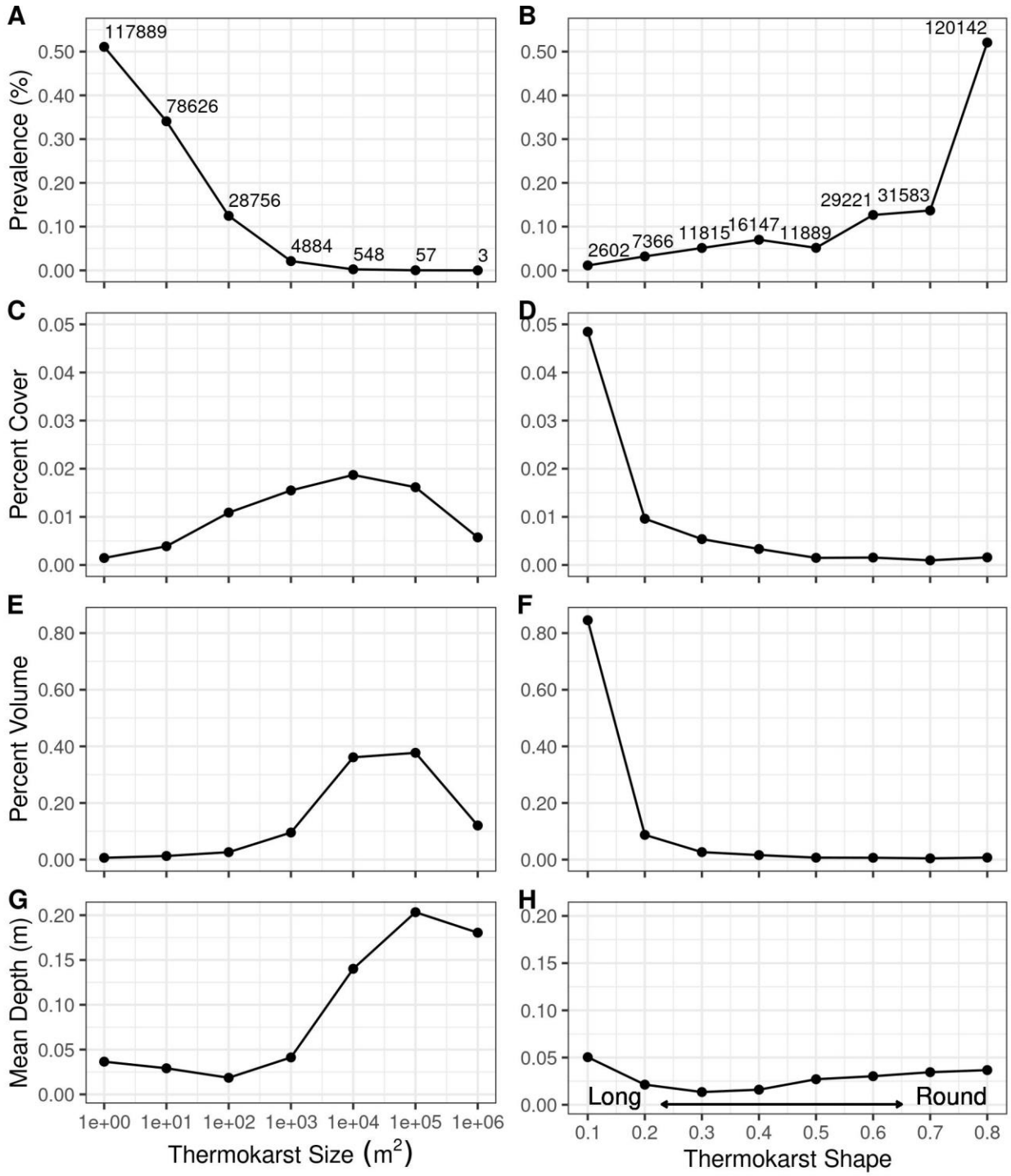

Figure 3.3. A & B) Prevalence (percent of features by count), C & D) percent cover (percent cover of thermokarst within that class relative to the entire study area - the sum of the classes is overall percent cover of 7%), E & F) percent volume, and G & H mean depth of thermokarst features by size and shape class. Labels in A & B indicate the number of features within each class.

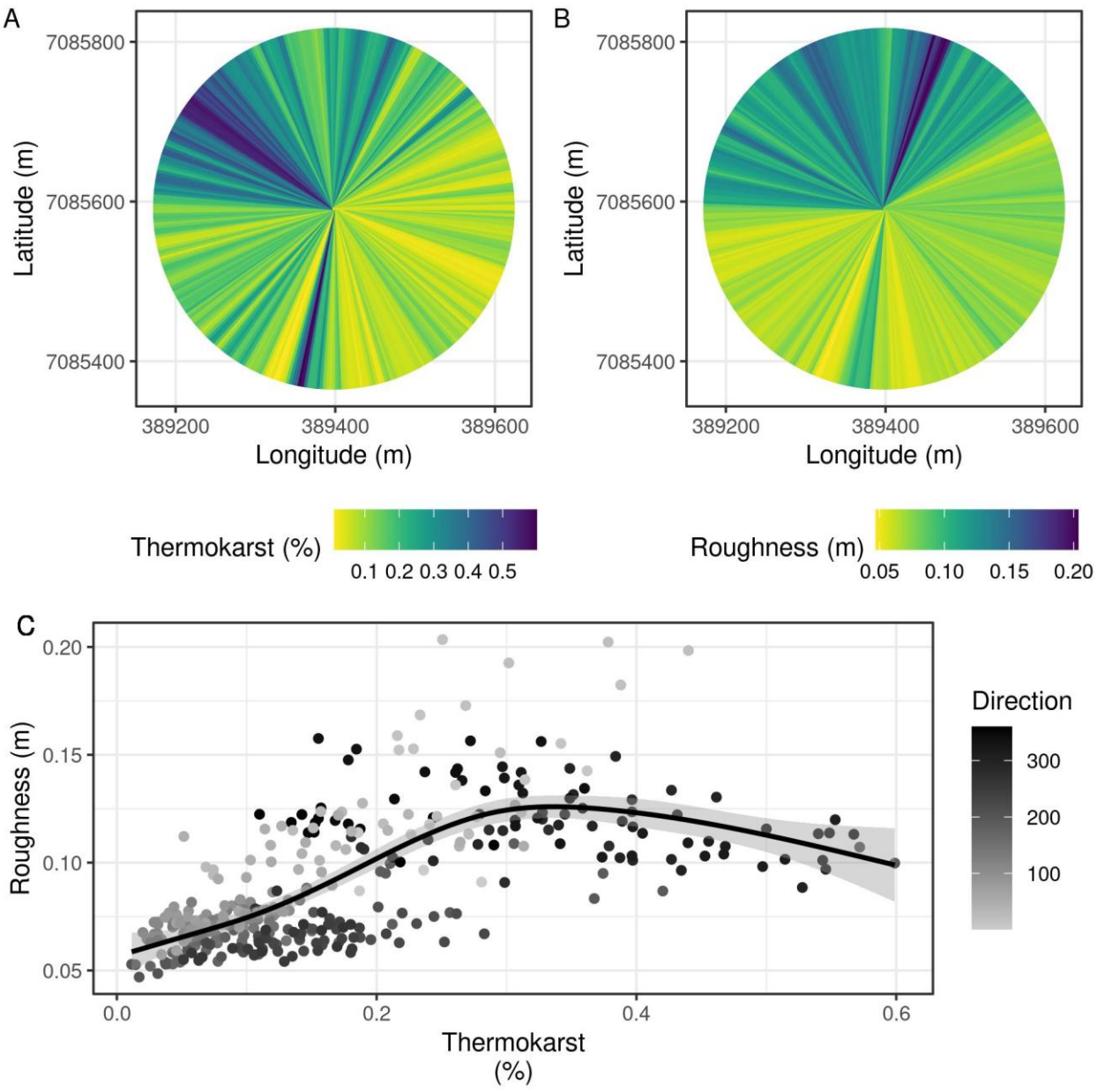

Figure 3.4. A) Thermokarst percent cover in 1° increments at the EC tower, B) surface roughness in 1° increments at the EC tower, and C) the relationship between percent thermokarst cover and surface roughness at the EC tower, with the grayscale indicating the direction from which the measurement came (relative to the tower).

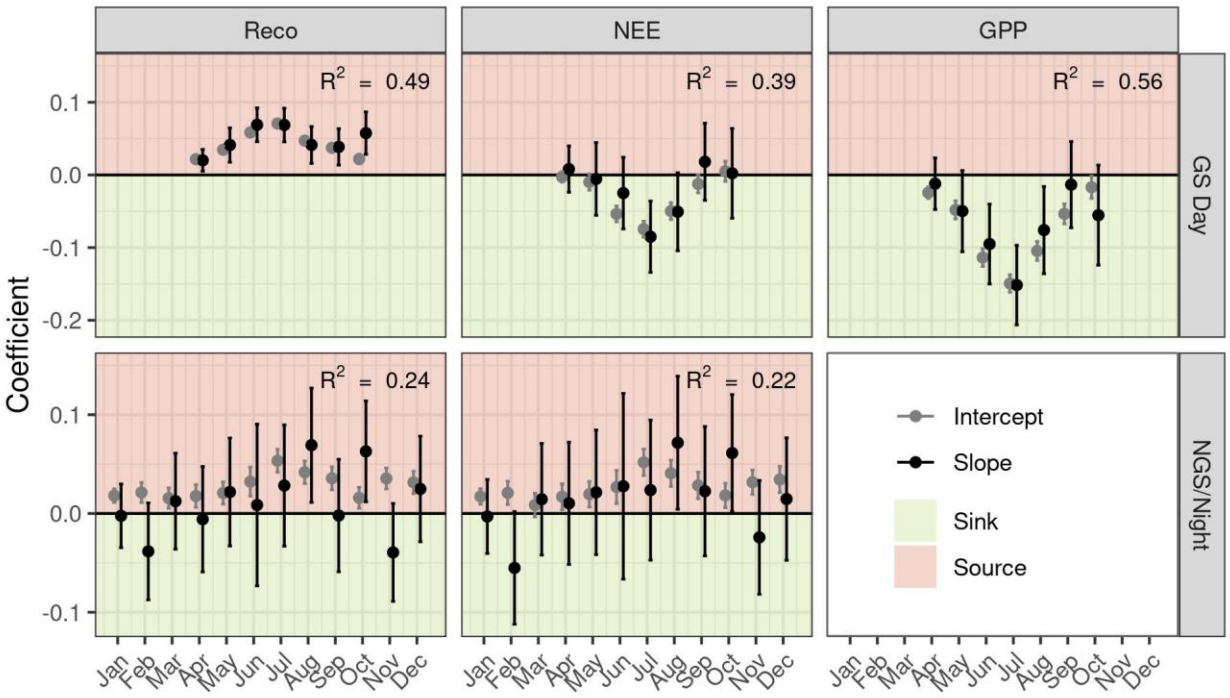

Figure 3.5. Coefficients for the linear regressions of GPP, NEE, and R_{eco} by thermokarst percent cover. Positive intercepts indicate a source when no thermokarst is present and negative intercepts indicate a sink when no thermokarst is present. Positive slopes indicate that fluxes trend toward a larger source or smaller sink as thermokarst percent cover increases, depending on the sign of the flux. Negative slopes indicate that fluxes trend toward a smaller source or larger sink as thermokarst percent cover increases.

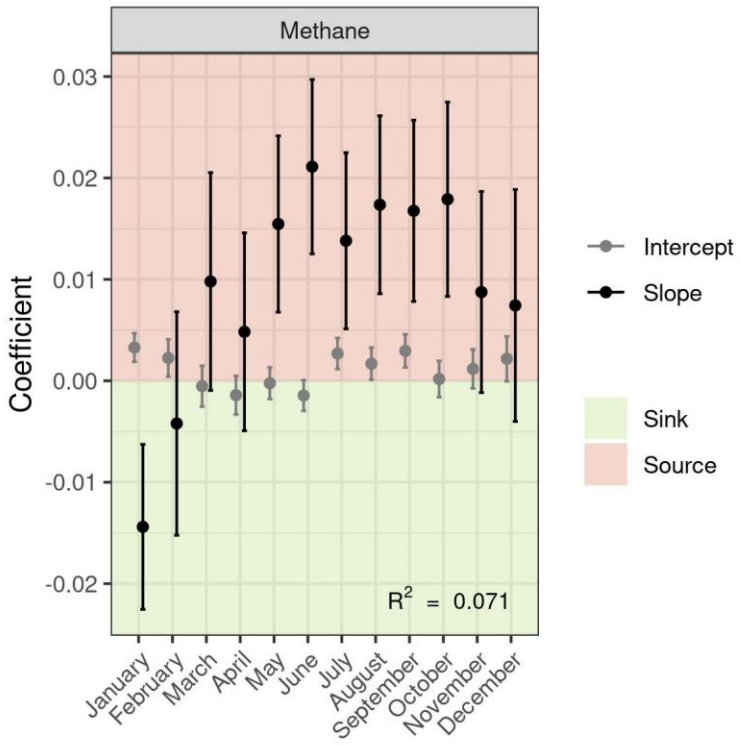

Figure 3.6. Coefficients for the linear regression of non-pulse CH_4 fluxes by thermokarst percent cover and month. Positive values for intercepts indicate a source when no thermokarst is present and negative values for intercepts indicate a sink when no thermokarst is present. Positive values for slopes indicate that fluxes trend toward a larger source or smaller sink as thermokarst percent cover increases, depending on the sign of the flux. Negative values for slopes indicate that fluxes trend toward a smaller source or larger sink as thermokarst percent cover increases.

CHAPTER 4: DIVERGENT HYDROLOGIC RESPONSES TO ABRUPT PERMAFROST THAW DRIVE SPATIALLY HETEROGENEOUS CARBON DIOXIDE FLUXES

Heidi Rodenhizer[a], Marguerite Mauritz[b], Susan M. Natali[c], Meghan A. Taylor[d], Gerardo Celis[e], Stephanie Kadej[a], Allison K. Kelley[a], Emma R. Lathrop[a], Elaine F. Pegoraro[f], Verity G. Salmon[g], Elizabeth E. Webb[h], Edward A. G. Schuur[a]

[a]Center for Ecosystem Science and Society, Northern Arizona University, Flagstaff, AZ

[b]Biological Sciences, University of Texas at El Paso, El Paso, TX

[c] Woodwell Climate Research Center, Falmouth, MA

[d] Rubenstein School of the Environment and Natural Resources, University of Vermont, Burlington, VT

[e]Department of Anthropology, University of Arkansas, Fayetteville, AR

[f] Climate and Ecosystem Sciences Division Lawrence Berkeley National Laboratory, Berkeley, CA

[g] Environmental Science Division and Climate Change Science Institute, Oak Ridge National Laboratory, Oak Ridge, TN

[h]School of Natural Resources and Environment, University of Florida, Gainesville, FL

Abstract

Permafrost thaw causes the seasonally thawed active layer to gradually deepen, mobilizing carbon and nutrients and causing Arctic ecosystems to become smaller carbon sinks relative to historical conditions or even to become carbon sources. Additionally, ground subsidence initiated by ice loss as permafrost thaws can cause these soils to thaw and collapse abruptly. Abrupt permafrost thaw can both accelerate carbon and nutrient mobilization relative to gradual thaw and rapidly shift soil moisture, with potentially opposing impacts on carbon fluxes. The uncertainty of hydrologic trajectories during and following thaw is one aspect which makes it difficult to predict the effect of abrupt thaw in suppressing or exacerbating carbon losses. In this study, we investigated the role of shifting hydrologic conditions in controlling growing season carbon dioxide fluxes during a 13 year permafrost warming experiment that initiated abrupt thaw. The active layer deepened differentially across treatments, leading to variable rates of subsidence and the formation of thermokarst depressions. In turn, differential subsidence caused a gradient of moisture conditions, with some plots becoming consistently inundated within thermokarst depressions and others exhibiting generally dry, but more variable soil moisture conditions outside of thermokarst depressions. Consistently wet conditions in the top 15 cm suppressed gross primary productivity and ecosystem respiration, resulting in lower growing season net ecosystem exchange (lower carbon uptake), while intermittently dry conditions in the top 15 cm promoted both gross primary productivity and ecosystem respiration with an overall increase in net ecosystem exchange (higher C uptake). On an annual basis, however, we found that both wet plots and dry plots released carbon, because abrupt thaw increased winter heterotrophic respiration. These findings indicate that Earth system models, which do not simulate subsidence and predict consistently drier active layer conditions, likely overestimate

growing season carbon uptake and underestimate winter respiration in abruptly thawing landscapes.

1. Introduction

1.1. Abrupt Thaw and the Permafrost Carbon Feedback

Globally, permafrost soils contain 1,440-1,600 Pg carbon (Schuur et al., 2018), which is about half of the global soil carbon stock (Hugelius et al., 2014; Köchy et al., 2015), and about twice as much carbon as is found in the atmosphere (Houghton, 2007). Permafrost soils accumulated carbon slowly over thousands of years due to frozen conditions that inhibit microbial decomposition (Ping et al., 2015; Schuur et al., 2008). However, temperatures in the Arctic are rising 2.5x faster than the global average (Ballinger et al., 2021) causing permafrost temperatures to rise and the active layer (seasonally thawed surface soil) to deepen at many sites (Biskaborn et al., 2019; M. T. Jorgenson et al., 2006; Luo et al., 2016; Nyland et al., 2021; Romanovsky et al., 2010), introducing previously frozen carbon to the contemporary carbon cycle. In an escalating response known as the permafrost carbon feedback, newly thawed permafrost carbon is decomposed and released to the atmosphere as the greenhouse gasses CO_2 and CH_4, leading to further warming(Schuur et al., 2008, in review; Schuur & Mack, 2018).

Permafrost can thaw both gradually, as the active layer deepens incrementally year after year, and abruptly, as ice, which provides structural support within the soil profile, melts and the ground surface subsides. Where abrupt thaw occurs, differential subsidence across the landscape can lead to the formation of thermokarst depressions over the course of hours to years (Kokelj & Jorgenson, 2013; Schuur & Abbott, 2011); in this paper we will use the term “abrupt thaw” to refer to rapid, differential subsidence generally, while thermokarst will be used to refer to specific depressions caused by abrupt thaw. While this process is a natural part of permafrost

ecosystems, the rate and extent of abrupt thaw are increasing due to climate change (Farquharson et al., 2019; M. T. Jorgenson et al., 2006, 2020; Kanevskiy et al., 2017; Lantz & Kokelj, 2008; Lara et al., 2016; Swanson, 2021; Veremeeva et al., 2021; Ward Jones et al., 2019). Although abrupt thaw is expected to occur in only about 20% of the permafrost region, these areas have exceptionally carbon rich soils and are believed to contain about 50% of total circumpolar permafrost carbon (Olefeldt et al., 2016). Abrupt thaw could therefore rapidly mobilize large stocks of permafrost carbon, potentially doubling the permafrost carbon feedback (Turetsky et al., 2020). However, concurrent plant disturbance and shifts to nutrient availability and hydrologic conditions make it difficult to predict the carbon cycle response to abrupt thaw across sites (M. T. Jorgenson & Osterkamp, 2005; Kokelj & Jorgenson, 2013; Lawrence et al., 2015; Natali et al., 2021; Olefeldt et al., 2016).

The effect of abrupt thaw on the carbon cycle varies considerably across sites due to the differential response of plant and microbial communities to variable shifts in environmental conditions (Abbott & Jones, 2015; Cassidy et al., 2016; Euskirchen et al., 2017; Jensen et al., 2014; Lee et al., 2011; Vogel et al., 2009). The overall impact of abrupt thaw on net ecosystem exchange (NEE; the net exchange of CO_2 between an ecosystem and the atmosphere) depends on the balance between gross primary productivity (GPP; the total amount of CO_2 fixed through photosynthesis) and ecosystem respiration (R_{eco}; the total amount of CO_2 respired by autotrophs and heterotrophs): $NEE = GPP - R_{eco}$. GPP can be suppressed or promoted by abrupt thaw through a number of environmental changes. These environmental changes include increases in nutrient availability (higher GPP), increases in soil moisture (higher or lower GPP), higher soil temperature and a longer unfrozen period (higher GPP), increases in physical disturbance to soils (lower GPP), and/or later snowmelt (lower GPP) (Collins et al., 2021; Euskirchen et al., 2017;

Hewitt et al., 2018; M. T. Jorgenson & Osterkamp, 2005; Kelsey et al., 2021; Mauritz et al., 2017; Rodenhizer et al., 2020). At the same time, R_{eco} can also be suppressed or promoted by abrupt thaw through many of the same environmental changes: nutrient availability (higher R_{eco}), shifts in soil moisture (higher or lower R_{eco}), deeper snow depth and higher soil temperature (higher R_{eco}), and physical disturbance (lower R_{eco}) (Abbott & Jones, 2015; Emmerton et al., 2016; Mauritz et al., 2017; Rodenhizer et al., in review). However, plant and microbial communities may respond to environmental changes at different rates or to different degrees, as, for example, microbes can continue to respire throughout the winter if soils do not freeze, or physical disturbance may kill plants entirely, suppressing GPP more than R_{eco} (Cassidy et al., 2016; Vogel et al., 2009). Overall, annual estimates of NEE in a few field studies have shown lower NEE (less uptake or higher emissions) in thermokarst affected areas (Cassidy et al., 2016; Euskirchen et al., 2017; Rodenhizer et al., in review). However, the wide variety of mechanisms driving the response of CO_2 fluxes to abrupt thaw indicates that this response is likely to be variable across the landscape. Therefore, it is necessary to better understand these mechanisms, in order to better constrain the net impact of abrupt thaw on the carbon cycle across space and into the future (Lara et al., 2020).

1.2. Divergent Hydrologic Responses to Permafrost Thaw

One of the main factors driving the relationship between abrupt thaw and carbon cycling is the complicated response of hydrologic conditions to abrupt thaw. In permafrost ecosystems, the water table is perched on top of the permafrost, which is relatively impermeable, such that lateral flow only occurs in the active layer (Walvoord & Kurylyk, 2016). As the active layer deepens in upland permafrost sites, the water table should follow the receding permafrost, resulting in drier surface soil conditions. However, thermokarst depressions can form where high

ice content causes subsidence, which results in the ground surface dropping closer to the water table. Therefore, areas with limited subsidence may get drier as the water table drops, while areas with high rates of subsidence will form thermokarst depressions and get wetter as water pools in these areas (Evans et al., 2020; M. T. Jorgenson et al., 2001; M. T. Jorgenson & Osterkamp, 2005; Vogel et al., 2009). With continued thaw, thermokarst depressions begin to expand and merge, increasing hydraulic connectivity as the permafrost table deepens across broader areas (Connon et al., 2018). In this more advanced stage of abrupt thaw, higher hydraulic connectivity allows better drainage and can lead to uniformly drier conditions than prior to thaw. However, due to spatial and temporal variability in the rate of subsidence across permafrost landscapes, there is likely to be a wide range of divergent hydrologic conditions found within permafrost ecosystems as a consequence of abrupt thaw.

Hydrologic conditions affect moisture availability, oxygen conditions, nutrient and carbon availability, and soil temperatures (Kokelj & Jorgenson, 2013), all of which directly impact the plant and microbial communities responsible for driving carbon fluxes. Relatively dry conditions (excluding drought) result in high rates of R_{eco} and GPP, as oxygen is abundant within the active layer, while water-logged conditions can suppress R_{eco} and GPP due to anoxic conditions within the active layer (Kotani et al., 2019; Mauritz et al., 2017; Natali et al., 2015; Schädel et al., 2016). On the other hand, higher ground heat fluxes due to inundation can cause soils to warm, deepening the active layer, increasing the stock of thawed carbon and nutrients available to microbes, and lengthening the time that the active layer remains unfrozen or even causing the formation of taliks (pockets of soil which remain unfrozen year-round) (Subin et al., 2013). This could potentially offset suppressed CO_2 production due to low-oxygen conditions.

How these complex and sometimes conflicting influences on CO_2 fluxes will resolve across heterogeneous landscapes undergoing abrupt thaw remains an area of high uncertainty.

In this study, we investigated the impact of abrupt thaw on soil hydrologic conditions and the impact of deeper permafrost thaw and shifts in soil hydrologic conditions on growing season (GS) and annual CO_2 fluxes in a 13 year permafrost warming experiment in an upland tundra ecosystem. Due to the length of this experiment, we were able to observe the initial response of CO_2 fluxes to warmer soil and air temperatures as well as the response to abrupt thaw, which only developed after several years of experimental manipulation and resulted in a patchwork of moisture and thaw responses. We hypothesized that deeper permafrost thaw would promote GS GPP and R_{eco} in drier locations, while wet conditions would suppress GPP and R_{eco}, resulting in higher GS NEE (more uptake) in drier locations and lower GS NEE (less uptake or release) in wet locations. We also hypothesized that annual NEE would be lower (higher release) in areas undergoing abrupt thaw, particularly in wet locations, as the period during which soil temperatures are above 0°C should be longer and allow higher respiration during the shoulder season and throughout the winter.

2. Methods

2.1. Site and Experimental Design

The Carbon in Permafrost Experimental Heating Research (CiPEHR) is located in moist acidic tussock tundra at ~700 m in the foothills of the Alaska Range near Healy, AK. The site is underlain by permafrost due to cool temperatures at this elevation. Soils are classified as Gelisols with an organic layer ~0.45-0.65 m thick (Schuur et al., 2009). Mean annual temperature during the study was -1.71°C (2009-2021), with a GS average of 9.70°C (May-Sept.) and a non-growing season (NGS) average of -9.89°C (Oct.-Apr.)(Figure S1; Table S1). Mean annual

temperatures ranged from -4.08°C in 2013 (z = -1.50) to 1.04°C in 2019 (z = 1.74). Average annual rainfall was 278 mm, with all rainfall occurring during the GS in seven of the thirteen years. In the remaining years, less than 10% of rainfall occurred during the NGS in all but one year in which 21% of annual rainfall occurred during the NGS.

CiPEHR was established in 2008 to warm soil and air temperatures passively to simulate future warming caused by climate change (Natali et al., 2011). Soil warming was achieved with snow fences, which increase snow depth and insulate the ground from extremely cold winter air temperatures. Excess snow in the warming treatments was shoveled off each spring to ensure similar water inputs and date of snowmelt in control and soil warming treatments. The experiment consisted of three replicate blocks with two snow fences each. Each snow fence consisted of eight plots, four on the control side of the fence, and four on the soil warming side of the fence. Air warming was achieved within half of the plots on each side of each snow fence using 0.36 m^2 x 0.5 m tall clear open-top chambers (OTCs) which were deployed during the snow free period of each year. Additional details on the experimental design can be found in Natali et al. (2011).

This experiment was initially designed with four discrete treatments: control, air warming, soil warming, and air + soil warming. Over the course of the experiment however, differential ground subsidence related to the heterogenous ground ice distribution and experimental warming resulted in a wide variety of environmental responses of permafrost thaw and surface soil moisture (Rodenhizer et al., 2020). These factors did not always respond uniformly within treatments, but rather a gradient of responses was observed both across and within treatments. To capture the gradient of environmental responses to warming and explain

the variability in CO_2 flux responses, we used environmental variables as continuous explanatory variables throughout most analyses rather than considering treatments as categorical effects.

2.2. Environmental Monitoring

Meteorological variables were monitored continuously using a HOBO Onset station (Bourne, MA, USA) and summarized to half-hourly time steps. Air temperature was measured year-round at 2 m, photosynthetically active radiation (PAR) was measured year-round, and rainfall was measured during the GS. Missing data were gap-filled using an eddy covariance tower and meteorological tower at a natural permafrost thaw gradient located about 1 km distant (Schuur et al., 2021) or nearby NOAA climate stations when necessary. Cumulative end-of-season snow depth was measured along transects located at each fence (control and soil warming) in April immediately prior to snow shoveling. Chamber air temperatures were measured during CO_2 flux measurements at 15 cm height within each OTC using shaded thermistors and were gap-filled using plot-level linear models comparing OTC air temperatures to HOBO air temperatures.

Metrics of permafrost thaw were monitored with measurements of soil temperature, thaw depth, and subsidence. Soil temperature was measured at 5 and 10 cm depths in all plots and at 20 and 40 cm depths in half of the plots of each treatment using type T copper-constantan thermocouples. Thaw depth was measured once or twice weekly throughout the snow-free season using a metal probe inserted into the soil until it hit the frozen layer. Elevation was measured at point locations in a 2x2 m grid across each of the experimental blocks using a Trimble high-precision differential GPS in late July or early August of 2009, 2011, and 2015-2020 (Rodenhizer et al., 2020). Elevation values were interpolated using ordinary kriging to create a continuous elevation surface for each year and subsidence was calculated as the

difference in elevation relative to 2009 (Hiemstra et al., 2009). Plot-level subsidence was gap-filled in years without measurements using linear interpolation.

Hydrologic conditions were monitored with measurements of soil moisture at two depths and water table depth. These measurements reflect differences in water inputs and hydraulic connectivity, although they do not directly measure lateral movement of water within the soil profile. Soil gravimetric water content (GWC) was estimated in the top 5 cm of the moss/soil layer in each plot using site-calibrated DC half-bridge resistance measurements (Vogel et al., 2009). The sensors for GWC at this site do not produce exact values of soil moisture, but the relative values between measurements can be compared. Soil volumetric water content (VWC) was measured in the top 15 cm in half of the plots of each treatment using Campbell Scientific CS616 water content reflectometer probes calibrated to the site. Water table depth (WTD) relative to the moss/soil surface was measured manually three times weekly throughout the snow-free season (May 1- Sept 30 except when frozen) in wells that were installed at each fence throughout the experiment (minimum 2 wells in soil warming and 2 wells in control at each fence).

Aboveground plant biomass (AGB) was estimated at the plot level using a non-destructive point-intercept method during peak GS (July) in 2009-2013, 2017, and 2021 (Salmon et al., 2016; Schuur et al., 2007). Point-intercept counts were completed for each species of vascular plant and for all mosses combined. Vascular biomass was dominated by the tussock forming sedge *Eriophorum vaginatum*, and other common plant species included *Vaccinium uliginosum*, *Betula nana*, *Carex bigelowii*, *Rubus chamaemorus*, *Empetrum nigrum*, *Rhododendron subarcticum*, *Vaccinium vitis-idaea*, *Andromeda polifolia*, and *Oxycoccus microcarpus*. We did not distinguish between moss species for this study, but the dominant

species at the site included *Sphagnum fuscum*, *Pleurozium schreberi*, and *Dicranum* spp. (Deane-Coe et al., 2015).

2.3. Carbon Flux Measurements and Processing

An automated system was used to measure GS NEE and R_{eco} in each experimental block (Mauritz et al., 2017; Natali et al., 2011). Each automated system consisted of eight flux chambers, which were rotated between plots every couple of days. To measure fluxes, air was circulated between the chamber and an infrared gas analyzer (LI-820, LICOR corp., Lincoln, NE, USA) for 1.5 minutes and CO_2 concentration was measured every 2 seconds. Measurements were logged on a Campbell Scientific CR1000 data logger. Because only one chamber could be measured at a time, the automated system cycled through all chambers every 1.6 hours. In 2019, a smaller subset of plots (n = 12) were measured in order to reduce field work effort. To maximize the range of environmental conditions and fluxes represented by the subset of plots that were measured in 2019, we selected plots across the entire range of mean annual WTD and ALT. This resulted in a bias in the treatment-level flux estimates in 2019 as compared to years where we measured all plots. We reduced this bias by gap-filling missing plot-level fluxes to determine annual averages for 2019 using relationships with environmental conditions (see 3.6.2).

All processing of carbon flux data was performed in R (R Core Team, 2021) using the data.table (Dowle & Srinivasan, 2021) and tidyverse packages (Wickham et al., 2019). Flux modeling for gap-filling and flux partitioning was completed using the minpack.lm package (Elzhov et al., 2016). CO_2 flux was calculated as the slope of CO_2 concentration throughout the measurement period (ppm CO_2 sec^{-1}) and converted to NEE (μmol m^{-2} $s\text{-}^{2}$) using the chamber volume and air pressure. Raw flux measurements were filtered to remove erroneous

measurements. All measurements with unrealistic CO_2 concentrations (<300 ppm or >550 ppm), low chamber air flow rate (<500 mL min^{-1}), or during periods of high wind speeds (>7 m s^{-1}) were removed. Additionally, all flow rates, CO_2 concentrations, and CO_2 fluxes were visually inspected in ~10 day periods to remove outliers.

In order to estimate continuous half-hourly flux in each plot, we gap-filled NEE using a light response curve with photosynthetically active radiation (PAR),

$$\text{Eq. 1. } NEE = \frac{a \times PAR \times GPmax}{(a \times PAR) + GPmax} + R$$

where a is photosynthetic efficiency, or the photosynthetic rate at half of GPmax, GPmax is the maximum potential photosynthetic rate, and R is the basal rate of respiration. In order to allow for differences between plots (caused by treatment or natural variability) and throughout the GS, NEE was modeled monthly in each plot throughout the GS (May-Sept.). Only measurements taken during the day were included in this modeling step. For the purposes of modeling, day was defined as PAR >= 5 μmol m^{-2} s^{-2} and night as PAR < 5 μmol m^{-2} s^{-2}. The resulting parameters were used to gap-fill half-hour time steps without a flux measurement.

R_{eco} was modeled at the plot-level using a temperature sensitivity (Q10) model with soil temperature measured at a depth of 10 cm,

$$\text{Eq. 2. } R_{eco} = A^{B \times T_{soil}}$$

where A is the basal respiration rate and B is the Q10 temperature response. NEE measurements taken at night were assumed to be R_{eco} without any contribution from photosynthesis and were used for this modeling step. The resulting parameters were used to gap-fill nighttime respiration during half hour periods without flux measurements and to estimate daytime respiration.

GPP was estimated as

$$\text{Eq. 3. } GPP = NEE - R_{eco}$$

during the day (PAR>= 5) and was set to 0 during the nighttime. This method resulted in some negative values for GPP. Though not biologically meaningful, these negative values reflect uncertainty associated with the measurements and models and were left in the dataset in order to avoid bias in flux sums.

We estimated NGS (Oct.-Apr.) respiration at the plot-level using a soil temperature response curve determined at an eddy covariance tower at the site (Schuur et al., 2021). Half-hourly winter respiration measured at the eddy covariance tower was modeled using the ecosystem respiration Q10 model (Eq. 2.) with 5 cm soil temperature. These parameters were used to estimate half-hourly fluxes for each plot using plot-level 5 cm soil temperature measurements.

2.4. Data Merging and Derived Variables

Half-hourly flux data were joined with all other environmental variables for each individual plot. For the purposes of this analysis, we defined each year as a period beginning on Oct. 1st and ending on Sept. 30th so that the environmental conditions of the prior winter could be considered when modeling fluxes. For environmental variables measured less frequently than every half-hour (i.e., thaw depth), a rolling join was used such that the closest value (in time) was associated with each half-hourly flux, so long as there was no more than two weeks between the two measurements. Missing values with no measurement within two weeks were not gap-filled. Because WTD was measured in water wells which were not directly located in each plot, WTD values were assigned to individual plots by a combination of proximity and representative microtopography for each year. Half-hourly chamber temperatures were gap-filled using plot-

level linear regressions between site-level air temperature (HOBO) and temperatures measured within the chambers. Growing degree days (GDD) were calculated as the cumulative sum of temperatures above 0°C, and freezing degree days (FDD) were calculated as the cumulative sum of temperatures below 0°C on an annual basis. Thaw penetration was calculated as the sum of subsidence and ALT.

Merged half-hourly flux and environmental data were aggregated to monthly and annual values. ALT, subsidence, thaw penetration, and AGB were already single annual values, fluxes and precipitation were summed, and for all other environmental data, the mean and standard deviation were calculated. The standard deviation was included as a metric of intraseasonal variability within individual plots. Additionally, we calculated three time-lagged variables for the current and prior months to infer the effect of antecedent conditions on fluxes. These variables included mean GWC (GWC_{2M}), mean VWC (VWC_{2M}), and GDD (GDD_{2M}), which was calculated as the cumulative sum of temperatures above 0°C in the prior and current months only. Finally, meteorological data were summarized to seasonal (GS and NGS) and annual values for analysis of the variability of climatic conditions from year to year.

2.5. Thermokarst Classification

To determine the impact of abrupt thaw processes on environmental conditions and CO_2 fluxes, the landscape across CiPEHR was classified according to its abrupt thaw status in 2017-2019 and 2021 following the methods in Rodenhizer et al. (in review). The classification used 1 m resolution airborne LiDAR data available from the National Ecological Observatory Network to classify each cell as non-thermokarst (Non-TK), thermokarst margins (TK Margin), and thermokarst centers (TK Center), where margins were considered any cells within 1 m of a thermokarst depression outline. We determined the classification within each plot in each of the

four years with remote sensing data. To determine thermokarst classification in 2020 (when no remote sensing data were available), we gap-filled on a plot by plot basis using linear interpolation.

2.6. Flux Analysis

We used gradient boosted regression tree models (GBMs) to investigate environmental drivers of CO_2 fluxes, using the gbm package (Greenwell et al., 2020), as this machine learning method allows for non-linear relationships and tipping-point behavior. 2009 was not included in this analysis or any of the other flux analyses because CO_2 fluxes were depressed in 2009, likely due to disturbance from experimental set-up activities (Celis et al., 2017; Mauritz et al., 2017). We modeled GPP, NEE, and R_{eco} separately using cumulative monthly (n = 6912) and cumulative GS (n = 576) fluxes from each plot. The monthly models included a mix of explanatory variables intended to test the impact of diverging soil environmental conditions during abrupt thaw on CO_2 fluxes, in addition to variables which drive seasonal climate patterns. The variables included in the monthly models were the mean and standard deviation of GWC, VWC, WTD, and soil temperature (10 cm), as well as TD, annual subsidence, thaw penetration to date (TD + annual subsidence), monthly precipitation sum, monthly GDD, monthly FDD, annual AGB, mean air temperature, GWC_{2M}, VWC_{2M}, and GDD_{2M}. The explanatory variables included in the cumulative GS models were thaw penetration, subsidence, ALT, total precipitation, previous winter snow depth, previous winter minimum soil temperature (10 cm), AGB, and the mean and standard deviation of GWC, VWC, WTD, air temperature and soil temperature (10 cm). For all models, we randomly sampled 80% of the data rows for use in model training and reserved the remaining data to evaluate model performance. For each model, we determined the optimal number of trees, interaction depth, shrinkage, and minimum

observations per node from a range of values using the caret package (Kuhn, 2021). Model performance was evaluated using a linear regression of the predicted vs. measured values; slope of lines were determined by geometric mean regression, which splits the variance equally between both axes. Variable importance (VI) was used to evaluate the importance of each model predictor, and was calculated as the reduction in the sum of squared error attributable to each variable and normalized to sum to 100. Partial dependence plots were used to evaluate the effect of the top predictors on CO_2 fluxes, and shapley additive explanations were used to investigate differences in model behavior in the driest and wettest deeply thawed plots.

To evaluate the trajectory of CO_2 fluxes over the 13-year experiment according to the degree of abrupt thaw, we visualized the change in GS CO_2 fluxes in each thermokarst class. Because we did not have data on thermokarst class prior to 2017 (although we knew that all of the plots started out as non-thermokarst), we binned the plots by 2021 thermokarst class for this analysis. Additionally, we gap-filled monthly NEE, R_{eco}, and GPP in 36 plots which were not measured in 2019 using the monthly GBMs and observed environmental conditions. Generalized Additive Models were used to observe trends through time.

3. Results

3.1. Flux Response to 13 Years of Warming

GS CO_2 fluxes responded non-linearly to warming through time, with higher carbon uptake in early years beginning to reverse later in the experiment (Figure 1). Soil warming plots had the largest increase in NEE, GPP, and R_{eco} and air warming had the smallest increase, with an intermediate response in air + soil warming plots. This treatment effect peaked in or before 2013 for all treatments and fluxes and declined thereafter. Between 2014 and the end of the experiment, very few consistent patterns remained. However, GPP remained somewhat elevated

over control plots in the air + soil warming treatment, R_{eco} was typically reduced in the air warming treatment, and NEE in soil warming plots was consistently lower than in control plots during the second half of the experiment (lower GS carbon uptake).

3.2. Environmental Changes Associated with Experimental Warming

Throughout the experiment, there was a general trajectory of deepening thaw, which caused subsidence and increasingly wet conditions, particularly in soil warming plots (Figure 2; Figure S2; Table S2). However, there was considerable variability among plots in the rate of thaw and the plot-level trajectory of WTD. At the beginning of the experiment, all plots had an ALT of close to 50 cm. By 2021, however, ALT ranged between 75 cm and over 250 cm, with control plots falling in the range 75-180 cm and soil warming plots falling in the range 120-260 cm. In 2009, WTD was between 13 and 36 cm below the surface, and as the experiment progressed, WTD became shallower in most plots. However, a few plots remained very dry, with WTD around 30 cm below the surface. Additionally, a few plots became inundated. This indicates that abrupt thaw created wetter conditions on average at this site, but that this average response was composed of divergent responses across the landscape, with some locations becoming drier and others wetter. Additionally, dry locations tended to experience more variability in soil moisture conditions, while wet locations were consistently wet (Figure S2; Figure S3).

Deepening thaw and increasingly wet conditions corresponded to the formation of thermokarst depressions within the experiment, particularly in the soil and soil + air warming plots (Figure 3). When the experiment was established in 2008, none of the plots showed signs of subsidence. By 2017, about half of the plots (all of the soil and soil + air warming, plus one control plot) were located along a thermokarst margin or within a thermokarst center. By 2021,

over 75% of the plots were located along a thermokarst margin or within a thermokarst center, including over half of control and air warming plots.

Differences in environmental conditions between thermokarst classes indicated that our classification reflected real shifts in environmental conditions that occurred throughout the experiment (Figure 4). Initial conditions (2010 to reflect the first year of flux data that we analyzed) showed the shallowest ALT (60.5 ± 3.0 cm; mean ± SD). By the period 2017-2021, ALT had deepened by 17 cm in Non-TK (78.0 ± 13.5 cm), nearly doubled in TK margins (110.0 ± 31.0 cm), and more than doubled in TK centers (132.0 ± 33.0 cm). However, the spread in ALT between plots also increased as abrupt thaw progressed from the Non-TK (approx. 50-125 cm) to TK center classes (approx. 75-260 cm). Similarly, there was the least subsidence (relative to 2009) in Non-TK (10 ± 9 cm), moderate subsidence in TK margins (33 ± 20 cm), and the most subsidence in TK centers (58 ± 18.5 cm), with an increasing spread between plots through the classes. Metrics of soil moisture (GWC, VWC, ALT) showed increasing wetness as abrupt thaw progressed, but only a few plots showed higher GWC in the TK center class, while VWC and WTD showed a more steady and consistent increase. GWC (top 5 cm) was low (3.6-5.4%) in all but the TK centers, where it doubled and had a large spread among plots (9.8 ± 11.6%). VWC (top 15 cm) increased consistently from initial conditions (42 ± 3%) to TK centers (54 ± 12%). WTD remained below the soil surface in all plots that were classified as Non-TK or TK margins (20 ± 4 cm below the surface), but exceeded the soil surface (ponding) in many plots within TK centers (3 ± 9 cm below the surface). SD GWC, SD VWC, and SD WTD (reflecting intraseasonal variability within a single plot, rather than the standard deviation across annual plot values) responded in unique ways. SD GWC decreased as abrupt thaw progressed from initial conditions (0.9 ± 0.1%; intraseasonal within-plot SD ± across-plot SD) to TK margins (0.7 ±

0.1%) before increasing again in TK centers (0.8 ± 0.1%). SD VWC increased from initial conditions (0.6 ± 0.1%) to Non-TK (0.7 ± 0.1%), dropped in TK margins (0.6 ± 0.1%), and then increased again in TK centers (0.7 ± 0.1%). SD WTD increased from initial conditions (4 ± 1 cm) to Non-TK and TK margins (both 6 ± 3 cm) before decreasing again in TK centers (5 ± 2 cm). We also observed shifts in AGB as abrupt thaw progressed. AGB increased from initial conditions (450 ± 87 g m^{-2}) to Non-TK (514 ± 130 g m^{-2}), and then remained relatively steady through TK margins (531 ± 134 g m^{-2}) and TK centers (531 ± 197 g m^{-2}). However, the spread in AGB between plots increased dramatically in TK centers, with some plots losing all biomass, and others showing some of the highest AGB of the experiment. This loss of biomass was related to increasing soil moisture and inundation (Figure S4).

3.3. Environmental Drivers of CO_2 Fluxes

3.3.1. GBM

The GBM models showed good fit across all CO_2 fluxes, particularly at the monthly timescale, and highlighted the importance of soil moisture in controlling cumulative GS fluxes (Figure 5). At the monthly timescale, the validation regression r^2 values were 0.83, 0.74, and 0.78 for GPP, NEE, and R_{eco}, respectively, while at the cumulative GS timescale, the values were 0.53, 0.44, and 0.57, respectively. All of the models had a tendency to slightly overestimate low fluxes and underestimate high fluxes, particularly at the cumulative GS scale. At the monthly timescale, the top predictors of CO_2 fluxes were temperature (GPP: air temperature VI = 40; NEE: air temperature VI = 36; R_{eco}: soil temperature VI = 35) and AGB (GPP: VI = 12; NEE: VI = 10; R_{eco}: VI = 9). Higher temperatures and AGB drove higher fluxes in all cases (Figure S5). Metrics of soil moisture were mostly missing from the top predictors of cumulative monthly CO_2 fluxes; the only exceptions were that NEE dropped rapidly as VWC increased above about 60%

(VI = 4), and GPP increased with increasing SD VWC (VI = 6). At the cumulative GS timescale, the top predictor of all CO_2 fluxes was biomass (GPP: VI = 28; NEE: VI = 25; R_{eco}: VI = 16), and the remaining top predictors related to metrics of soil moisture (GPP: SD GWC VI = 9, SD VWC VI = 6; NEE: VWC VI = 11, SD WTD VI = 7, GWC VI = 7; R_{eco}: SD GWC VI = 8, subsidence VI = 7) and ALT (GPP: VI = 8; R_{eco}: VI = 12). Most CO_2 fluxes were suppressed by higher values of the metrics of soil moisture with the exception of the response of GPP to SD VWC, which showed higher GPP when VWC was more variable, and the response of NEE to SD WTD, which showed higher NEE when WTD was more variable (Figure S6). Both GPP and R_{eco} increased with ALT up to about 125 cm at which point the relationship plateaued.

3.3.2. CO_2 Flux Response to Abrupt Thaw

Investigating GS cumulative CO_2 fluxes based on a progression of thermokarst classes revealed a non-linear flux response in areas undergoing abrupt thaw. Across all thermokarst classes, cumulative GS CO_2 fluxes increased in the first four years of the experiment, and increases were the weakest in Non-TK (by 2021) plots, somewhat stronger in TK margins, and the strongest in TK centers (Figure 6). After 2014, the trajectories of fluxes across thermokarst classes diverged. In Non-TK, both GPP and R_{eco} continued to increase through 2021, although the rate of increase declined slightly near the end of the experiment, particularly for GPP. GS NEE in Non-TK increased more or less linearly, but very slowly, throughout the entire experiment, reaching GS CO_2 uptake of almost 100 gC m^{-2} by 2021. In TK margins, a rapid increase in GPP peaked around 2016 before declining through 2021, likely due to increasing wetness. R_{eco} increased less rapidly than GPP at the beginning of the experiment, but did not decline as much through 2021. Overall, GS NEE in TK margins increased more strongly than Non-TK through about 2015, reaching a peak of about 100 gC m^{-2}, but then declined to about 75

gC m^{-2} by 2021, similar to the beginning of the experiment. In TK centers, GPP increased very rapidly until 2014 and then declined more slowly through 2021. R_{eco} increased more slowly than GPP, but for a longer period, reaching a peak in 2016, before declining slightly through 2021. Overall, GS NEE in TK centers increased rapidly between 2010 and 2013, peaking at about 125 gC m^{-2}, decreased nearly as rapidly through 2016, and then continued to decrease more slowly, falling to about 50 gC m^{-2} by 2021. The more rapid rate of thaw in plots which became thermokarst centers likely contributed to the initial, rapid NEE response, through the mobilization of carbon and nutrients in the active layer, as well as to the earlier and faster decline in NEE, through the rapid subsidence and increasingly wet conditions which reduced plant growth in many plots.

On average, NGS carbon emissions exceeded GS carbon uptake throughout the entire experiment (Figure S7; Table S3). Plot-level annual flux estimates showed carbon loss from nearly all plots across most years of the experiment, indicating that winter respiration more than offsets GS uptake, although there were some exceptions. Additionally, when accounting for winter respiration, R_{eco} had not yet peaked in plots classified as Non-TK by 2021 and showed slower post-peak declines in plots classified as TK margins or TK centers by 2021, indicating that the effect of warming on winter respiration could be longer lasting than impacts on GS fluxes.

4. Discussion

Abrupt thaw resulted in the creation of a patchwork of non-thermokarst areas with only slow subsidence, thermokarst margins resulting from a moderate rate of subsidence, and thermokarst centers resulting from rapid subsidence across the landscape (Figure 7). The environmental conditions of these three classes existed along a continuum from relatively

shallow thaw and generally dry, but highly variable, soil moisture conditions to deep thaw and consistently wet conditions. Our hypotheses about the effect of abrupt thaw and soil moisture conditions on CO_2 fluxes were generally supported. GS GPP and R_{eco} were highest in dry locations and lowest in the ponds that formed in thermokarst centers. In the dry conditions that were common early in the experiment and remained in a few plots throughout the entire experiment, GPP was promoted more than R_{eco}, leading to high GS carbon uptake. However, higher winter respiration in dry plots led to higher CO_2 release annually. As thermokarst depressions formed later in the experiment, wet conditions suppressed GPP more than R_{eco}, causing the wettest plots to release carbon throughout the GS. Although wet conditions suppressed the rate of R_{eco}, winter respiration was higher in thermokarst centers, indicating that the effects of warmer soil temperatures and a longer thawed period outweighed the effects of anaerobic conditions at the annual timescale. Taken together, these results support our hypothesis that there are multiple paths to CO_2 release from thermokarst affected landscapes (Schuur et al., 2021).

4.1. Non-Linear Carbon Flux Responses To Divergent Hydrologic Conditions

Early in the experiment, warming promoted fluxes, but as individual plots subsided at different rates, divergent soil moisture conditions complicated the response of CO_2 fluxes (Mauritz et al., 2017; Natali et al., 2011). Overall, GPP and R_{eco} tended to be suppressed in consistently wet sites, but GPP was suppressed more, leading to lower carbon uptake (lower NEE), or even net carbon release, during the GS. On the other hand, both GPP and R_{eco} were both higher along moderately subsided thermokarst margins where thaw was deep but soils were still dry enough to support plants, leading to higher carbon uptake during the GS (higher NEE). This provides more context to previous work at the site which found that thermokarst leads to

both higher GPP and R_{eco} at the landscape scale (Rodenhizer et al., in review). Water tracks are the most common thermokarst feature at this site, and these water tracks are often decades old and exhibit higher AGB, as succession has allowed thick moss growth within the depressions and larger shrub growth along the deeply thawed, but relatively dry margins. This is in contrast to drier sites, where drying along thermokarst margins can result in drought (Emmerton et al., 2016; Euskirchen et al., 2017). High AGB in older water tracks was responsible for driving a strong GS increase in both GPP and R_{eco} at the landscape scale (Rodenhizer et al., in review). Within CiPEHR, however, thermokarst depressions are less than a decade old and are undergoing rapid deformation, resulting in no succession to date. Rather, plants have begun to die-off in the most deeply subsided thermokarst centers which are inundated nearly year-round (Figure 4; Figure S4), with just a few tussocks of *Eriophorum vaginatum* still living in the deepest pond by 2021. This lack of plant AGB, combined with anoxic conditions, can explain the lower GPP and R_{eco} observed in thermokarst centers in this study (Mauritz et al., 2017; Schädel et al., 2016). Additionally, higher cumulative winter R_{eco} in thermokarst margins and centers in this study is corroborated by landscape level estimates from Rodenhizer et al. (in review). Taken together, this indicates that increased AGB and drier conditions along thermokarst margins may dominate the GS flux response to abrupt thaw at the landscape scale, but this is not sufficient to offset increases in ecosystem respiration during the winter (Supplemental Table 3).

Our results, combined with the results of other studies, point towards the potential for expansion of abrupt thaw to shift permafrost ecosystems towards becoming carbon sources at the annual scale (Cassidy et al., 2016; Hicks Pries et al., 2013; Rodenhizer et al., in review; Schuur et al., 2021; Turetsky et al., 2020). NGS respiration more than completely offset GS CO_2 uptake in most plots. Although we did not account for shoulder season photosynthesis in our modeling

approach, this is unlikely to change the sign of the annual carbon balance, as April and October GPP combined tended to be less than 15 g C m^{-2} at the site (Schuur et al., 2021; Webb et al., 2016), an order of magnitude less than annual CO_2 emissions. Our results are in line with several other studies from this site that used a variety of methods to assess NGS respiration and found that winter respiration is responsible for shifting the ecosystem from a GS CO_2 sink to an annual CO_2 source (Celis et al., 2017; Natali et al., 2011; Schuur et al., 2021; Webb et al., 2016). This highlights the importance of winter respiration in determining the sign of annual fluxes across the circumpolar region (Natali et al., 2019).

4.2. Environmental Drivers of fluxes

4.2.1. Role of soil moisture in driving CO_2 fluxes

Metrics of soil moisture across different depths in the soil profile were important predictors of CO_2 fluxes at the seasonal timescale, and exhibited strongly non-linear influences on fluxes. VWC was the most important soil moisture variable in determining annual NEE and it exerted a strongly non-linear effect. A slight increase in cumulative GS NEE as VWC rose from 30% to 60% could indicate a slight alleviation of drought allowing higher carbon uptake (Euskirchen et al., 2017), while the drop in NEE after ~60% VWC is likely due to waterlogging and plant mortality in subsided and wet plots. These results are similar to those by Heiskanen et al. (2021), who found higher R_{eco} and GPP with drier conditions in a subarctic fen, confirming the potential for lower soil moisture to drive higher fluxes at wet sites. Variability in metrics of soil moisture showed differing influences on CO_2 fluxes, likely due to the different depths that each metric corresponds to. Increasing SD GWC resulted in lower GPP and NEE at the cumulative GS timescale, and it appears that this reflected low AGB in the wettest plots, where there was high variability in GWC (Figure S2). This was the opposite pattern observed slightly

deeper in the soil profile with SD VWC and SD WTD, where lower variability in VWC and WTD resulted in decreased fluxes, as there was low variability in VWC and WTD in the wettest plots (Figure S2). We think this could be due to thermokarst centers having consistently inundated conditions within the top 15 cm where VWC is measured (Figure S3), leading to low variability in VWC and WTD, while the top 5 cm may occasionally dry out, leading to high variability in GWC.

4.2.2. The Trade-Off Between ALT and Inundation

There was a trade-off between ALT and metrics of soil moisture in determining CO_2 fluxes, particularly R_{eco}. ALT was associated with higher GPP and R_{eco}, likely reflecting the increased nutrient and carbon availability as permafrost thaws, in addition to higher soil temperatures and a longer thawed period (Mauritz et al., 2017). Subsidence (which results in wetter soils) and SD GWC, on the other hand, were associated with lower GPP and R_{eco}, likely reflecting increasingly anoxic conditions in inundated depressions (Mauritz et al., 2017; Taylor et al., 2021). The opposite, and relatively strong, effects on R_{eco} indicated that there was a trade-off between deep thaw providing access to nutrients and a long thawed period on the one hand and inundated, anoxic conditions on the other. In the few inundated plots, shapley values indicated that R_{eco} decreased more as a result of subsidence and inundation than it increased as a result of deeper ALT, leading to suppressed respiration (Figure S8). However, GPP was reduced nearly to zero in these plots, resulting in higher CO_2 release overall, despite lower rates of respiration. In a few plots with very deep ALT and WTD well below the surface, the impact of ALT was stronger than the impact of subsidence, leading to high rates of respiration (Figure S8). However, GPP was also very high in these plots, leading to high GS CO_2 uptake. Overall, the two extreme cases we observed were 1) complete inundation which led to suppressed GPP despite deep ALT, and 2)

deep thaw with dry conditions which led to higher GPP. R_{eco} and NEE were similarly suppressed in these extreme cases but to a lesser degree, indicating that GPP may be more strongly impacted by changes in moisture availability than R_{eco}.

4.3. Implications of Abrupt Thaw for the Future of Carbon Fluxes

GPP, R_{eco}, and NEE all showed strongly non-linear responses to experimental warming, likely driven by strong shifts in hydrology which did not become apparent until thermokarst depressions began to form. This did not occur until at least four years into the experiment, and, in some plots, was not apparent until the last few years of this 13 year experiment (Figure 1). This indicates that short-term studies may miss important feedbacks that take time to develop. In fact, we suspect that continuing to monitor this site into the future could result in another inflection point in fluxes, as continued thaw will likely cause thermokarst features to expand and merge, resulting in higher hydraulic connectivity and drier soil conditions more suitable to plant growth and heterotrophic respiration (Figure 7;Connon et al., 2018; Nitze et al., 2020).

The eventual development of drier conditions would reflect what most Earth system models (ESMs) predict in permafrost ecosystems, however these models oversimplify the processes involved in permafrost thaw and often miss the potential for divergent hydrologic conditions to develop during early stages of abrupt thaw. Many models predict that drying will occur progressively (Andresen et al., 2020; Lawrence et al., 2015; Schädel et al., 2018), while field studies, including ours, indicate that the trajectory of hydrology, and therefore fluxes, is not direct (Hinkel & Hurd, 2006; T. M. Jorgenson et al., 2013). This is because differential subsidence can lead to a patchwork of wet and dry conditions in the short-term. Most ESMs, however, do not represent subsidence, missing the potential for short-term wetting, and instead predicting that WTD will gradually drop as ALT deepens (Andresen et al., 2020). The amount of

time it takes to transition from a pre-thaw landscape to an advanced-thaw landscape is therefore likely to have a large impact on cumulative fluxes, making it important to understand how long this transition period could take (Lawrence et al., 2015). While modeling has predicted that the transition from wet to dry conditions during permafrost thaw could take only a few months (Teufel & Sushama, 2019), this study indicates the opposite. Over a 13-year period within this upland landscape, we observed a wide variety of hydrologic responses but overall wetter conditions, and it is uncertain how much longer it may take before thermokarst features merge and drain. Regardless of the hydrologic path, however, our results indicate that the long-term impact of abrupt permafrost thaw will be to shift tundra ecosystems towards higher annual carbon emissions, mobilizing centuries of accumulated permafrost soil carbon and accelerating increases in global temperature.

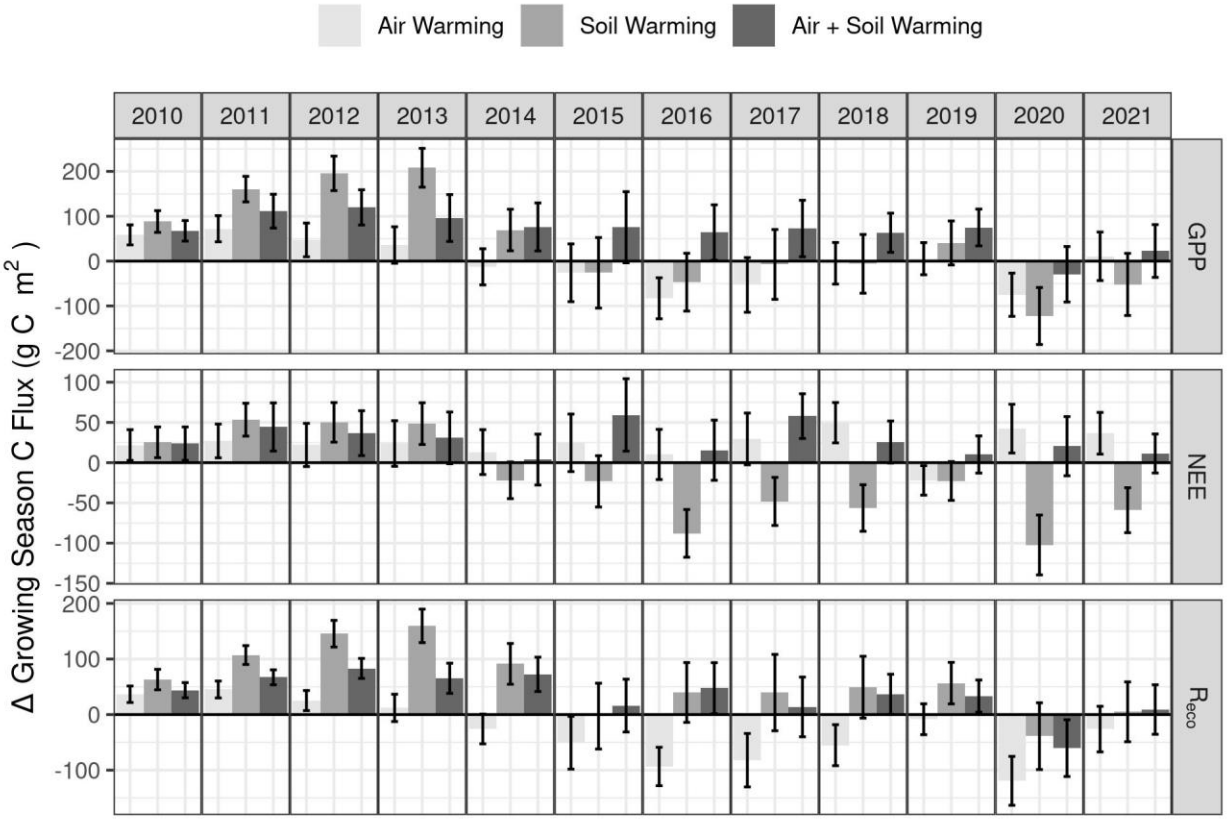

Figure 4.1. Experimental warming effects on GS NEE, R_{eco}, and GPP throughout the course of the experiment. Bar height indicates the difference in cumulative GS flux between each treatment and the control. Strong treatment effects of warming in the first several years declined or reversed later in the experiment.

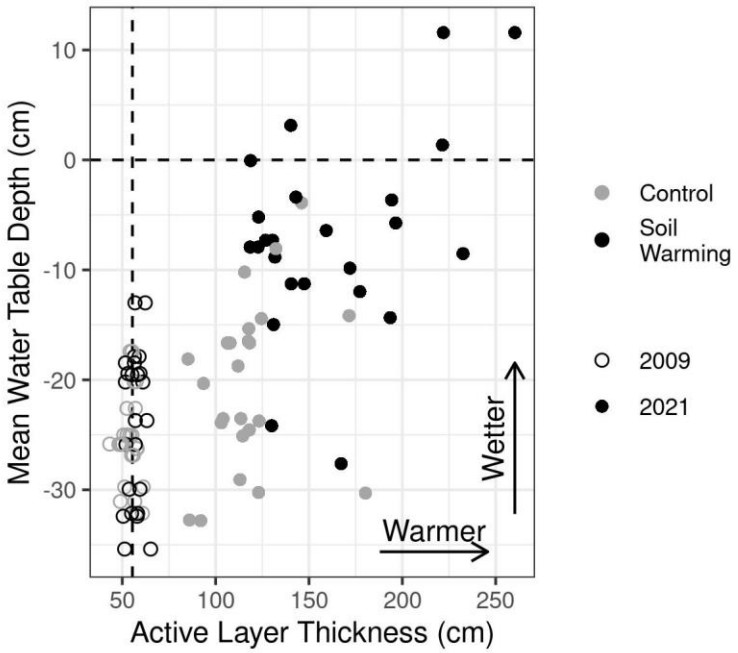

Figure 4.2. Initial (2009; open circles) and final (2021; filled circles) ALT and mean annual WTD in the warming experiment. Each point represents one plot, with gray representing control and black representing soil warming. The dashed lines represent a WTD of 0, or WTD at the soil surface, and the mean ALT in 2009.

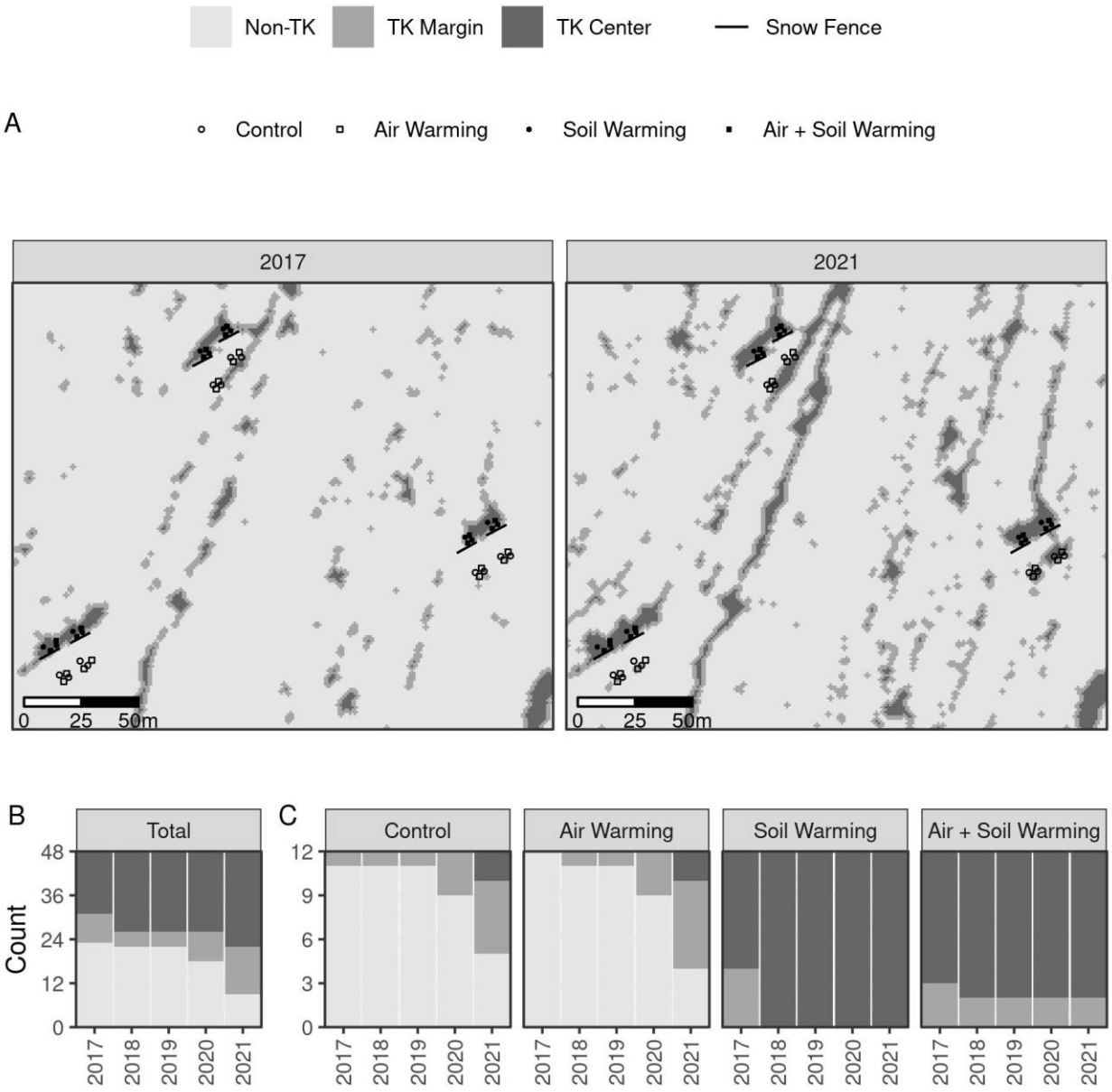

Figure 4.3. A) Thermokarst classification at CiPEHR in 2017 and 2021. Non-thermokarst is shown in light gray, thermokarst margins are shown in medium gray, and thermokarst centers are shown in dark gray. B) Count of CiPEHR plots in each thermokarst class between 2017 and 2021. C) Count of CiPEHR plots, broken up by warming treatment, in each thermokarst class between 2017 and 2021.

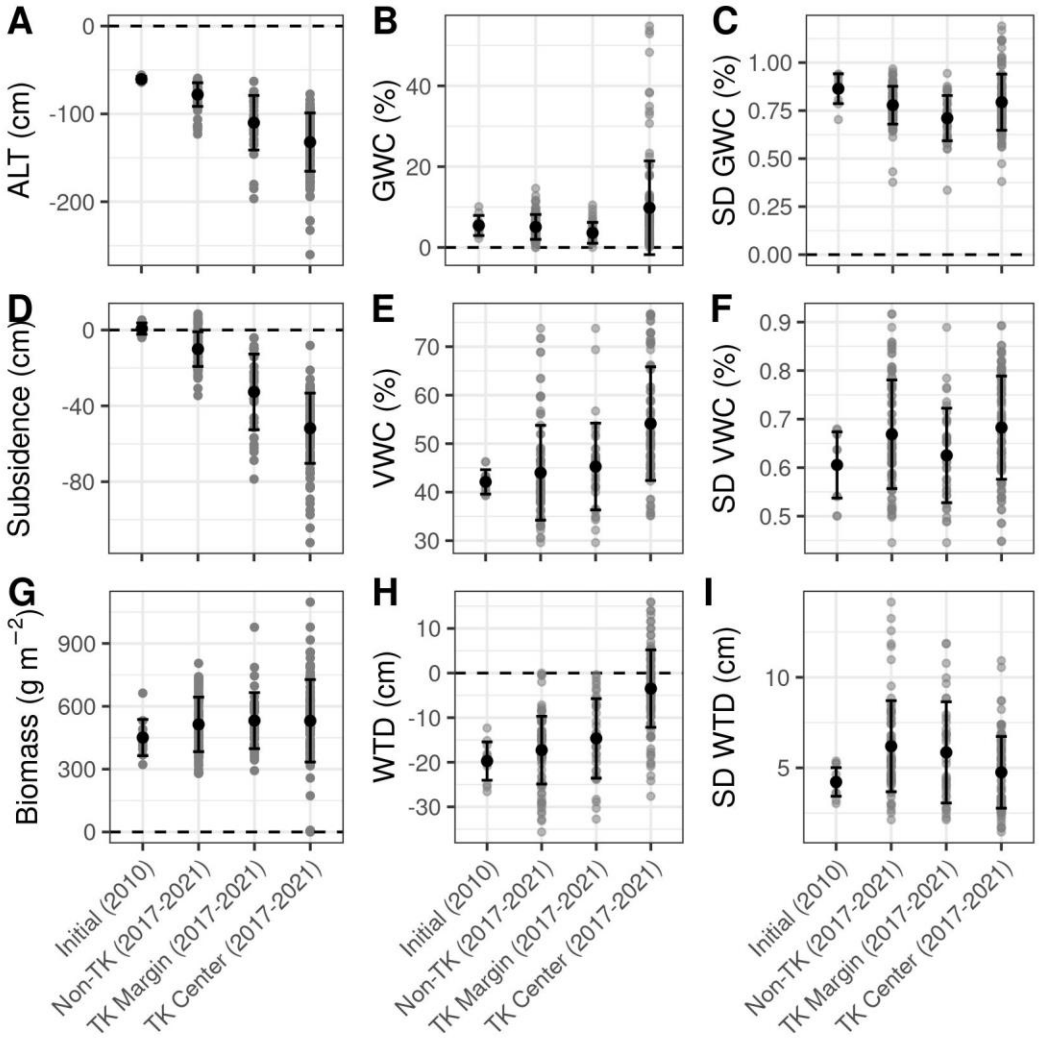

Figure 4.4. Differences in environmental conditions between initial conditions, non-thermokarst, thermokarst margins, and thermokarst centers: A) ALT, B) GWC, C) SD GWC, D) subsidence, E) VWC, F) SD VWC, G) AGB, H) WTD, and I) SD WTD. 2010 was used for initial conditions, as this was the first year in which CO_2 fluxes were analyzed, due to disturbance from experimental set-up in 2009. Thermokarst classifications were available in 2017-2021.

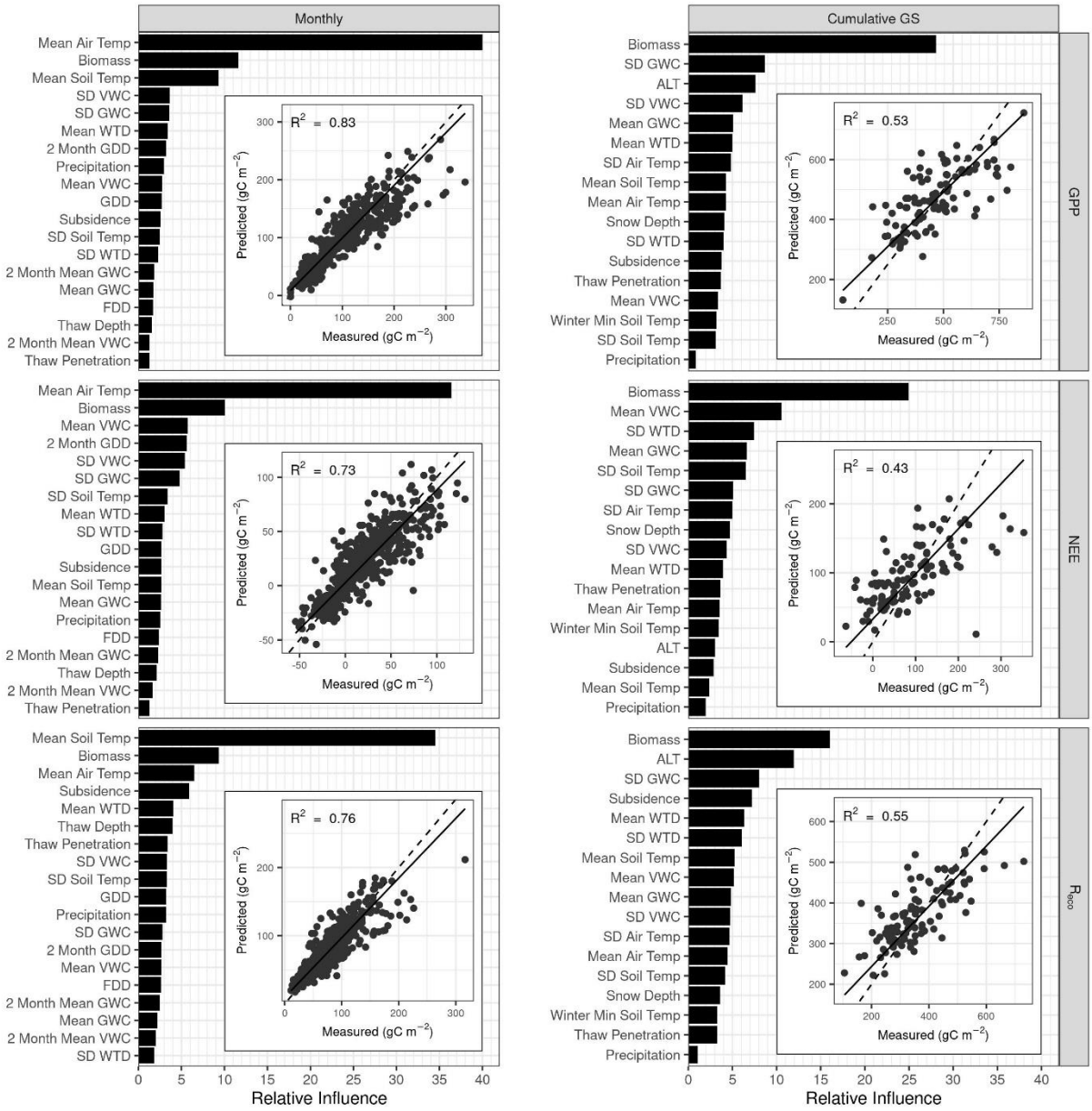

Figure 4.5. The relative influence (reduction in sum of squared error attributable to each variable) of environmental variables included in the monthly and cumulative GS GBM models of GPP, NEE, and R_{eco}, with linear regressions using validation data in the insets to evaluate model fit. Validation regression slopes were calculated using geometric mean regression. In addition to air/soil temperature and AGB, both metrics of soil moisture and metrics of thaw were strong predictors of fluxes.

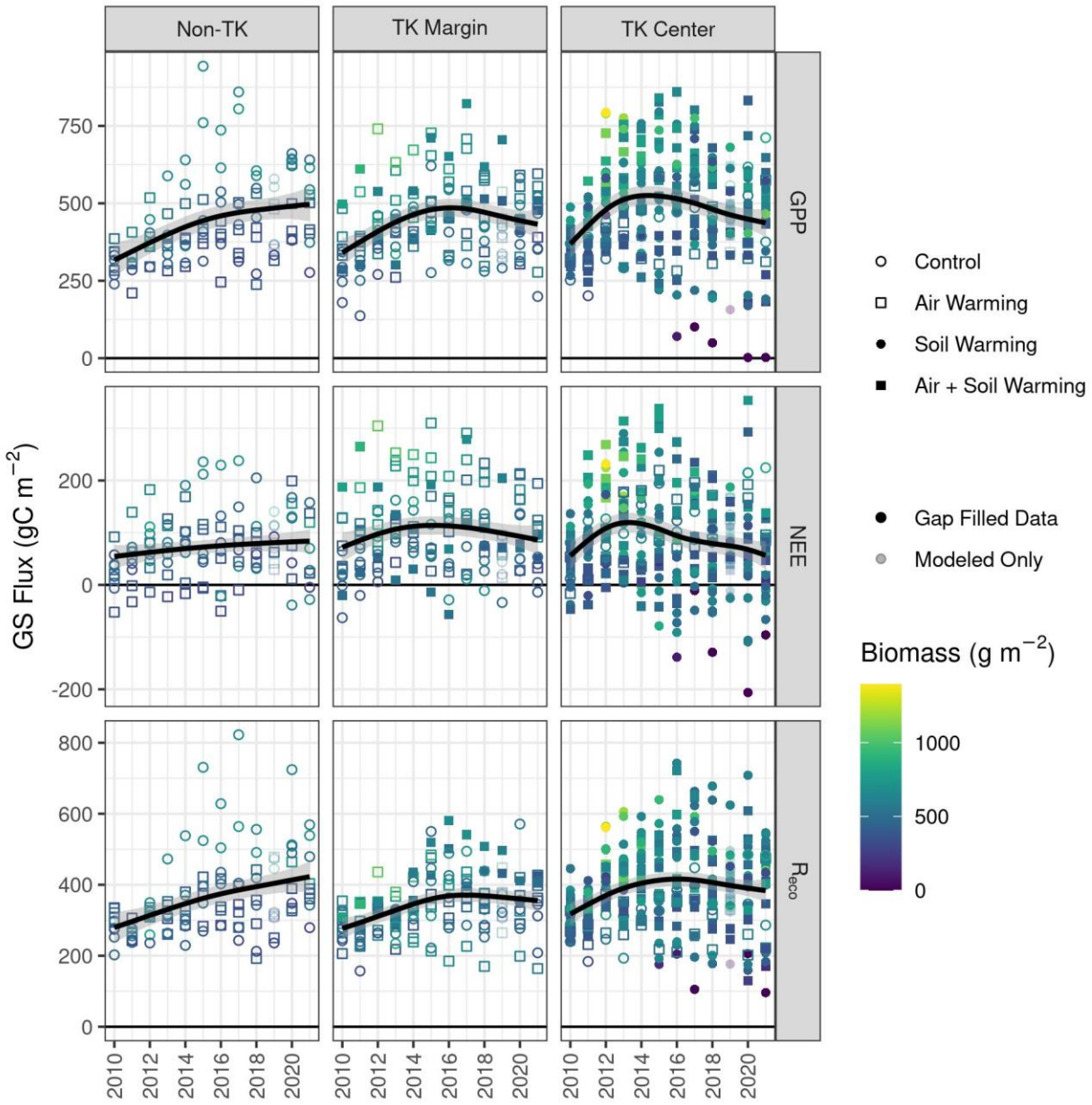

Figure 4.6. The trajectory of GS CO_2 fluxes throughout the course of the warming experiment in each of the thermokarst classes with generalized additive model (GAM) lines to highlight trends through time. Each plot was assigned to the same thermokarst class in all years based on the thermokarst class in 2021. Each point represents the GS cumulative CO_2 flux for an individual plot. Color indicates plot-level AGB and shape indicates experimental treatment. Solid points indicate GS sums of gap-filled measurements, and transparent points in 2019 indicate GS sums which were modeled using the monthly GBMs of each CO_2 flux and plot-level environmental conditions.

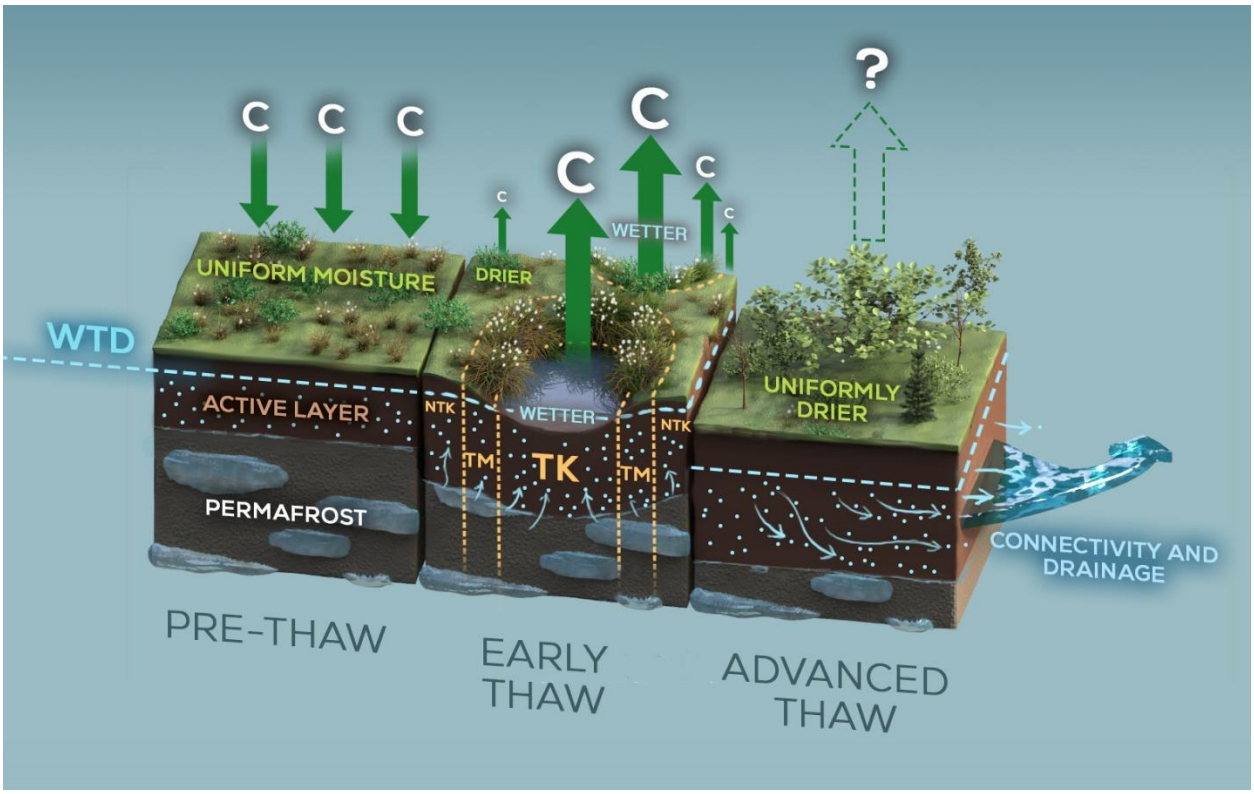

Figure 4.7. A diagram of hydrologic conditions and CO_2 fluxes as abrupt permafrost thaw progresses. NTK refers to Non-Thermokarst, TM refers to Thermokarst Margin, and TK refers to Thermokarst Center. Initially, the permafrost table is a relatively consistent depth below the soil surface and so is water table depth (WTD). The ecosystem is a slight carbon sink on an annual basis. During early-thaw, depressions form in the permafrost table and soil surface, causing water in the soil profile to drain from non-thermokarst areas and into the thermokarst centers. This leads to a patchwork of subsided, wet microsites, and relatively unsubsided, dry microsites. All areas of the landscape are annual carbon sources, with the lowest source occurring in non-thermokarst areas where R_{eco} increased more than GPP, and the highest source occurring in thermokarst centers, where GPP was suppressed more than R_{eco}. During advanced-thaw, discrete thermokarst depressions expand and merge with nearby thermokarst features, leading to deeper permafrost table depths across the landscape and drier conditions, as the WTD tracks the permafrost table. Permafrost ecosystems in advanced stages of thaw are likely to be carbon sources, although the magnitude is uncertain.

CHAPTER 5: DISCUSSION OF RESULTS AND CONCLUSIONS

Air temperatures in the Arctic are rising more than two times faster than the global average (IPCC, 2021), and this is causing permafrost to thaw both gradually, with incremental increases in ALT, and abruptly, with rapid collapse of ice-rich permafrost ground forming discrete thermokarst features (Turetsky et al., 2020). Although only ~20% of the permafrost region is expected to be susceptible to abrupt thaw, this region contains ~50% of permafrost carbon (Olefeldt et al., 2016). When permafrost carbon that has been frozen for years to thousands of years thaws, it becomes susceptible to microbial respiration and release to the atmosphere as greenhouse gases (Schuur et al., 2018). The reintroduction of this old carbon to the modern day carbon cycle has the potential to cause further climate change in a vicious cycle that leads to more permafrost thaw (Schuur et al., 2009). Therefore, it is imperative that scientists work to understand the magnitude, rate, and form of permafrost carbon release. This depends, in part, on how much of the permafrost region will undergo abrupt thaw and how susceptible abruptly thawed permafrost carbon is to respiration, as hydrology can shift rapidly with abrupt thaw and lead to conditions more or less suited to plant growth, ecosystem respiration, and methanogenesis (Kokelj & Jorgenson, 2013). This dissertation investigated the rate of ground subsidence and the impact it has on thawed permafrost carbon stocks, the extent and morphology of abrupt thaw in a warming tundra ecosystem and the role it plays in CO_2 and CH_4 release to the atmosphere at the landscape scale, and the fine scale responses of hydrology to abrupt thaw and how this determines the spatial heterogeneity of CO_2 fluxes.

At CiPEHR, a permafrost warming experiment to simulate future conditions, subsidence of up to ~1 m per decade was observed (Rodenhizer et al., 2020). This subsidence was responsible for masking the full rate of permafrost thaw, as ALT measurements, which are the common method

for tracking gradual permafrost thaw, fail to account for the change in the soil surface elevation. Accounting for subsidence revealed that the depth to the permafrost table increased up to 50% more relative to 2009 than ALT measurements indicated. This also meant that permafrost carbon thawed twice as quickly over the course of the experiment than would have been calculated with ALT. This resulted in a larger pool of carbon available to microbial respiration than would have been assumed if only gradual thaw were considered. This highlights a large discrepancy between how permafrost ecosystems are modeled in Earth System Models and how they thaw in the real world, resulting in the potential for models to vastly underestimate permafrost thaw and carbon emissions (Turetsky et al., 2020).

Abrupt thaw was not just present in a permafrost warming experiment designed to simulate future conditions, though; thermokarst features covered 7% of the landscape surrounding the permafrost warming experiment, as well. These thermokarst features took the form of numerous small thermokarst pits and ponds and larger networks of water tracks. Although there were more small pits by number, the water tracks affected a far larger area, making them the form of thermokarst likely to be responsible for the largest impact on permafrost carbon thaw and, therefore, carbon fluxes. Both annual CO_2 and CH_4 release increased in response to abrupt thaw. However, the high biomass observed in water tracks actually caused higher CO_2 uptake during the growing season. Despite this, the increase in non-growing season CO_2 emissions outpaced growing season increases in uptake, highlighting the importance of non-growing season fluxes, despite their smaller magnitude, particularly in areas of abrupt thaw (Natali et al., 2019). This is likely due to the increased length of the zero curtain and the higher likelihood of talik formation in thermokarst features than in areas experiencing only gradual thaw, which allows microbial activity to continue longer into, or throughout, the non-growing season (Parazoo et al., 2018).

There was considerable fine-scale spatial variability in abrupt thaw and the resulting hydrologic and carbon cycle responses that could not be addressed at the landscape scale. Abrupt thaw within CiPEHR resulted in two main hydrologic regimes: 1) subsided and wet and 2) high and dry. Thermokarst depressions were found to be consistently wet, almost regardless of precipitation conditions, as moisture from surrounding high and dry locations would drain into these depressions allowing them to remain saturated long into dry periods. On the other hand, the high and dry locations experienced more variable soil moisture conditions, with wet conditions following rain and dry conditions during dry spells. These divergent hydrologic conditions led to divergent growing season CO_2 responses. Growing season GPP and R_{eco} were suppressed in subsided and wet locations, as water-logging killed plants and slowed microbial activity. This resulted in an overall increase in growing season CO_2 emissions from subsided and wet locations. Growing season GPP and R_{eco} were stimulated in high and dry locations, where increased availability of carbon and nutrients in the deepening active layer was not offset by water-logging and anoxia. At this moist tundra site, the high and dry locations were not dry enough to cause drought, so the drier conditions resulted in the alleviation of flooding, as seen in wet ecosystems like fens (Heiskanen et al., 2021). Overall, there was an increase in growing season CO_2 uptake in high and dry locations. However, it is important to note that winter emissions likely offset growing season uptake, even in these highly productive locations, based on the available eddy covariance data (Rodenhizer et al., in review; Schuur et al., 2021), and may have resulted in larger CO_2 emissions at the annual scale than tundra undisturbed by abrupt thaw, although this is uncertain without annual fine-scale CO_2 flux measurements.

In conclusion, this dissertation highlights the important role that abrupt thaw and non-growing season microbial activity will play in exacerbating the effect of climate change on permafrost

carbon release into the future. Abrupt permafrost thaw could result in about the same magnitude of emissions as gradual permafrost emissions over the next century (Turetsky et al., 2020). Combined, these permafrost emissions are likely to be comparable to some of the world's largest carbon polluters (at current emission levels)(Schuur et al., in review), but these emissions were not included in the Paris Agreement commitments (Natali et al., 2021). It is therefore necessary that model projections be improved to better account for abrupt permafrost thaw and that these projections are included in global climate change policy.

REFERENCES

Abbott, B. W., & Jones, J. B. (2015). Permafrost collapse alters soil carbon stocks, respiration, CH_4, and N_2O in upland tundra. *Global Change Biology*, *21*(12), 4570–4587. https://doi.org/10.1111/gcb.13069

Abbott, B. W., Jones, J. B., Godsey, S. E., Larouche, J. R., & Bowden, W. B. (2015). Patterns and persistence of hydrologic carbon and nutrient export from collapsing upland permafrost. *Biogeosciences*, *12*(12), 3725–3740. https://doi.org/10.5194/bg-12-3725-2015

Abe, T., Iwahana, G., Efremov, P. V., Desyatkin, A. R., Kawamura, T., Fedorov, A., Zhegusov, Y., Yanagiya, K., & Tadono, T. (2020). Surface displacement revealed by L-band InSAR analysis in the Mayya area, Central Yakutia, underlain by continuous permafrost. *Earth, Planets and Space*, *72*(1), 138. https://doi.org/10.1186/s40623-020-01266-3

Andresen, C. G., Lawrence, D. M., Wilson, C. J., McGuire, A. D., Koven, C., Schaefer, K., Jafarov, E., Peng, S., Chen, X., Gouttevin, I., Burke, E., Chadburn, S., Ji, D., Chen, G., Hayes, D., & Zhang, W. (2020). Soil moisture and hydrology projections of the permafrost region – a model intercomparison. *The Cryosphere*, *14*(2), 445–459. https://doi.org/10.5194/tc-14-445-2020

Arndt, K. A., Oechel, W. C., Goodrich, J. P., Bailey, B. A., Kalhori, A., Hashemi, J., Sweeney, C., & Zona, D. (2019). Sensitivity of methane emissions to later soil freezing in Arctic tundra ecosystems. *Journal of Geophysical Research: Biogeosciences*, *124*(8), 2595–2609. https://doi.org/10.1029/2019JG005242

Ballinger, T. J., Overland, J. E., Wang, M., Bhatt, U. S., Brettschneider, B., Hanna, E., Hanssen-Bauer, I., Kim, S.-J., Thoman, R. L., & Walsh, J. E. (2021). Surface Air Temperature. In T. A. Moon, M. L. Druckenmiller, & R. L. Thoman (Eds.), *Arctic Report Card 2021*. https://doi.org/10.25923/53xd-9k68

Bao, T., Xu, X., Jia, G., Billesbach, D. P., & Sullivan, R. C. (2021). Much stronger tundra methane emissions during autumn freeze than spring thaw. *Global Change Biology*, *27*(2), 376–387. https://doi.org/10.1111/gcb.15421

Bartoń, K. (2020). *MuMIn: Multi-model inference* (1.43.17) [R]. https://CRAN.R-project.org/package=MuMIn

Bates, D., Mächler, M., Bolker, B., & Walker, S. (2015). Fitting Linear Mixed-Effects Models Using {lme4}. *Journal of Statistical Software*, *67*(1), 1–48. https://doi.org/10.18637/jss.v067.i01

Belshe, E. F., Schuur, E. A. G., & Bolker, B. M. (2013). Tundra ecosystems observed to be CO_2 sources due to differential amplification of the carbon cycle. *Ecology Letters*, *16*(10), 1307–1315. https://doi.org/10.1111/ele.12164

Belshe, E. F., Schuur, E. A. G., Bolker, B. M., & Bracho, R. (2012). Incorporating spatial heterogeneity created by permafrost thaw into a landscape carbon estimate. *Journal of Geophysical Research: Biogeosciences*, *117*(G1). https://doi.org/10.1029/2011JG001836

Belshe, E. F., Schuur, E. A. G., & Grosse, G. (2013). Quantification of upland thermokarst

features with high resolution remote sensing. *Environmental Research Letters*, *8*(3), 035016. https://doi.org/10.1088/1748-9326/8/3/035016

Berner, L. T., Massey, R., Jantz, P., Forbes, B. C., Macias-Fauria, M., Myers-Smith, I., Kumpula, T., Gauthier, G., Andreu-Hayles, L., Gaglioti, B. V., Burns, P., Zetterberg, P., D'Arrigo, R., & Goetz, S. J. (2020). Summer warming explains widespread but not uniform greening in the Arctic tundra biome. *Nature Communications*, *11*(1), 4621. https://doi.org/10.1038/s41467-020-18479-5

Biskaborn, B. K., Smith, S. L., Noetzli, J., Matthes, H., Vieira, G., Streletskiy, D. A., Schoeneich, P., Romanovsky, V. E., Lewkowicz, A. G., Abramov, A., Allard, M., Boike, J., Cable, W. L., Christiansen, H. H., Delaloye, R., Diekmann, B., Drozdov, D., Etzelmüller, B., Grosse, G., … Lantuit, H. (2019). Permafrost is warming at a global scale. *Nature Communications*, *10*(1), 264. https://doi.org/10.1038/s41467-018-08240-4

Bivand, R. S., Pebesma, E., & Gómez-Rubio, V. (2008). *Applied Spatial Data Analysis with R* (R. Gentleman, K. Hornik, & G. Parmigiani, Eds.). Springer Science + Business Media, LLC.

Blanc-Betes, E., Welker, J. M., Sturchio, N. C., Chanton, J. P., & Gonzalez-Meler, M. A. (2016). Winter precipitation and snow accumulation drive the methane sink or source strength of Arctic tussock tundra. *Global Change Biology*, *22*(8), 2818–2833. https://doi.org/10.1111/gcb.13242

Brady, N. C., & Weil, R. R. (2008). *The Nature and Properties of Soils* (14th ed.). Pearson Education, Inc.

Brown, J., Hinkel, K. M., & Nelson, F. E. (2000). The circumpolar active layer monitoring (calm) program: Research designs and initial results. *Polar Geography*, *24*(3), 166–258. https://doi.org/10.1080/10889370009377698

Bunn, A. G., & Goetz, S. J. (2006). Trends in Satellite-Observed Circumpolar Photosynthetic Activity from 1982 to 2003: The Influence of Seasonality, Cover Type, and Vegetation Density. *Earth Interactions*, *10*(12), 1–19. https://doi.org/10.1175/EI190.1

Burke, S. A., Wik, M., Lang, A., Contosta, A. R., Palace, M., Crill, P. M., & Varner, R. K. (2019). Long-term measurements of methane ebullition from thaw ponds. *Journal of Geophysical Research: Biogeosciences*, *124*(7), 2208–2221. https://doi.org/10.1029/2018JG004786

Campitelli, E. (2021). *ggnewscale: Multiple fill and colour scales in "ggplot2"* (0.4.5) [R]. https://CRAN.R-project.org/package=ggnewscale

Cassidy, A. E., Christen, A., & Henry, G. H. R. (2016). The effect of a permafrost disturbance on growing-season carbon-dioxide fluxes in a high Arctic tundra ecosystem. *Biogeosciences*, *13*(8), 2291–2303. https://doi.org/10.5194/bg-13-2291-2016

Celis, G., Mauritz, M., Bracho, R., Salmon, V. G., Webb, E. E., Hutchings, J., Natali, S. M., Schädel, C., Crummer, K. G., & Schuur, E. A. G. (2017). Tundra is a consistent source of CO_2 at a site with progressive permafrost thaw during 6 years of chamber and eddy covariance measurements: Tundra CO_2 Fluxes. *Journal of Geophysical Research: Biogeosciences*, *122*(6), 1471–1485. https://doi.org/10.1002/2016JG003671

Celis, G., Mauritz, M., Taylor, M., Ledman, J., Natali, S. M., Schuur, E. A. G., & Bonanza Creek LTER. (2018). Eight Mile Lake Research Watershed: Hourly meteorological data, 2004-2018 ver 23. *Environmental Data Initiative*. https://doi.org/10.6073/pasta/ec2da48c393574c7b62baa8140c86ae8

Chapin, F. S., Shaver, G. R., Giblin, A. E., Nadelhoffer, K. J., & Laundre, J. A. (1995). Responses of Arctic Tundra to Experimental and Observed Changes in Climate. *Ecology*, *76*(3), 694–711. https://doi.org/10.2307/1939337

Clayden, J. (2020). *mmand: Mathematical morphology in any number of dimensions* (1.6.1) [R]. https://CRAN.R-project.org/package=mmand

Collalti, A., & Prentice, I. C. (2019). Is NPP proportional to GPP? Waring's hypothesis 20 years on. *Tree Physiology*, *39*(8), 1473–1483. https://doi.org/10.1093/treephys/tpz034

Collins, C. G., Elmendorf, S. C., Hollister, R. D., Henry, G. H. R., Clark, K., Bjorkman, A. D., Myers-Smith, I. H., Prevéy, J. S., Ashton, I. W., Assmann, J. J., Alatalo, J. M., Carbognani, M., Chisholm, C., Cooper, E. J., Forrester, C., Jónsdóttir, I. S., Klanderud, K., Kopp, C. W., Livensperger, C., … Suding, K. N. (2021). Experimental warming differentially affects vegetative and reproductive phenology of tundra plants. *Nature Communications*, *12*(1), 3442. https://doi.org/10.1038/s41467-021-23841-2

Commane, R., Lindaas, J., Benmergui, J., Luus, K. A., Chang, R. Y.-W., Daube, B. C., Euskirchen, E. S., Henderson, J. M., Karion, A., Miller, J. B., Miller, S. M., Parazoo, N. C., Randerson, J. T., Sweeney, C., Tans, P., Thoning, K., Veraverbeke, S., Miller, C. E., & Wofsy, S. C. (2017). Carbon dioxide sources from Alaska driven by increasing early winter respiration from Arctic tundra. *Proceedings of the National Academy of Sciences*, *114*(21), 5361–5366. https://doi.org/10.1073/pnas.1618567114

Congalton, R. G., & Green, K. (2019). *Assessing the accuracy of remotely sensed data: Principles and practices* (3rd ed.). CRC Press.

Connon, R., Devoie, É., Hayashi, M., Veness, T., & Quinton, W. (2018). The Influence of Shallow Taliks on Permafrost Thaw and Active Layer Dynamics in Subarctic Canada. *Journal of Geophysical Research: Earth Surface*, *123*(2), 281–297. https://doi.org/10.1002/2017JF004469

Cooper, M. D. A., Estop-Aragonés, C., Fisher, J. P., Thierry, A., Garnett, M. H., Charman, D. J., Murton, J. B., Phoenix, G. K., Treharne, R., Kokelj, S. V., Wolfe, S. A., Lewkowicz, A. G., Williams, M., & Hartley, I. P. (2017). Limited contribution of permafrost carbon to methane release from thawing peatlands. *Nature Climate Change*, *7*(7), 507–511. https://doi.org/10.1038/nclimate3328

Cory, R. M., Crump, B. C., Dobkowski, J. A., & Kling, G. W. (2013). Surface exposure to sunlight stimulates CO_2 release from permafrost soil carbon in the Arctic. *Proceedings of the National Academy of Sciences*, *110*(9), 3429–3434. https://doi.org/10.1073/pnas.1214104110

Curasi, S. R., Loranty, M. M., & Natali, S. M. (2016). Water track distribution and effects on carbon dioxide flux in an eastern Siberian upland tundra landscape. *Environmental Research Letters*, *11*(4), 045002. https://doi.org/10.1088/1748-9326/11/4/045002

De Reu, J., Bourgeois, J., Bats, M., Zwertvaegher, A., Gelorini, V., De Smedt, P., Chu, W., Antrop, M., De Maeyer, P., Finke, P., Van Meirvenne, M., Verniers, J., & Crombé, P. (2013). Application of the topographic position index to heterogeneous landscapes. *Geomorphology*, *186*, 39–49. https://doi.org/10.1016/j.geomorph.2012.12.015

Deane-Coe, K. K., Mauritz, M., Celis, G., Salmon, V., Crummer, K. G., Natali, S. M., & Schuur, E. A. G. (2015). Experimental Warming Alters Productivity and Isotopic Signatures of Tundra Mosses. *Ecosystems*, *18*(6), 1070–1082. https://doi.org/10.1007/s10021-015-9884-7

Delwiche, K. B., Knox, S. H., Malhotra, A., Fluet-Chouinard, E., McNicol, G., Feron, S., Ouyang, Z., Papale, D., Trotta, C., Canfora, E., Cheah, Y.-W., Christianson, D., Alberto, M. C. R., Alekseychik, P., Aurela, M., Baldocchi, D., Bansal, S., Billesbach, D. P., Bohrer, G., … Jackson, R. B. (2021). *FLUXNET-CH4: A global, multi-ecosystem dataset and analysis of methane seasonality from freshwater wetlands* [Preprint]. Biosphere – Biogeosciences. https://doi.org/10.5194/essd-2020-307

DeMarco, J., Mack, M. C., Bret-Harte, M. S., Burton, M., & Shaver, G. R. (2014). Long-term experimental warming and nutrient additions increase productivity in tall deciduous shrub tundra. *Ecosphere*, *5*(6), art72. https://doi.org/10.1890/ES13-00281.1

Devoie, É. G., Craig, J. R., Connon, R. F., & Quinton, W. L. (2019). Taliks: A tipping point in discontinuous permafrost degradation in peatlands. *Water Resources Research*, *55*(11), 9838–9857. https://doi.org/10.1029/2018WR024488

Dowle, M., & Srinivasan, A. (2021). *data.table: Extension of `data.frame`*. (1.14.0) [R]. https://CRAN.R-project.org/package=data.table

Ekici, A., Lee, H., Lawrence, D. M., Swenson, S. C., & Prigent, C. (2019). Ground subsidence effects on simulating dynamic high-latitude surface inundation under permafrost thaw using CLM5. *Geoscientific Model Development*, *12*(12), 5291–5300. https://doi.org/10.5194/gmd-12-5291-2019

Elzhov, T. V., Mullen, K. M., Spiess, A.-N., & Bolker, B. M. (2016). *minpack.lm: R interface to the Levenberg-Marquardt nonlinear least-squares algorithm found in MINPACK, plus support for bounds* (1.2-1) [R]. https://CRAN.R-project.org/package=minpack.lm

Emmerton, C. A., St. Louis, V. L., Humphreys, E. R., Gamon, J. A., Barker, J. D., & Pastorello, G. Z. (2016). Net ecosystem exchange of CO_2 with rapidly changing high Arctic landscapes. *Global Change Biology*, *22*(3), 1185–1200. https://doi.org/10.1111/gcb.13064

Euskirchen, E. S., Edgar, C. W., Syndonia Bret-Harte, M., Kade, A., Zimov, N., & Zimov, S. (2017). Interannual and seasonal patterns of carbon dioxide, water, and energy fluxes from ecotonal and thermokarst-impacted ecosystems on carbon-rich permafrost soils in northeastern Siberia. *Journal of Geophysical Research: Biogeosciences*, *122*(10), 2651–2668. https://doi.org/10.1002/2017JG004070

Euskirchen, E. S., Edgar, C. W., Turetsky, M. R., Waldrop, M. P., & Harden, J. W. (2014). Differential response of carbon fluxes to climate in three peatland ecosystems that vary in the presence and stability of permafrost: Carbon fluxes and permafrost thaw. *Journal of Geophysical Research: Biogeosciences*, *119*(8), 1576–1595.

https://doi.org/10.1002/2014JG002683

Evans, S. G., Godsey, S. E., Rushlow, C. R., & Voss, C. (2020). Water Tracks Enhance Water Flow Above Permafrost in Upland Arctic Alaska Hillslopes. *Journal of Geophysical Research: Earth Surface*, *125*(2). https://doi.org/10.1029/2019JF005256

Farquharson, L. M., Romanovsky, V. E., Cable, W. L., Walker, D. A., Kokelj, S. V., & Nicolsky, D. (2019). Climate change drives widespread and rapid thermokarst development in very cold permafrost in the Canadian high Arctic. *Geophysical Research Letters*, *46*(12), 6681–6689. https://doi.org/10.1029/2019GL082187

French, H., & Shur, Y. (2010). The principles of cryostratigraphy. *Earth-Science Reviews*, *101*(3–4), 190–206. https://doi.org/10.1016/j.earscirev.2010.04.002

Garnier, S., Ross, N., Rudis, R., Sciaini, M., & Scherer, C. (2021). *Rvision—Colorblind-friendly color maps for R* (0.6.1) [R]. https://cran.r-project.org/web/packages/viridis/index.html

Goetz, S. J., Bunn, A. G., Fiske, G. J., & Houghton, R. A. (2005). Satellite-observed photosynthetic trends across boreal North America associated with climate and fire disturbance. *Proceedings of the National Academy of Sciences*, *102*(38), 13521–13525. https://doi.org/10.1073/pnas.0506179102

Gräler, B., Pebesma, E., & Heuvelink, G. (2016). Spatio-Temporal Interpolation using gstat. *The R Journal*, *8*(1), 204–218.

Greenwell, B., Boehmke, B., Cunningham, J., & GBM Developers. (2020). *gbm: Generalized boosted regression models* (2.1.8) [R]. https://CRAN.R-project.org/package=gbm

Grønlund, A., Hauge, A., Hovde, A., & Rasse, D. P. (2008). Carbon loss estimates from cultivated peat soils in Norway: A comparison of three methods. *Nutrient Cycling in Agroecosystems*, *81*(2), 157–167. https://doi.org/10.1007/s10705-008-9171-5

Grosse, G., Morgenstern, A., & Lantuit, H. (2008). *Distribution of thermokarst lakes and ponds at three yedoma sites in Siberia*. 6.

Grosse, G., Schirrmeister, L., & Malthus, T. J. (2006). Application of Landsat-7 satellite data and a DEM for the quantification of thermokarst-affected terrain types in the periglacial Lena?Anabar coastal lowland. *Polar Research*, *25*(1), 51–67. https://doi.org/10.1111/j.1751-8369.2006.tb00150.x

Harden, J. W., Koven, C. D., Ping, C.-L., Hugelius, G., David McGuire, A., Camill, P., Jorgenson, T., Kuhry, P., Michaelson, G. J., O'Donnell, J. A., Schuur, E. A. G., Tarnocai, C., Johnson, K., & Grosse, G. (2012). Field information links permafrost carbon to physical vulnerabilities of thawing. *Geophysical Research Letters*, *39*(15). https://doi.org/10.1029/2012GL051958

Harris, C., & Murton, J. B. (2005). Interactions between glaciers and permafrost: An introduction. *Geological Society, London, Special Publications*, *242*(1), 1–9. https://doi.org/10.1144/GSL.SP.2005.242.01.01

Hayes, D. J., Kicklighter, D. W., McGuire, A. D., Chen, M., Zhuang, Q., Yuan, F., Melillo, J. M., & Wullschleger, S. D. (2014). The impacts of recent permafrost thaw on land–atmosphere

greenhouse gas exchange. *Environmental Research Letters*, *9*(4), 045005. https://doi.org/10.1088/1748-9326/9/4/045005

Heiskanen, L., Tuovinen, J.-P., Räsänen, A., Virtanen, T., Juutinen, S., Lohila, A., Penttilä, T., Linkosalmi, M., Mikola, J., Laurila, T., & Aurela, M. (2021). Carbon dioxide and methane exchange of a patterned subarctic fen during two contrasting growing seasons. *Biogeosciences*, *18*(3), 873–896. https://doi.org/10.5194/bg-18-873-2021

Hewitt, R. E., DeVan, M. R., Lagutina, I. V., Genet, H., McGuire, A. D., Taylor, D. L., & Mack, M. C. (2019). Mycobiont contribution to tundra plant acquisition of permafrost-derived nitrogen. *New Phytologist*, 16.

Hewitt, R. E., Taylor, D. L., Genet, H., McGuire, A. D., & Mack, C. (2018). *Below-ground plant traits influence tundra plant acquisition of newly thawed permafrost nitrogen*. 13.

Hicks Pries, C. E., Schuur, E. A. G., & Crummer, K. G. (2012). Holocene Carbon Stocks and Carbon Accumulation Rates Altered in Soils Undergoing Permafrost Thaw. *Ecosystems*, *15*(1), 162–173. https://doi.org/10.1007/s10021-011-9500-4

Hicks Pries, C. E., Schuur, E. A. G., & Crummer, K. G. (2013). Thawing permafrost increases old soil and autotrophic respiration in tundra: Partitioning ecosystem respiration using $\delta^{13}C$ and $\Delta^{14}C$. *Global Change Biology*, *19*(2), 649–661. https://doi.org/10.1111/gcb.12058

Hicks Pries, C. E., Schuur, E. A. G., Natali, S. M., & Crummer, K. G. (2016). Old soil carbon losses increase with ecosystem respiration in experimentally thawed tundra. *Nature Climate Change*, *6*(2), 214–218. https://doi.org/10.1038/nclimate2830

Hicks Pries, C. E., Schuur, E. A. G., Vogel, J. G., & Natali, S. M. (2013). Moisture drives surface decomposition in thawing tundra. *Journal of Geophysical Research: Biogeosciences*, *118*(3), 1133–1143. https://doi.org/10.1002/jgrg.20089

Hicks Pries, C. E., van Logtestijn, R. S. P., Schuur, E. A. G., Natali, S. M., Cornelissen, J. H. C., Aerts, R., & Dorrepaal, E. (2015). Decadal warming causes a consistent and persistent shift from heterotrophic to autotrophic respiration in contrasting permafrost ecosystems. *Global Change Biology*, *21*(12), 4508–4519. https://doi.org/10.1111/gcb.13032

Hiemstra, P. H., Pebesma, E., Twenhöfel, C. J. W., & Heuvelink, G. B. M. (2009). *Real-time automatic interpolation of ambient gamma dose rates from the Dutch Radioactivity Monitoring Network*. *35*(8), 1711–1721.

Hijmans, R. J. (2019). *raster: Geographic data analysis and modeling* (2.8-19) [R]. https://CRAN.R-project.org/package=raster

Hijmans, R. J. (2021). *raster: Geographic data analysis and modeling* (3.4-10) [R]. https://CRAN.R-project.org/package=raster

Hinkel, K. M., & Hurd, J. K. (2006). Permafrost Destabilization and Thermokarst Following Snow Fence Installation, Barrow, Alaska, U.S.A. *Arctic, Antarctic, and Alpine Research*, *38*(4), 530–539. https://doi.org/10.1657/1523-0430(2006)38[530:PDATFS]2.0.CO;2

Hinkel, K. M., & Nelson, F. E. (2003). Spatial and temporal patterns of active layer thickness at

Circumpolar Active Layer Monitoring (CALM) sites in northern Alaska, 1995–2000. *Journal of Geophysical Research*, *108*(D2), 8168. https://doi.org/10.1029/2001JD000927

Hobbie, S. E., & Chapin, F. S. (1998). The response of tundra plant biomass, aboveground production, nitrogen, and CO_2 flux to experimental warming. *Ecology*, *79*(5), 1526–1544. https://doi.org/10.1890/0012-9658(1998)079[1526:TROTPB]2.0.CO;2

Houghton, R. A. (2007). Balancing the global carbon budget. *Annual Review of Earth and Planetary Sciences*, *35*, 313–347.

Hugelius, G., Strauss, J., Zubrzycki, S., Harden, J. W., Schuur, E. A. G., Ping, C.-L., Schirrmeister, L., Grosse, G., Michaelson, G. J., Koven, C. D., O'Donnell, J. A., Elberling, B., Mishra, U., Camill, P., Yu, Z., Palmtag, J., & Kuhry, P. (2014). Estimated stocks of circumpolar permafrost carbon with quantified uncertainty ranges and identified data gaps. *Biogeosciences*, *11*(23), 6573–6593. https://doi.org/10.5194/bg-11-6573-2014

IPCC. (2013). *Climate Change 2013: The Physical Science Basis. Contribution of Working Group I to the Fifth Assessment Report of the Intergovernmental Panel on Climate Change*. Cambridge University Press.

IPCC. (2021). *Climate Change 2021: The Physical Science Basis. Contribution of Working Group I to the Sixth Assessment Report of the Intergovernmental Panel on Climate Change*. Cambridge University Press.

Jensen, A. E., Lohse, K. A., Crosby, B. T., & Mora, C. I. (2014). Variations in soil carbon dioxide efflux across a thaw slump chronosequence in northwestern Alaska. *Environmental Research Letters*, *9*(2), 025001. https://doi.org/10.1088/1748-9326/9/2/025001

Johansson, M., Callaghan, T. V., Bosiö, J., Åkerman, H. J., Jackowicz-Korczynski, M., & Christensen, T. R. (2013). Rapid responses of permafrost and vegetation to experimentally increased snow cover in sub-arctic Sweden. *Environmental Research Letters*, *8*(3), 035025. https://doi.org/10.1088/1748-9326/8/3/035025

Johnston, C. E., Ewing, S. A., Harden, J. W., Varner, R. K., Wickland, K. P., Koch, J. C., Fuller, C. C., Manies, K., & Jorgenson, M. T. (2014). Effect of permafrost thaw on CO_2 and CH_4 exchange in a western Alaska peatland chronosequence. *Environmental Research Letters*, *9*(8), 085004. https://doi.org/10.1088/1748-9326/9/8/085004

Jones, B. M., Grosse, G., Arp, C. D., Miller, E., Liu, L., Hayes, D. J., & Larsen, C. F. (2015). Recent Arctic tundra fire initiates widespread thermokarst development. *Scientific Reports*, *5*(1), 15865. https://doi.org/10.1038/srep15865

Jones, B. M., Stoker, J. M., Gibbs, A. E., Grosse, G., Romanovsky, V. E., Douglas, T. A., Kinsman, N. E. M., & Richmond, B. M. (2013). Quantifying landscape change in an arctic coastal lowland using repeat airborne LiDAR. *Environmental Research Letters*, *8*(4), 045025. https://doi.org/10.1088/1748-9326/8/4/045025

Jones, M. C., Grosse, G., Jones, B. M., & Walter Anthony, K. (2012). Peat accumulation in drained thermokarst lake basins in continuous, ice-rich permafrost, northern Seward Peninsula, Alaska. *Journal of Geophysical Research: Biogeosciences*, *117*(G2), n/a-n/a. https://doi.org/10.1029/2011JG001766

Jorgenson, M. T., Douglas, T. A., Liljedahl, A. K., Roth, J. E., Cater, T. C., Davis, W. A., Frost, G. V., Miller, P. F., & Racine, C. H. (2020). The roles of climate extremes, ecological succession, and hydrology in repeated permafrost aggradation and degradation in fens on the Tanana Flats, Alaska. *Journal of Geophysical Research: Biogeosciences*, *125*(12). https://doi.org/10.1029/2020JG005824

Jorgenson, M. T., & Osterkamp, T. E. (2005). Response of boreal ecosystems to varying modes of permafrost degradation. *Canadian Journal of Forest Research*, *35*, 2100–2111. https://doi.org/10.1139/X05-153

Jorgenson, M. T., Racine, C. H., Walters, J. C., & Osterkamp, T. E. (2001). Permafrost Degradation and Ecological Changes Associated with a WarmingClimate in Central Alaska. *Climatic Change*, *48*, 551–579.

Jorgenson, M. T., Romanovsky, V., Harden, J., Shur, Y., O'Donnell, J., Schuur, E. A. G., Kanevskiy, M., & Marchenko, S. (2010). Resilience and vulnerability of permafrost to climate change. *Canadian Journal of Forest Research*, *40*, 1219–1236. https://doi.org/10.1139/X10-060

Jorgenson, M. T., Shur, Y. L., & Pullman, E. R. (2006). Abrupt increase in permafrost degradation in Arctic Alaska. *Geophysical Research Letters*, *33*(2), L02503. https://doi.org/10.1029/2005GL024960

Jorgenson, T. M., Harden, J., Kanevskiy, M., O'Donnell, J., Wickland, K., Ewing, S., Manies, K., Zhuang, Q., Shur, Y., Striegl, R., & Koch, J. (2013). Reorganization of vegetation, hydrology and soil carbon after permafrost degradation across heterogeneous boreal landscapes. *Environmental Research Letters*, *8*(3), 035017. https://doi.org/10.1088/1748-9326/8/3/035017

Kääb, A. (2008). Remote sensing of permafrost-related problems and hazards. *Permafrost and Periglacial Processes*, *19*(2), 107–136. https://doi.org/10.1002/ppp.619

Kanevskiy, M., Shur, Y., Jorgenson, M. T., Ping, C.-L., Michaelson, G. J., Fortier, D., Stephani, E., Dillon, M., & Tumskoy, V. (2013). Ground ice in the upper permafrost of the Beaufort Sea coast of Alaska. *Cold Regions Science and Technology*, *85*, 56–70. https://doi.org/10.1016/j.coldregions.2012.08.002

Kanevskiy, M., Shur, Y., Jorgenson, T., Brown, D. R. N., Moskalenko, N., Brown, J., Walker, D. A., Raynolds, M. K., & Buchhorn, M. (2017). Degradation and stabilization of ice wedges: Implications for assessing risk of thermokarst in northern Alaska. *Geomorphology*, *297*, 20–42. https://doi.org/10.1016/j.geomorph.2017.09.001

Kassambara, A. (2020). *ggpubr: "ggplot2" based publication ready plots* (0.4.0) [R]. https://CRAN.R-project.org/package=ggpubr

Kelsey, K. C., Pedersen, S. H., Leffler, A. J., Sexton, J. O., Feng, M., & Welker, J. M. (2021). Winter snow and spring temperature have differential effects on vegetation phenology and productivity across Arctic plant communities. *Global Change Biology*, *27*(8), 1572–1586. https://doi.org/10.1111/gcb.15505

Kljun, N., Calanca, P., Rotach, M. W., & Schmid, H. P. (2015). A simple two-dimensional

parameterisation for Flux Footprint Prediction (FFP). *Geoscientific Model Development*, *8*(11), 3695–3713. https://doi.org/10.5194/gmd-8-3695-2015

Köchy, M., Hiederer, R., & Freibauer, A. (2015). Global distribution of soil organic carbon – Part 1: Masses and frequency distributions of SOC stocks for the tropics, permafrost regions, wetlands, and the world. *SOIL*, *1*(1), 351–365. https://doi.org/10.5194/soil-1-351-2015

Kokelj, S. V., & Burn, C. R. (2003). Ground ice and soluble cations in near-surface permafrost, Inuvik, Northwest Territories, Canada. *Permafrost and Periglacial Processes*, *14*(3), 275–289. https://doi.org/10.1002/ppp.458

Kokelj, S. V., & Jorgenson, M. T. (2013). Advances in thermokarst research: Recent advances in research investigating thermokarst processes. *Permafrost and Periglacial Processes*, *24*(2), 108–119. https://doi.org/10.1002/ppp.1779

Kokelj, S. V., Kokoszka, J., van der Sluijs, J., Rudy, A. C. A., Tunnicliffe, J., Shakil, S., Tank, S., & Zolkos, S. (2020). *Permafrost thaw couples slopes with downstream systems and effects propagate throughArctic drainage networks* [Preprint]. Frozen ground/Geomorphology. https://doi.org/10.5194/tc-2020-218

Kokelj, S. V., Lantz, T. C., Kanigan, J., Smith, S. L., & Coutts, R. (2009). Origin and polycyclic behaviour of tundra thaw slumps, Mackenzie Delta region, Northwest Territories, Canada. *Permafrost and Periglacial Processes*, *20*(2), 173–184. https://doi.org/10.1002/ppp.642

Kotani, A., Saito, A., Kononov, A. V., Petrov, R. E., Maximov, T. C., Iijima, Y., & Ohta, T. (2019). Impact of unusually wet permafrost soil on understory vegetation and CO2 exchange in a larch forest in eastern Siberia. *Agricultural and Forest Meteorology*, *265*, 295–309. https://doi.org/10.1016/j.agrformet.2018.11.025

Kuhn, M. (2021). *caret: Classification and regression training* (6.0-90) [R]. https://CRAN.R-project.org/package=caret

Kutzbach, L., Wagner, D., & Pfeiffer, E.-M. (2004). Effect of microrelief and vegetation on methane emission from wet polygonal tundra, Lena Delta, Northern Siberia. *Biogeochemistry*, *69*(3), 341–362. https://doi.org/10.1023/B:BIOG.0000031053.81520.db

Lantz, T. C., & Kokelj, S. V. (2008). Increasing rates of retrogressive thaw slump activity in the Mackenzie Delta region, N.W.T., Canada. *Geophysical Research Letters*, *35*(6), L06502. https://doi.org/10.1029/2007GL032433

Lara, M. J., Genet, H., McGuire, A. D., Euskirchen, E. S., Zhang, Y., Brown, D. R. N., Jorgenson, M. T., Romanovsky, V., Breen, A., & Bolton, W. R. (2016). Thermokarst rates intensify due to climate change and forest fragmentation in an Alaskan boreal forest lowland. *Global Change Biology*, *22*(2), 816–829. https://doi.org/10.1111/gcb.13124

Lara, M. J., McGuire, A. D., Euskirchen, E. S., Genet, H., Yi, S., Rutter, R., Iversen, C., Sloan, V., & Wullschleger, S. D. (2020). Local-scale Arctic tundra heterogeneity affects regional-scale carbon dynamics. *Nature Communications*, *11*(1), 4925. https://doi.org/10.1038/s41467-020-18768-z

Lawrence, D. M., Koven, C. D., Swenson, S. C., Riley, W. J., & Slater, A. G. (2015). Permafrost

thaw and resulting soil moisture changes regulate projected high-latitude CO_2 and CH_4 emissions. *Environmental Research Letters*, *10*(9), 094011. https://doi.org/10.1088/1748-9326/10/9/094011

Lee, H., Schuur, E. A. G., & Vogel, J. G. (2010). Soil CO_2 production in upland tundra where permafrost is thawing. *Journal of Geophysical Research*, *115*(G1), G01009. https://doi.org/10.1029/2008JG000906

Lee, H., Schuur, E. A. G., Vogel, J. G., Lavoie, M., Bhadra, D., & Staudhammer, C. L. (2011). A spatially explicit analysis to extrapolate carbon fluxes in upland tundra where permafrost is thawing. *Global Change Biology*, *17*(3), 1379–1393. https://doi.org/10.1111/j.1365-2486.2010.02287.x

Lenth, R. V. (2021). *emmeans: Estimated marginal means, aka least-squares means* (1.6.1) [R]. https://CRAN.R-project.org/package=emmeans

Lindgren, P. R., Grosse, G., Walter Anthony, K. M., & Meyer, F. J. (2016). Detection and spatiotemporal analysis of methane ebullition on thermokarst lake ice using high-resolution optical aerial imagery. *Biogeosciences*, *13*(1), 27–44. https://doi.org/10.5194/bg-13-27-2016

Liu, L., Zhang, T., & Wahr, J. (2010). InSAR measurements of surface deformation over permafrost on the North Slope of Alaska. *Journal of Geophysical Research*, *115*(F3), F03023. https://doi.org/10.1029/2009JF001547

Luo, D., Wu, Q., Jin, H., Marchenko, S. S., Lü, L., & Gao, S. (2016). Recent changes in the active layer thickness across the northern hemisphere. *Environmental Earth Sciences*, *75*(7), 555. https://doi.org/10.1007/s12665-015-5229-2

Marion, G. M., Henry, G. H. R., Freckman, D. W., Johnstone, J., Jones, G., Jones, M. H., Lévesque, E., Molau, U., Mølgaard, P., Parsons, A. N., J. Svoboda, & Virginia, R. A. (1997). Open-top designs for manipulating field temperature in high-latitude ecosystems. *Global Change Biology*, *3*(S1), 20–32. https://doi.org/10.1111/j.1365-2486.1997.gcb136.x

Mauritz, M., Bracho, R., Celis, G., Hutchings, J., Natali, S. M., Pegoraro, E., Salmon, V. G., Schädel, C., Webb, E. E., & Schuur, E. A. G. (2017). Nonlinear CO_2 flux response to 7 years of experimentally induced permafrost thaw. *Global Change Biology*, *23*(9), 3646–3666. https://doi.org/10.1111/gcb.13661

Morgenstern, A., Overduin, P. P., Günther, F., Stettner, S., Ramage, J., Schirrmeister, L., Grigoriev, M. N., & Grosse, G. (2021). Thermo-erosional valleys in Siberian ice-rich permafrost. *Permafrost and Periglacial Processes*, *32*(1), 59–75. https://doi.org/10.1002/ppp.2087

Mu, C., Zhang, T., Zhang, X., Li, L., Guo, H., Zhao, Q., Cao, L., Wu, Q., & Cheng, G. (2016). Carbon loss and chemical changes from permafrost collapse in the northern Tibetan Plateau. *Journal of Geophysical Research: Biogeosciences*, *121*(7), 1781–1791. https://doi.org/10.1002/2015JG003235

Myhre, G., Shindell, D., & Pongratz, J. (2014). Anthropogenic and natural radiative forcing. In

Climate change (pp. 659–740). Cambridge, United Kingdom: Cambridge University Press. In *Climate change 2013: The physical science basis; Working Group I contribution to the fifth assessment report of the Intergovernmental Panel on Climate Change.* Cambridge University Press.

Natali, S. M., Holdren, J. P., Rogers, B. M., Treharne, R., Duffy, P. B., Pomerance, R., & MacDonald, E. (2021). Permafrost carbon feedbacks threaten global climate goals. *Proceedings of the National Academy of Sciences*, *118*(21), e2100163118. https://doi.org/10.1073/pnas.2100163118

Natali, S. M., Schuur, E. A. G., Mauritz, M., Schade, J. D., Celis, G., Crummer, K. G., Johnston, C., Krapek, J., Pegoraro, E., Salmon, V. G., & Webb, E. E. (2015). Permafrost thaw and soil moisture driving CO_2 and CH_4 release from upland tundra. *Journal of Geophysical Research: Biogeosciences*, *120*(3), 525–537. https://doi.org/10.1002/2014JG002872

Natali, S. M., Schuur, E. A. G., & Rubin, R. L. (2012). Increased plant productivity in Alaskan tundra as a result of experimental warming of soil and permafrost: Increased plant productivity in Alaskan tundra. *Journal of Ecology*, *100*(2), 488–498. https://doi.org/10.1111/j.1365-2745.2011.01925.x

Natali, S. M., Schuur, E. A. G., Trucco, C., Hicks Pries, C. E., Crummer, K. G., & Baron Lopez, A. F. (2011). Effects of experimental warming of air, soil and permafrost on carbon balance in Alaskan tundra. *Global Change Biology*, *17*(3), 1394–1407. https://doi.org/10.1111/j.1365-2486.2010.02303.x

Natali, S. M., Watts, J. D., Rogers, B. M., Potter, S., Ludwig, S. M., Selbmann, A.-K., Sullivan, P. F., Abbott, B. W., Arndt, K. A., Birch, L., Björkman, M. P., Bloom, A. A., Celis, G., Christensen, T. R., Christiansen, C. T., Commane, R., Cooper, E. J., Crill, P., Czimczik, C., … Zona, D. (2019). Large loss of CO_2 in winter observed across the northern permafrost region. *Nature Climate Change*, *9*(11), 852–857. https://doi.org/10.1038/s41558-019-0592-8

Nauta, A. L., Heijmans, M. M. P. D., Blok, D., Limpens, J., Elberling, B., Gallagher, A., Li, B., Petrov, R. E., Maximov, T. C., van Huissteden, J., & Berendse, F. (2015). Permafrost collapse after shrub removal shifts tundra ecosystem to a methane source. *Nature Climate Change*, *5*(1), 67–70. https://doi.org/10.1038/nclimate2446

Nelson, F. E., Anisimov, O. A., & Shiklomanov, N. I. (2001). Subsidence risk from thawing permafrost. *Nature*, *410*(6831), 889–890. https://doi.org/10.1038/35073746

NEON (National Ecological Observatory Network). (2017a). *Elevation—LiDAR, RELEASE-2017 (DP3.30024.001)*. http://data.neonscience.org

NEON (National Ecological Observatory Network). (2017b). *Soil physical properties (DP1.10047.001)*. http://data.neonscience.org

NEON (National Ecological Observatory Network). (2018). *High-resolution orthorectified camera imagery mosaic, RELEASE-2018 (DP3.30010.001)*. https://doi.org/10.48443/4e85-cr14

NEON (National Ecological Observatory Network). (2020a). *Elevation—LiDAR, RELEASE-*

2020 (DP3.30024.001). https://doi.org/10.48443/917d-g459

NEON (National Ecological Observatory Network). (2020b). *High-resolution orthorectified camera imagery mosaic, RELEASE-2020 (DP3.30010.001)*. https://doi.org/10.48443/4e85-cr14

Neubauer, S. C., & Megonigal, J. P. (2015). Moving beyond global warming potentials to quantify the climatic role of ecosystems. *Ecosystems*, *18*(6), 1000–1013. https://doi.org/10.1007/s10021-015-9879-4

Nitze, I., Cooley, S. W., Duguay, C. R., Jones, B. M., & Grosse, G. (2020). The catastrophic thermokarst lake drainage events of 2018 in northwestern Alaska: Fast-forward into the future. *The Cryosphere*, *14*(12), 4279–4297. https://doi.org/10.5194/tc-14-4279-2020

Nixon, F. M., & Taylor, A. E. (1998). *Regional active layer monitoring across the sporadic, discontinuous and continuous permafrost zones, Mackenzie Valley, Norhtwestern Canada*. 6.

Nyland, K. E., Shiklomanov, N. I., Streletskiy, D. A., Nelson, F. E., Klene, A. E., & Kholodov, A. L. (2021). Long-term Circumpolar Active Layer Monitoring (CALM) program observations in Northern Alaskan tundra. *Polar Geography*, 1–19. https://doi.org/10.1080/1088937X.2021.1988000

Olefeldt, D., Goswami, S., Grosse, G., Hayes, D., Hugelius, G., Kuhry, P., McGuire, A. D., Romanovsky, V. E., Sannel, A. B. K., Schuur, E. A. G., & Turetsky, M. R. (2016). Circumpolar distribution and carbon storage of thermokarst landscapes. *Nature Communications*, *7*(1), 13043. https://doi.org/10.1038/ncomms13043

O'Neill, H. B., & Burn, C. R. (2017). Talik Formation at a Snow Fence in Continuous Permafrost, Western Arctic Canada: Talik Formation at a Snow Fence. *Permafrost and Periglacial Processes*, *28*(3), 558–565. https://doi.org/10.1002/ppp.1905

O'Neill, H. B., Smith, S. L., & Duchesne, C. (2019). Long-Term Permafrost Degradation and Thermokarst Subsidence in the Mackenzie Delta Area Indicated by Thaw Tube Measurements. *Cold Regions Engineering 2019*, 643–651. https://doi.org/10.1061/9780784482599.074

Osterkamp, T. E. (2007). Characteristics of the recent warming of permafrost in Alaska. *Journal of Geophysical Research*, *112*(F2), F02S02. https://doi.org/10.1029/2006JF000578

Osterkamp, T. E., Jorgenson, M. T., Schuur, E. A. G., Shur, Y. L., Kanevskiy, M. Z., Vogel, J. G., & Tumskoy, V. E. (2009). Physical and ecological changes associated with warming permafrost and thermokarst in Interior Alaska. *Permafrost and Periglacial Processes*, *20*(3), 235–256. https://doi.org/10.1002/ppp.656

Osterkamp, T. E., & Romanovsky, V. E. (1999). *Evidence for warming and thawing of discontinuous permafrost in Alaska*. 21.

Parazoo, N. C., Koven, C. D., Lawrence, D. M., Romanovsky, V., & Miller, C. E. (2018). Detecting the permafrost carbon feedback: Talik formation and increased cold-season respiration as precursors to sink-to-source transitions. *The Cryosphere*, *12*(1), 123–144. https://doi.org/10.5194/tc-12-123-2018

Pebesma, E. (2004). Multivariable geostatistics in S: the gstat package. *Computers & Geosciences*, *30*, 683–691.

Pebesma, E. (2018). Simple Features for R: Standardized support for spatial vector data. *The R Journal*, *10*(1), 439. https://doi.org/10.32614/RJ-2018-009

Pebesma, E., & Bivand, R. S. (2005). Classes and methods for spatial data in R. *R News*, *5*(2). https://cran.r-project.org/doc/Rnews/

Pegoraro, E. F., Mauritz, M. E., Ogle, K., Ebert, C. H., & Schuur, E. A. G. (2020). Lower soil moisture and deep soil temperatures in thermokarst features increase old soil carbon loss after 10 years of experimental permafrost warming. *Global Change Biology*, *27*(6), 1293–1308. https://doi.org/10.1111/gcb.15481

Pegoraro, E., Mauritz, M., Bracho, R., Ebert, C., Dijkstra, P., Hungate, B. A., Konstantinidis, K. T., Luo, Y., Schädel, C., Tiedje, J. M., Zhou, J., & Schuur, E. A. G. (2019). Glucose addition increases the magnitude and decreases the age of soil respired carbon in a long-term permafrost incubation study. *Soil Biology and Biochemistry*, *129*, 201–211. https://doi.org/10.1016/j.soilbio.2018.10.009

Phillips, M. R., Burn, C. R., Wolfe, S. A., Morse, P. D., Gaanderse, A. J., O'Neill, H. B., Shugar, D. H., & Gruber, S. (n.d.). *Improving water content description of ice-rich permafrost soils*. 7.

Pirk, N., Mastepanov, M., López-Blanco, E., Christensen, L. H., Christiansen, H. H., Hansen, B. U., Lund, M., Parmentier, F.-J. W., Skov, K., & Christensen, T. R. (2017). Toward a statistical description of methane emissions from arctic wetlands. *Ambio*, *46*(S1), 70–80. https://doi.org/10.1007/s13280-016-0893-3

Pizano, C., Barón, A. F., Schuur, E. A. G., Crummer, K. G., & Mack, M. C. (2014). Effects of thermo-erosional disturbance on surface soil carbon and nitrogen dynamics in upland arctic tundra. *Environmental Research Letters*, *9*(7), 075006. https://doi.org/10.1088/1748-9326/9/7/075006

Plaza, C., Pegoraro, E., Bracho, R., Celis, G., Crummer, K. G., Hutchings, J. A., Hicks Pries, C. E., Mauritz, M., Natali, S. M., Salmon, V. G., Schädel, C., Webb, E. E., & Schuur, E. A. G. (2019). Direct observation of permafrost degradation and rapid soil carbon loss in tundra. *Nature Geoscience*, *12*(8), 627–631. https://doi.org/10.1038/s41561-019-0387-6

Plaza, C., Schuur, E. A. G., Pegoraro, E. F., & Bonanza Creek LTER. (2017). Eight Mile Lake Research Watershed, Carbon in Permafrost Experimental Heating Research (CiPEHR): Physical and chemical properties of soils, 2009-2013 ver 4. *Environmental Data Initiative*. https://doi.org/10.6073/pasta/f502d8fe1a2e1d6c6b035c198af04f3e

Polishchuk, Y. M., Bogdanov, A. N., Polishchuk, V. Y., Manasypov, R. M., Shirokova, L. S., Kirpotin, S. N., & Pokrovsky, O. S. (2017). *Size distribution, surface coverage, water, carbon, and metal storage of thermokarst lakes in the permafrost zone of the Western Siberia Lowland*. 18.

Porter, C., Morin, P., Howat, I., Noh, M.-J., Bates, B., Peterman, K., Keesey, S., Schlenk, M., Gardiner, J., Tomko, K., Willis, M., Kelleher, C., Cloutier, M., Husby, E., Foga, S.,

Nakamura, H., Platson, M., Wethington, M. Jr., Williamson, C., … Bojesen, M. (2018). *ArcticDEM* (V1 ed.) [Map]. Harvard Dataverse. https://doi.org/10.7910/DVN/OHHUKH

R Core Team. (2018). *R: A language and environment for statistical computing* (3.5.0) [Computer software]. R Foundation for Statistical Computing. https://www.R-project.org/

R Core Team. (2021). *R: A language and environment for statistical computing* (4.1.0) [Computer software]. R Foundation for Statistical Computing. https://www.R-project.org/

Raz-Yaseef, N., Torn, M. S., Wu, Y., Billesbach, D. P., Liljedahl, A. K., Kneafsey, T. J., Romanovsky, V. E., Cook, D. R., & Wullschleger, S. D. (2017). Large CO_2 and CH_4 emissions from polygonal tundra during spring thaw in northern Alaska: Spring Pulse Emission. *Geophysical Research Letters*, *44*(1), 504–513. https://doi.org/10.1002/2016GL071220

Rodenhizer, H., Belshe, E. F., Celis, G., Ledman, J., Mauritz, M., Goetz, S. J., Sankey, T., & Schuur, E. A. G. (in review). *Abrupt Permafrost Thaw Accelerates Carbon Dioxide and Methane Release at a Tussock Tundra Site*.

Rodenhizer, H., Celis, G., Bracho, R., & Schuur, E. A. G. (2021). AmeriFlux US-EML Eight Mile Lake permafrost thaw gradient, Healy Alaska., Ver. 4-5. *Ameriflux AMP*. https://doi.org/10.17190/AMF/1418678

Rodenhizer, H., Ledman, J., Mauritz, M., Natali, S. M., Pegoraro, E., Plaza, C., Romano, E., Schädel, C., Taylor, M., & Schuur, E. (2020). Carbon thaw rate doubles when accounting for subsidence in a permafrost warming experiment. *Journal of Geophysical Research: Biogeosciences*, *125*(6). https://doi.org/10.1029/2019JG005528

Rodenhizer, H., Mauritz, M. E., Taylor, M. A., Ledman, J., Natali, S. M., Schuur, E. A. G., & Bonanza Creek LTER. (2019a). Eight Mile Lake Research Watershed, Carbon in Permafrost Experimental Heating Research (CiPEHR): GPS Elevation, 2009-2019 ver 2. *Environmental Data Initiative*. https://doi.org/10.6073/pasta/9b181a01b52f254a9cdbcba007c0a165

Rodenhizer, H., Mauritz, M. E., Taylor, M. A., Ledman, J., Natali, S. M., Schuur, E. A. G., & Bonanza Creek LTER. (2019b). Eight Mile Lake Research Watershed, Carbon in Permafrost Experimental Heating Research (CiPEHR): GPS PLot Locations ver 2. *Environmental Data Initiative*. https://doi.org/10.6073/pasta/73e1738968a42877a37b4e0c80e07ef0

Rodenhizer, H., Mauritz, M. E., Taylor, M. A., Ledman, J., Natali, S. M., Schuur, E. A. G., & Bonanza Creek LTER. (2021). Eight Mile Lake Research Watershed, Carbon in Permafrost Experimental Heating Research (CiPEHR): GPS Elevation, 2009-2020 ver 3. *Environmental Data Initiative*. https://doi.org/10.6073/pasta/18922ce3170dc2abf1dcc78585302f45

Romano, E. (2018). *Dissolved organic carbon released from thawing permafrost soils and detected in headwater streams* [Northern Arizona University]. Proquest Theses and Dissertations.

Romanovsky, V. E., Sergueev, D. O., & Osterkamp, T. E. (2003). *Temporal variations in the*

active layer and near-surface permafrost temperatures at the long-term observatories in Northern Alaska. 6.

Salmon, V. G., Schädel, C., Bracho, R., Pegoraro, E., Celis, G., Mauritz, M., Mack, M. C., & Schuur, E. A. G. (2018). Adding Depth to Our Understanding of Nitrogen Dynamics in Permafrost Soils. *Journal of Geophysical Research: Biogeosciences*, *123*(8), 2497–2512. https://doi.org/10.1029/2018JG004518

Salmon, V. G., Soucy, P., Mauritz, M., Celis, G., Natali, S. M., Mack, M. C., & Schuur, E. A. G. (2016). Nitrogen availability increases in a tundra ecosystem during five years of experimental permafrost thaw. *Global Change Biology*, *22*(5), 1927–1941. https://doi.org/10.1111/gcb.13204

Schädel, C., Bader, M. K.-F., Schuur, E. A. G., Biasi, C., Bracho, R., Čapek, P., De Baets, S., Diáková, K., Ernakovich, J., Estop-Aragones, C., Graham, D. E., Hartley, I. P., Iversen, C. M., Kane, E., Knoblauch, C., Lupascu, M., Martikainen, P. J., Natali, S. M., Norby, R. J., … Wickland, K. P. (2016). Potential carbon emissions dominated by carbon dioxide from thawed permafrost soils. *Nature Climate Change*, *6*(10), 950–953. https://doi.org/10.1038/nclimate3054

Schädel, C., Koven, C. D., Lawrence, D. M., Celis, G., Garnello, A. J., Hutchings, J., Mauritz, M., Natali, S. M., Pegoraro, E., Rodenhizer, H., Salmon, V. G., Taylor, M. A., Webb, E. E., Wieder, W. R., & Schuur, E. A. (2018). Divergent patterns of experimental and model-derived permafrost ecosystem carbon dynamics in response to Arctic warming. *Environmental Research Letters*, *13*(10), 105002. https://doi.org/10.1088/1748-9326/aae0ff

Schuur, E. A. G., & Abbott, B. (2011). High risk of permafrost thaw. *Nature*, *480*(7375), 32–33. https://doi.org/10.1038/480032a

Schuur, E. A. G., Abbott, B. W., Ernakovich, J., Euskirchen, E. S., Hugelius, G., Grosse, G., Jones, M. C., Koven, C. D., Leshyk, V., Lawrence, D. M., Loranty, M. M., Mauritz, M., Olefeldt, D., Natali, S. M., Rodenhizer, H., Salmon, V. G., Schädel, C., Treat, C. C., Turetsky, M. R., & Wilson, C. J. (in review). *Permafrost and Climate Change: Carbon Cycle Feedbacks From the Warming Arctic*.

Schuur, E. A. G., Bockheim, J., Canadell, J. G., Euskirchen, E., Field, C. B., Goryachkin, S. V., Hagemann, S., Kuhry, P., Lafleur, P. M., Lee, H., Mazhitova, G., Nelson, F. E., Rinke, A., Romanovsky, V. E., Shiklomanov, N., Tarnocai, C., Venevsky, S., Vogel, J. G., & Zimov, S. A. (2008). Vulnerability of permafrost carbon to climate change: Implications for the global carbon cycle. *BioScience*, *58*(8), 701–714. https://doi.org/10.1641/B580807

Schuur, E. A. G., Bracho, R., Celis, G., Belshe, E. F., Ebert, C., Ledman, J., Mauritz, M., Pegoraro, E. F., Plaza, C., Rodenhizer, H., Romanovsky, V., Schädel, C., Schirokauer, D., Taylor, M., Vogel, J. G., & Webb, E. E. (2021). Tundra underlain by thawing permafrost persistently emits carbon to the atmosphere over 15 years of measurements. *Journal of Geophysical Research: Biogeosciences*, *126*(6). https://doi.org/10.1029/2020JG006044

Schuur, E. A. G., Crummer, K. G., Vogel, J. G., & Mack, M. C. (2007). Plant species composition and productivity following permafrost thaw and thermokarst in Alaskan

tundra. *Ecosystems*, *10*(2), 280–292. https://doi.org/10.1007/s10021-007-9024-0

Schuur, E. A. G., & Mack, M. C. (2018). Ecological response to permafrost thaw and consequences for local and global ecosystem services. *Annual Review of Ecology, Evolution, and Systematics*, *49*(1), 279–301. https://doi.org/10.1146/annurev-ecolsys-121415-032349

Schuur, E. A. G., McGuire, A. D., Schädel, C., Grosse, G., Harden, J. W., Hayes, D. J., Hugelius, G., Koven, C. D., Kuhry, P., Lawrence, D. M., Natali, S. M., Olefeldt, D., Romanovsky, V. E., Schaefer, K., Turetsky, M. R., Treat, C. C., & Vonk, J. E. (2015). Climate change and the permafrost carbon feedback. *Nature*, *520*(7546), 171–179. https://doi.org/10.1038/nature14338

Schuur, E. A. G., Vogel, J. G., Crummer, K. G., Lee, H., Sickman, J. O., & Osterkamp, T. E. (2009). The effect of permafrost thaw on old carbon release and net carbon exchange from tundra. *Nature*, *459*(7246), 556–559. https://doi.org/10.1038/nature08031

Schuur, Edward. A. G., McGuire, A. D., Romanovsky, V. E., Schädel, C., & Mack, M. C. (2018). Arctic and boreal carbon. In N. Cavallaro, G. Shrestha, R. Birdsey, M. A. Mayes, R. G. Najjar, S. C. Reed, P. Romero-Lankao, & Z. Zhu (Eds.), *Second State of the Carbon Cycle Report (SOCCR2): A Sustained Assessment Report* (pp. 428–468). U.S. Global Change Research Program. https://doi.org/10.7930/ SOCCR2.2018.Ch11

Shaver, G. R., Billings, W. D., Chapin, F. S., Giblin, A. E., Nadelhoffer, K. J., Oechel, W. C., & Rastetter, E. B. (1992). Global Change and the Carbon Balance of Arctic Ecosystems. *BioScience*, *42*(6), 433–441. https://doi.org/10.2307/1311862

Shaver, G. R., Canadell, J., Chapin, F. S., Gurevitch, J., Harte, J., Henry, G., Ineson, P., Jonasson, S., Melillo, J., Pitelka, L., & Rustad, L. (2000). Global Warming and Terrestrial Ecosystems: A Conceptual Framework for Analysis. *BioScience*, *50*(10), 871. https://doi.org/10.1641/0006-3568(2000)050[0871:GWATEA]2.0.CO;2

Shiklomanov, N. I., Streletskiy, D. A., Little, J. D., & Nelson, F. E. (2013). Isotropic thaw subsidence in undisturbed permafrost landscapes. *Geophysical Research Letters*, *40*(24), 6356–6361. https://doi.org/10.1002/2013GL058295

Shiklomanov, N. I., Streletskiy, D. A., & Nelson, F. E. (2012). Northern Hemisphere Component of the Global Circumpolar Active Layer Monitoring (CALM) Program. *Proceedings of the Tenth International Conference on Permafrost*, *1*, 377–382.

Shur, Y. L., & Jorgenson, M. T. (2007). Patterns of permafrost formation and degradation in relation to climate and ecosystems. *Permafrost and Periglacial Processes*, *18*(1), 7–19. https://doi.org/10.1002/ppp.582

Song, C., Xu, X., Sun, X., Tian, H., Sun, L., Miao, Y., Wang, X., & Guo, Y. (2012). Large methane emission upon spring thaw from natural wetlands in the northern permafrost region. *Environmental Research Letters*, *7*(3), 034009. https://doi.org/10.1088/1748-9326/7/3/034009

Streletskiy, D. A., Shiklomanov, N. I., Little, J. D., Nelson, F. E., Brown, J., Nyland, K. E., & Klene, A. E. (2017). Thaw Subsidence in Undisturbed Tundra Landscapes, Barrow,

Alaska, 1962-2015: Barrow Subsidence. *Permafrost and Periglacial Processes*, *28*(3), 566–572. https://doi.org/10.1002/ppp.1918

Streletskiy, D. A., Shiklomanov, N. I., Nelson, F. E., & Klene, A. E. (2008). *Thirteen years of observations at Alaskan CALM sites: Long-term active layer and ground surface temperature trends*. 6.

Subin, Z. M., Koven, C. D., Riley, W. J., Torn, M. S., Lawrence, D. M., & Swenson, S. C. (2013). Effects of Soil Moisture on the Responses of Soil Temperatures to Climate Change in Cold Regions. *JOURNAL OF CLIMATE*, *26*, 21.

Swanson, D. K. (2021). Permafrost thaw-related slope failures in Alaska's Arctic National Parks, *c*. 1980–2019. *Permafrost and Periglacial Processes*, ppp.2098. https://doi.org/10.1002/ppp.2098

Tagesson, T., Mölder, M., Mastepanov, M., Sigsgaard, C., Tamstorf, M. P., Lund, M., Falk, J. M., Lindroth, A., Christensen, T. R., & Ström, L. (2012). Land-atmosphere exchange of methane from soil thawing to soil freezing in a high-Arctic wet tundra ecosystem. *Global Change Biology*, *18*(6), 1928–1940. https://doi.org/10.1111/j.1365-2486.2012.02647.x

Tarnocai, C., Canadell, J. G., Schuur, E. A. G., Kuhry, P., Mazhitova, G., & Zimov, S. (2009). Soil organic carbon pools in the northern circumpolar permafrost region: SOIL ORGANIC CARBON POOLS. *Global Biogeochemical Cycles*, *23*(2), n/a-n/a. https://doi.org/10.1029/2008GB003327

Taylor, M. A., Celis, G., Ledman, J. D., Bracho, R., & Schuur, E. A. G. (2018). Methane efflux measured by eddy covariance in Alaskan upland tundra undergoing permafrost degradation. *Journal of Geophysical Research: Biogeosciences*, *123*(9), 2695–2710. https://doi.org/10.1029/2018JG004444

Taylor, M., Celis, G., Ledman, J., Mauritz, M., Natali, S. M., Pegoraro, E., Schädel, C., & Schuur, E. A. G. (2021). Experimental soil warming and permafrost thaw increase CH_4 emissions in an upland tundra ecosystem. *JGR Biogeosciences*.

Teufel, B., & Sushama, L. (2019). Abrupt changes across the Arctic permafrost region endanger northern development. *Nature Climate Change*, *9*(11), 858–862. https://doi.org/10.1038/s41558-019-0614-6

Thorson, R. M. (1986). Late Cenozoic glaciation of the Northern Nenana Valley. In T. D. Hamilton, K. M. Reed, & R. M. Thorson (Eds.), *Glaciation in Alaska* (pp. 99–121). Alaska Geological Society.

Tokida, T., Mizoguchi, M., Miyazaki, T., Kagemoto, A., Nagata, O., & Hatano, R. (2007). Episodic release of methane bubbles from peatland during spring thaw. *Chemosphere*, *70*(2), 165–171. https://doi.org/10.1016/j.chemosphere.2007.06.042

Trucco, C., Schuur, E. A. G., Natali, S. M., Belshe, E. F., Bracho, R., & Vogel, J. (2012). Seven-year trends of CO_2 exchange in a tundra ecosystem affected by long-term permafrost thaw. *Journal of Geophysical Research: Biogeosciences*, *117*(G2), n/a-n/a. https://doi.org/10.1029/2011JG001907

Turetsky, M. R., Abbott, B. W., Jones, M. C., Anthony, K. W., Olefeldt, D., Schuur, E. A. G.,

Grosse, G., Kuhry, P., Hugelius, G., Koven, C., Lawrence, D. M., Gibson, C., Sannel, A. B. K., & McGuire, A. D. (2020). Carbon release through abrupt permafrost thaw. *Nature Geoscience*, *13*(2), 138–143. https://doi.org/10.1038/s41561-019-0526-0

Veremeeva, A., Nitze, I., Günther, F., Grosse, G., & Rivkina, E. (2021). Geomorphological and climatic drivers of thermokarst lake area increase trend (1999–2018) in the Kolyma Lowland Yedoma Region, North-Eastern Siberia. *Remote Sensing*, *13*(2), 178. https://doi.org/10.3390/rs13020178

Vogel, J., Schuur, E. A. G., Trucco, C., & Lee, H. (2009). Response of CO_2 exchange in a tussock tundra ecosystem to permafrost thaw and thermokarst development. *Journal of Geophysical Research*, *114*(G4), G04018. https://doi.org/10.1029/2008JG000901

Walter Anthony, K., Daanen, R., Anthony, P., Schneider von Deimling, T., Ping, C.-L., Chanton, J. P., & Grosse, G. (2016). Methane emissions proportional to permafrost carbon thawed in Arctic lakes since the 1950s. *Nature Geoscience*, *9*(9), 679–682. https://doi.org/10.1038/ngeo2795

Walvoord, M. A., & Kurylyk, B. L. (2016). Hydrologic Impacts of Thawing Permafrost-A Review. *Vadose Zone Journal*, *15*(6), vzj2016.01.0010. https://doi.org/10.2136/vzj2016.01.0010

Ward Jones, M. K., Pollard, W. H., & Jones, B. M. (2019). Rapid initialization of retrogressive thaw slumps in the Canadian high Arctic and their response to climate and terrain factors. *Environmental Research Letters*, *14*(5), 055006. https://doi.org/10.1088/1748-9326/ab12fd

Watts, J. D., Natali, S. M., Minions, C., Risk, D., Arndt, K., Zona, D., Euskirchen, E. S., Rocha, A. V., Sonnentag, O., Helbig, M., Kalhori, A., Oechel, W., Ikawa, H., Ueyama, M., Suzuki, R., Kobayashi, H., Celis, G., Schuur, E. A. G., Humphreys, E., … Edgar, C. (2021). Soil respiration strongly offsets carbon uptake in Alaska and Northwest Canada. *Environmental Research Letters*, *16*(8), 084051. https://doi.org/10.1088/1748-9326/ac1222

Webb, E. E., Schuur, E. A. G., Natali, S. M., Oken, K. L., Bracho, R., Krapek, J. P., Risk, D., & Nickerson, N. R. (2016). Increased wintertime CO_2 loss as a result of sustained tundra warming: Tundra Wintertime CO_2 Loss. *Journal of Geophysical Research: Biogeosciences*, *121*(2), 249–265. https://doi.org/10.1002/2014JG002795

Westermann, S., Duguay, C., Grosse, G., & Kääb, A. (2015). Remote sensing of permafrost and frozen ground. In M. Tedesco (Ed.), *Remote Sensing of the Cryosphere* (First Edition, pp. 307–344). John Wiley & Sons, Ltd.

Wickham, H. (2017). *tidyverse: Easily install and load the "Tidyverse"* (1.2.1) [R]. https://CRAN.R-project.org/package=tidyverse

Wickham, H., Averick, M., Bryan, J., Chang, W., McGowan, L., François, R., Grolemund, G., Hayes, A., Henry, L., Hester, J., Kuhn, M., Pedersen, T., Miller, E., Bache, S., Müller, K., Ooms, J., Robinson, D., Seidel, D., Spinu, V., … Yutani, H. (2019). Welcome to the Tidyverse. *Journal of Open Source Software*, *4*(43), 1686. https://doi.org/10.21105/joss.01686

Wickland, K. P., Jorgenson, M. T., Koch, J. C., Kanevskiy, M., & Striegl, R. G. (2020). Carbon dioxide and methane flux in a dynamic Arctic tundra landscape: Decadal-scale impacts of ice wedge degradation and stabilization. *Geophysical Research Letters*, *47*(22). https://doi.org/10.1029/2020GL089894

Wu, H., & Li, Z.-L. (2009). Scale issues in remote sensing: A review on analysis, processing and modeling. *Sensors*, *9*(3), 1768–1793. https://doi.org/10.3390/s90301768

Wutzler, T., Lucas-Moffat, A., Migliavacca, M., Knauer, J., Sickel, K., Šigut, L., Menzer, O., & Reichstein, M. (2018). Basic and extensible post-processing of eddy covariance flux data with REddyProc. *Biogeosciences*, *15*(16), 5015–5030. https://doi.org/10.5194/bg-15-5015-2018

Zimov, S. A., Davydov, S. P., Zimova, G. M., Davydova, A. I., Schuur, E. A. G., Dutta, K., & Chapin, F. S. (2006). Permafrost carbon: Stock and decomposability of a globally significant carbon pool. *Geophysical Research Letters*, *33*(20), L20502. https://doi.org/10.1029/2006GL027484

Zona, D., Gioli, B., Commane, R., Lindaas, J., Wofsy, S. C., Miller, C. E., Dinardo, S. J., Dengel, S., Sweeney, C., Karion, A., Chang, R. Y.-W., Henderson, J. M., Murphy, P. C., Goodrich, J. P., Moreaux, V., Liljedahl, A., Watts, J. D., Kimball, J. S., Lipson, D. A., & Oechel, W. C. (2016). Cold season emissions dominate the Arctic tundra methane budget. *Proceedings of the National Academy of Sciences*, *113*(1), 40–45. https://doi.org/10.1073/pnas.1516017113

SUPPLEMENTAL INFORMATION FOR CHAPTER 2

Text S2.1.

To partition the total ice volume into excess and pore ice components, we started with an equation for the total core volume using its component parts:

$$TotalCoreVolume(m^3) = TotalIceVolume(m^3) + SoilVolume(m^3) - PoreIceVolume(m^3) \quad \text{Eq. S2.1}$$

where the known total core volume is calculated from the soil core dimensions and the known total ice volume is calculated by multiplying the total ice mass by the density of ice. The variables soil volume and pore ice volume are unknowns and soil volume refers to the volume of dry soil, including pore space. To be able to solve for soil volume, we replaced the unknown variable, pore ice volume, by assuming that pore space composes 50% of the soil volume (Brady & Weil, 2008; Figure S3):

$$TotalCoreVolume(m^3) - TotalIceVolume(m^3) = SoilVolume(m^3) - 0.5 * SoilVolume(m^3) \quad \text{Eq. S2.2}$$

We then rearranged equation S2 to calculate the soil volume, including pore space:

$$SoilVolume(m^3) = 2 * \left(TotalCoreVolume(m^3) - TotalIceVolume(m^3)\right) \quad \text{Eq. S2.3}$$

Finally, excess ice was calculated from the known soil core volume and calculated soil volume, including pore space, from Eq. S2:

$$ExcessIce(m^3) = TotalCoreVolume(m^3) - SoilVolume(m^3) \quad \text{Eq. S2.4}$$

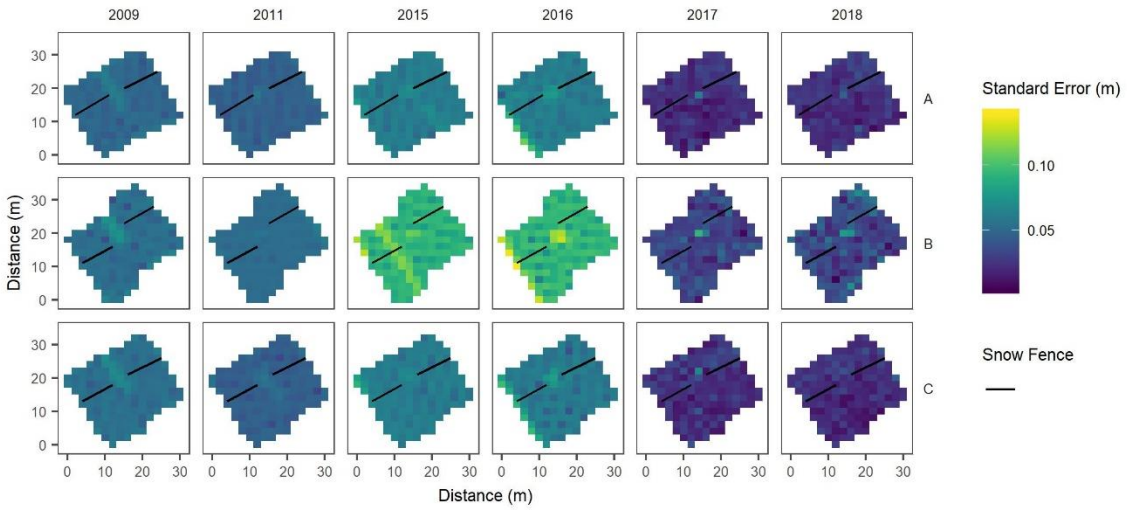

Figure S2.1. Standard error of the kriged elevation surfaces.

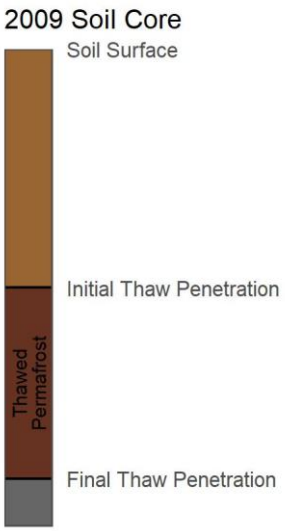

Figure S2.2. A diagram of a soil core showing the thawed permafrost, which we defined as the layer of soil between the initial (2009) thaw penetration and the final (any year through 2018) thaw penetration. The calculation of both the minimum and maximum potential subsidence uses ice volume from within the thawed permafrost layer only.

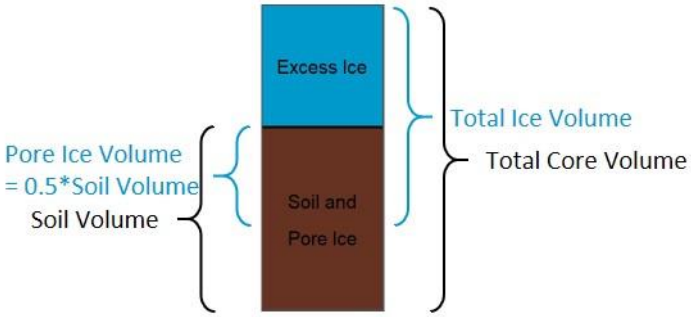

Figure S2.3. A diagram of the relative volumes of total ice, excess ice, pore ice, and soil within soil cores. Soil volume and pore ice volume were both unknowns, while total ice volume and total core volume were measured in the laboratory. Soil volume refers to the combined volume of

soil and pore space. Given the total ice volume, total core volume, and the estimated relationship between soil volume and pore ice volume, we were able to solve for soil volume.

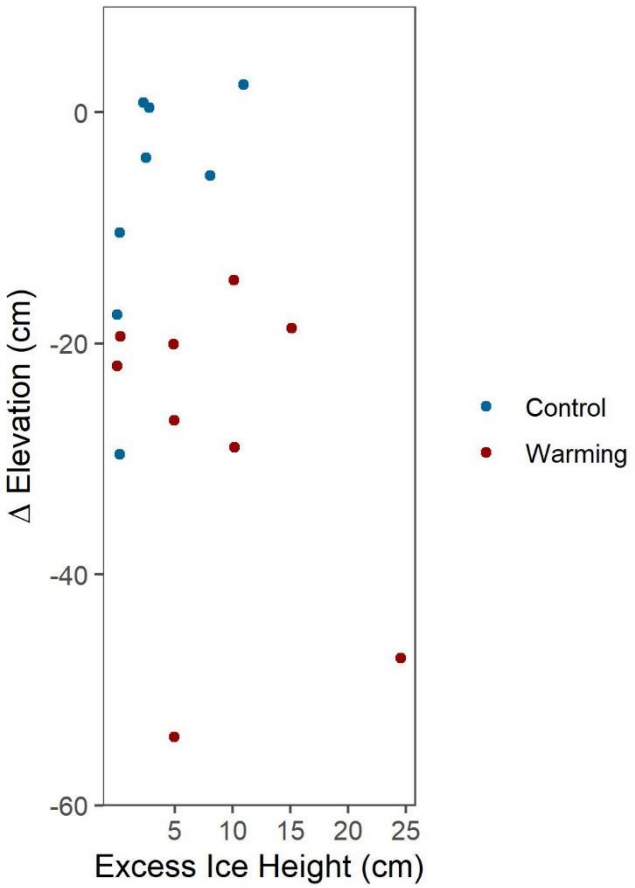

Figure S2.4. The relationship between excess ice height and subsidence. A mixed effects model showed that there was no correlation.

Table S2.1. Mixed effects model results for the effect of warming on subsidence through time. No intercept was included for any treatment, as subsidence in the first year of measurements was necessarily 0. Filename: 2019JG005528R-Table S1.xlsx

Table S2.2. Soil core data and calculated ice height (volume of ice/soil core area) for each soil layer in each soil core from 2009. The layer height is the depth from the initial thaw penetration

to the final thaw penetration. Gravimetric water content and bulk density are depth normalized averages from the originally measured soil layers (5-10 cm sections). Ice height is calculated using the equation in section 3.4, and the cumulative ice height is the sum of ice heights for each core (unique combination of block, fence, and treatment; shown with blocks of shading). NA indicates missing data, because the soil core was not deep enough to reach the final thaw penetration. Filename: 2019JG005528R-Table S2.xlsx

Table S2.3. Results of a mixed effects model of subsidence with the fixed effects of total ice height and soil warming, where ice height is calculated as the total volume of ice within the thawed permafrost soil layer divided by the area of the soil core. Filename: 2019JG005528R-Table S3.xlsx

Movie S2.1. 3D gif of elevation at Block A through time. File available at https://agupubs.onlinelibrary.wiley.com/doi/full/10.1029/2019JG005528. Filename: 2019JG005528R-Movie S1.gif

Movie S2.2. 3D gif of elevation at Block B through time. File available at https://agupubs.onlinelibrary.wiley.com/doi/full/10.1029/2019JG005528. Filename: 2019JG005528R-Movie S2.gif

Movie S2.3. 3D gif of elevation at Block C through time. File available at https://agupubs.onlinelibrary.wiley.com/doi/full/10.1029/2019JG005528. Filename: 2019JG005528R-Movie S3.gif

SUPPLEMENTAL INFORMATION FOR CHAPTER 3

Table S1. A description of the thermokarst models we tested. Neighborhood size indicates the radius of the circular neighborhood used to calculate median elevation and cut-off indicates the cut-off used to classify microtopography as thermokarst.

Model Name	Neighborhood Size (radius in m)	Threshold (cm)	Overall Accuracy (%)
Small	15	0	69
Conservative Small	15	-5	61.5
Medium	25	0	68
Large	35	0	67.5
Small Combination	**15 & 25**	**0**	**71.5**
Large Combination	25 & 35	0	68
Complete Combination	**15 & 25 & 35**	**0**	**71.5**
Conservative Small and Large Combination	15 & 25 & 35	-5 (15m) and 0 (25m & 35m)	69

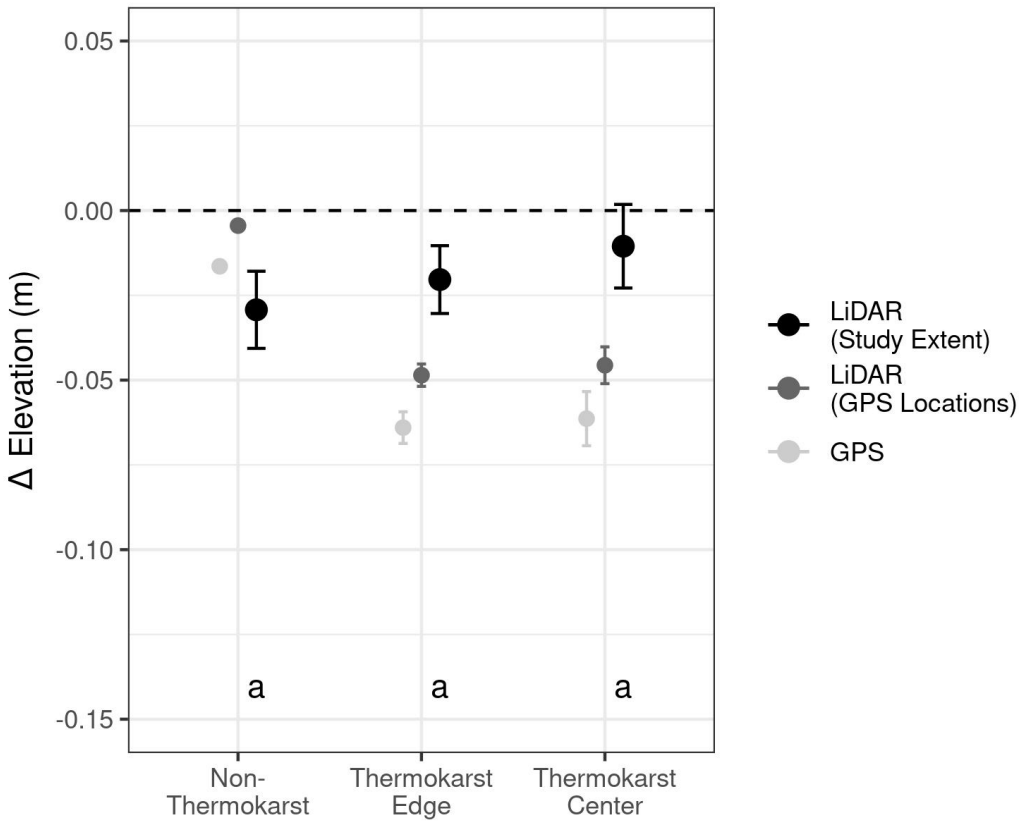

Figure S1. Subsidence between 2017 and 2019 by thermokarst class. In black, LiDAR (Study Extent) shows subsidence calculated from the LiDAR DTM from a stratified random sample of cells (~500 cells from each class) across the study extent. To evaluate the performance of the LiDAR-derived subsidence, we also included a comparison of LiDAR and GPS derived subsidence across all locations with GPS data. GPS shows subsidence calculated from the GPS-derived DTM within CiPEHR (n = Non-Thermokarst: 1094, Thermokarst Edge: 163, Thermokarst Center: 64) and LiDAR (GPS Locations) shows subsidence calculated from the LiDAR DTM within the footprint of the GPS-derived DTM at CiPEHR (same sample size as GPS). Error bars show the standard error. Letters indicate (the lack of) differences in rate of subsidence between thermokarst classes using LiDAR across the entire study extent.

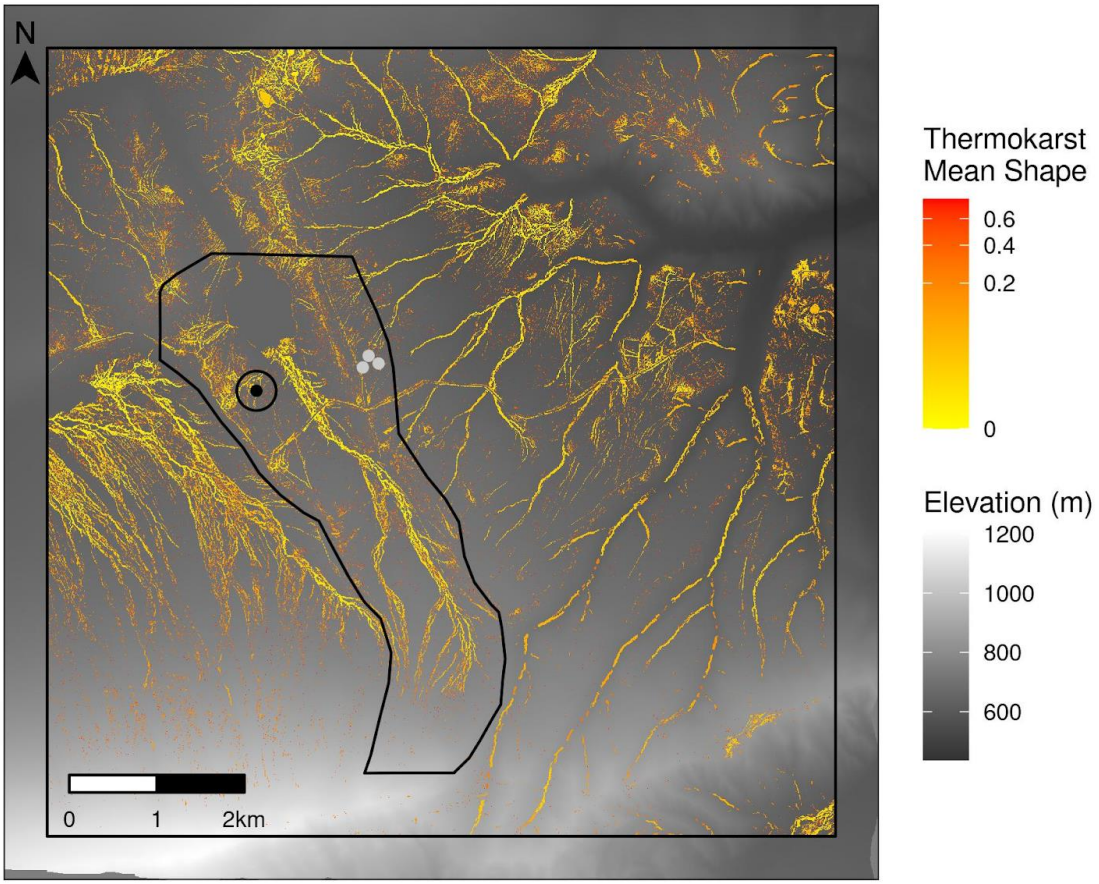

Figure S2. The mean shape of thermokarst features (2017-2019) across the study extent (9 x 9 km black box). The Polsby-Popper test was used to determine the shape of thermokarst features, with smaller values being rounder or more compact and larger values being longer or less compact. Thermokarst features with smaller Polsby-Popper values tend to be water tracks, while features with larger values tend to be small thermokarst pits. The EML watershed is outlined in black with the EC tower and approximate tower footprint shown as a point within a circle. The three gray points show the location of the three experimental blocks at CiPEHR.

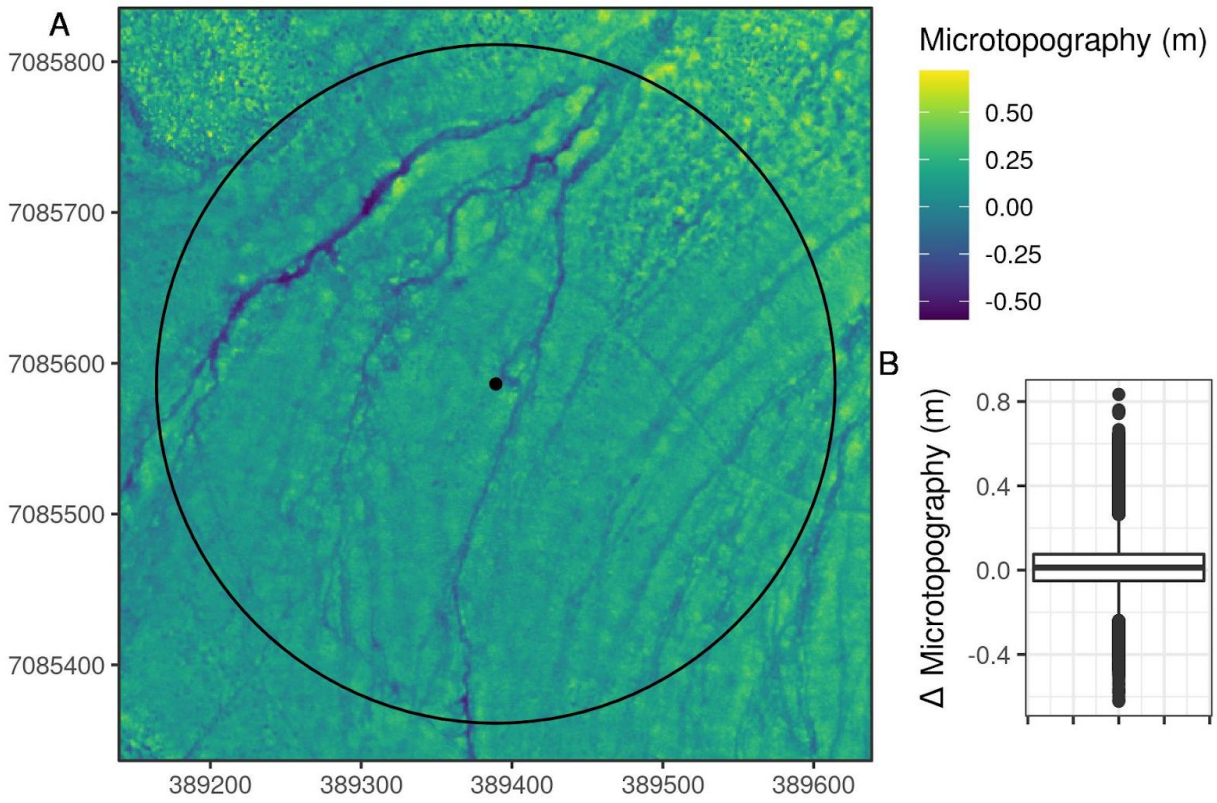

Figure S3. A) Mean microtopography for the period 2017-2019 at the EC tower (black point), with the approximate EC tower footprint delineated (black circle). One deeply incised water track with two forks to the NW of the EC tower and one fork immediately to the right of the EC tower is found at the site. B) Change in microtopography between 2008 and the mean of 2017-2019.

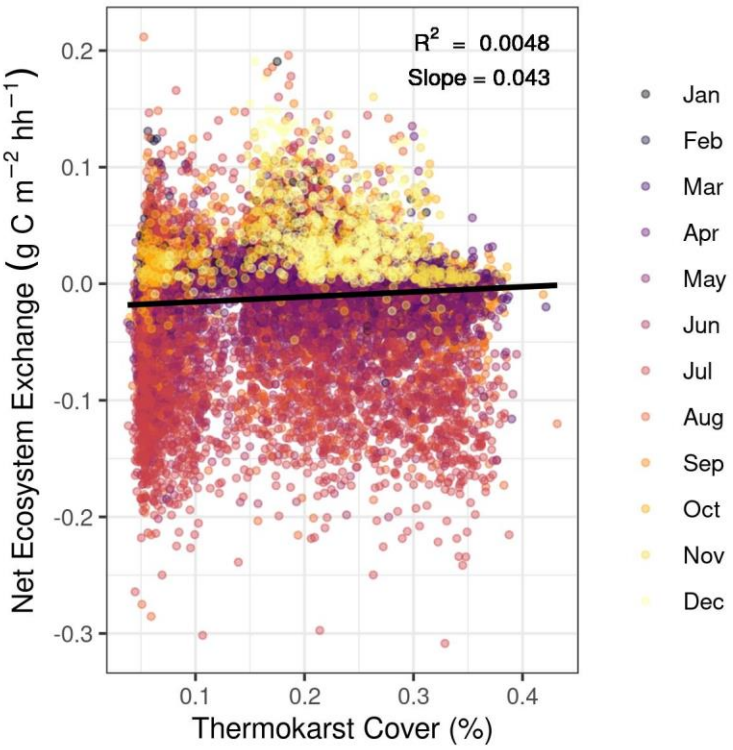

Figure S4. A scatterplot of NEE (all times) by thermokarst percent cover with the linear fit.

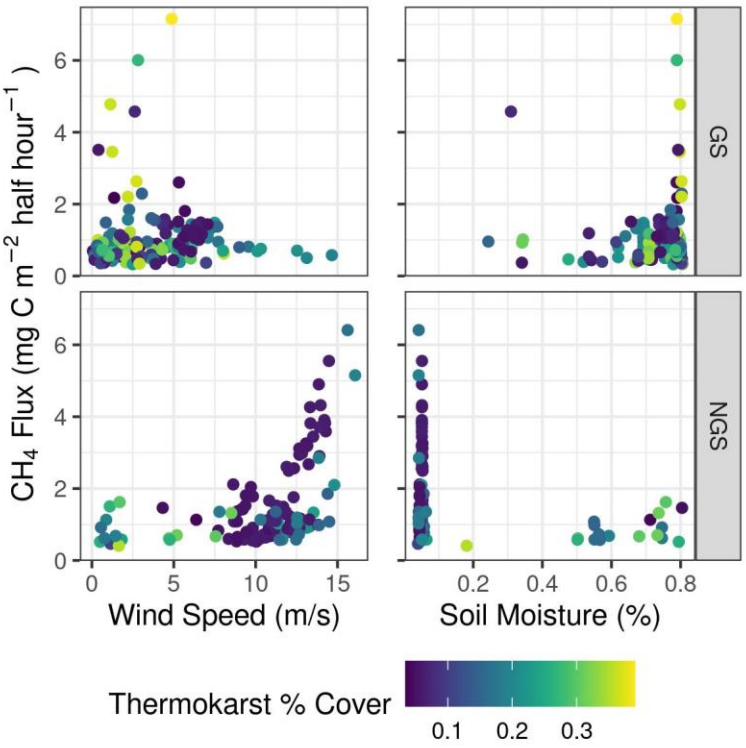

Figure S5. Relationship of CH_4 pulse release (CH_4 fluxes more than 3 standard deviations from the 2-week mean which were not included in linear modeling) to wind speed and soil moisture in the GS and NGS, with points colored by thermokarst percent cover.

SUPPLEMENTAL INFORMATION FOR CHAPTER 4

Analysis of the Impact of Subsidence on Hydrology:

To determine the effect of subsidence on soil hydrologic conditions throughout the course of the experiment, we modeled the plot-level response of GS mean and standard deviation of WTD (water table), VWC (0-15cm soil moisture), and GWC (0-5cm surface moisture) to subsidence using mixed effects models in the lme4 package (Bates et al., 2015). We included plot nested within treatment nested within snow fence nested within block as a random effect to account for the experimental design. To find the best fitting model, we considered models with 1) no fixed effects (null model), 2) subsidence, and 3) a quadratic subsidence effect. A quadratic term was tested to account for expected diminishing responses of hydrologic variables as subsidence proceeded and the inability of VWC and GWC to exceed 100%. Variable selection was performed using forward step-wise selection using AIC. Confidence intervals for fixed effects were bootstrapped with 1000 iterations using the MASS package and r^2 values were estimated using the MuMIn package (Bartoń, 2020). All variables were inspected for normality and an appropriate transformation was performed where necessary.

To investigate the intra-annual and spatial variability of the impact of subsidence on soil hydrologic conditions across plots for the entire experiment, we determined elevation, TD, and WTD along a transect spanning control and soil warming plots at each fence. Because each of these environmental variables were measured in slightly different locations across the experimental blocks, we used the kriged elevation (2.2.), and interpolated TD and WTD using universal kriging (incorporating the relationship between TD or WTD and subsidence) to get continuous surfaces from point measurements using the automap package (Hiemstra et al., 2009). Values from each layer were extracted along the transects using the raster package

(Hijmans, 2021). TD and WTD values were extracted both during a dry period and also following a large precipitation event; we selected dates that were about two weeks apart in 2018, because 2018 was the most recent year with both elevation data and a significant dry period. We used TD measured on July 27, 2018 (dry) and Aug. 10, 2018 (wet) and WTD measured on July 30, 2018 (dry) and Aug. 8, 2018 (wet). Because TD and WTD were not measured on exactly the same days, we chose dates that were as close in time as possible for comparison between TD and WTD (<= 3 days between measurements) while still falling within the window of dry and wet conditions. Elevation values were extracted only once, as the changes in elevation were negligible within the two week period.

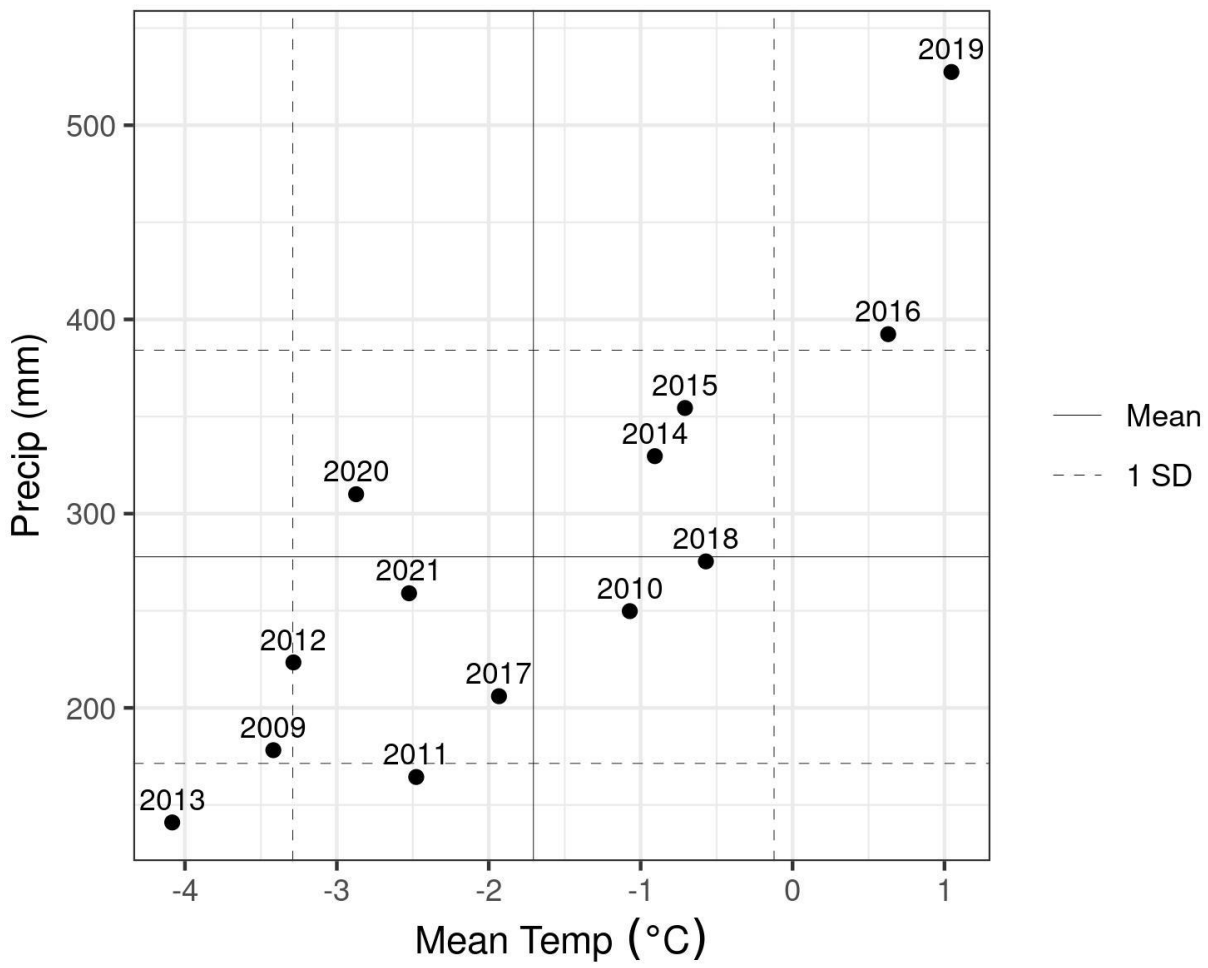

Figure S1. The spread of annual temperature and precipitation conditions throughout the course of the warming experiment. Mean annual temperature was calculated from Oct. 1 (of the previous year) - Sept. 30 (of the year as labeled), while precipitation was calculated for the GS, defined as May 1 - Sept. 30 (of the year as labeled). Mean and 1 SD lines were calculated across all years.

Table S1. GS, NGS, and annual meteorological conditions at CiPEHR. Snow depth and snow free date are provided by treatment, as this varies among plots, while all other variables are provided at the site level only.

Measurement	Season	2009	2010	2011	2012	2013	2014	2015	2016	2017	2018	2019	2020	2021
Mean Air Temperature (°C)	Annual	-3.42	-1.07	-2.48	-3.29	-4.08	-0.91	-0.71	0.63	-1.93	-0.57	1.05	-2.87	-2.52
	GS	9.71	9.84	9.42	9.14	9.27	9.14	9.52	10.29	10.42	9.66	10.82	9.83	9.05
	NGS	-12.92	-8.4	-11.07	-12.21	-13.72	-8.16	-8.09	-6.31	-10.85	-7.96	-6.01	-11.99	-10.88
Mean PAR (µmol m^{-2} s^{-1})	Annual	266.15	204.91	224.98	225.15	247.7	214.33	215.66	212.71	242.91	232.71	216.21	219.22	229.06
	GS	376.59	362.42	378.7	365.19	415.4	344.81	358.25	345.84	384.26	377.79	359.2	360.37	373.62
	NGS	140.91	71.59	114.04	124.55	126.67	120.16	112.75	117.09	140.9	128.01	113.01	117.83	124.74
Rainfall (mm)	Annual	178.2	249.8	164.4	223.4	141	329.6	354.4	392.4	206	275.4	527.4	310	259
	GS	178.2	249.8	164.4	223.4	111.6	312.2	354.4	392.4	187.2	275.4	518.4	293.2	257.6
	NGS	0	0	0	0	29.4	17.4	0	0	18.8	0	9	16.8	1.4
Treatment														
Spring Snow Depth (m)	Air + Soil Warming	1.35	0.49	1.08	1.29	1.24	0.79	0.92	1.13	1.22	1.55	1.03	1.32	1.56
	Air Warming	0.4	0.18	0.23	0.55	0.65	0.22	0	0.3	0.48	0.83	0.08	0.59	0.86
	Control	0.4	0.17	0.23	0.55	0.65	0.23	0	0.3	0.49	0.83	0.09	0.59	0.86
	Soil Warming	1.36	0.7	1.1	1.29	1.24	0.94	1.09	1.22	1.23	1.58	1.16	1.32	1.59
Snow Free Date (DOY)	Air + Soil Warming	NA	118	119	125	148	109	112	111	119	133	117	121	129
	Air Warming	NA	117	117	126	148	110	112	108	121	131	111	123	128
	Control	NA	117	117	125	148	110	112	108	121	131	111	125	128
	Soil Warming	NA	117	119	125	148	109	112	111	121	133	112	121	129

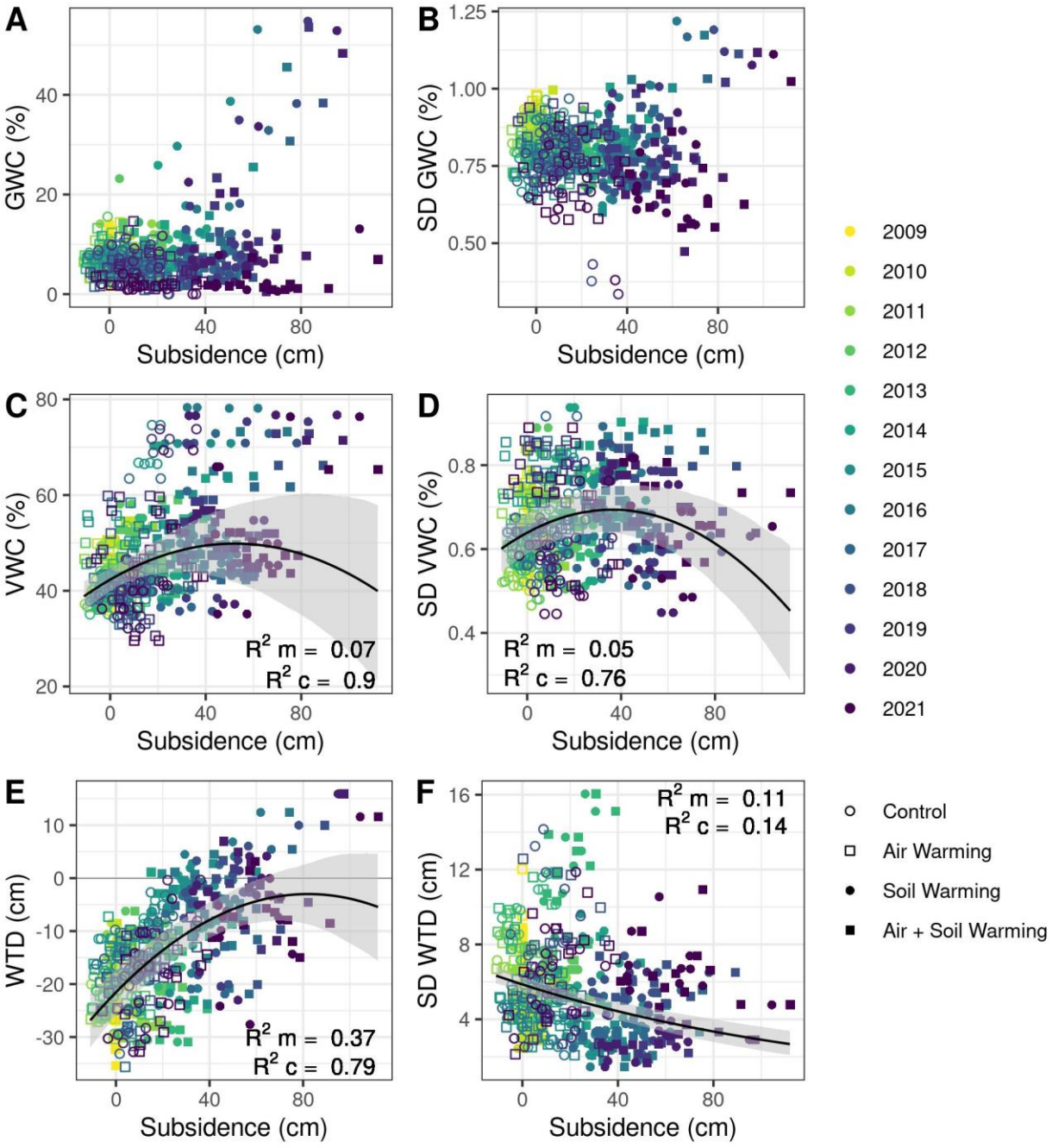

Figure S2. Mixed effects models of the role of subsidence in driving changes in A) GWC, B) SD GWC, C) VWC, D) SD VWC, E) WTD, and F) SD WTD. SD WTD was log-transformed and quadratic terms were statistically significant in the relationships with VWC, SD VWC, WTD, and SD WTD. Points reflect annual average values for a single plot, with color indicating year and shape indicating treatment. GWC measures soil moisture in the surface layer of moss and VWC measures soil moisture over the top 15 cm. In general subsidence resulted in wetter soils, with the relationship between subsidence and WTD being stronger than that with VWC or GWC.

Relationships between subsidence and the standard deviation of soil moisture metrics were much weaker, but showed that subsidence resulted in less variable soil hydrologic conditions in the two statistically significant relationships.

Table S2. Model summaries of the linear models of WTD, SD WTD, VWC, and SD VCW by subsidence. Marginal and conditional r^2 values are indicated by R^2_M and R^2_C, respectively.

Response	Final Variables	Coefficient	Min	Max	R^2M	R^2C
WTD	Intercept	-21.6	-25.8	-17.1	0.37	0.789
	Subsidence	0.451	0.362	0.541		
	Subsidence^2	-0.00275	-0.0038	-0.00171		
SD WTD	Intercept	1.77	1.7	1.83	0.107	0.144
	Subsidence	-0.00701	-0.00919	-0.00486		
VWC	Intercept	42.3	40	44.5	0.0694	0.898
	Subsidence	0.289	0.13	0.448		
	Subsidence^2	-0.00277	-0.00362	-0.00194		
SD VWC	Intercept	0.639	0.59	0.687	0.054	0.761
	Subsidence	0.00303	0.00188	0.00416		
	Subsidence^2	-0.0000419	-5.41E-05	-2.96E-05		

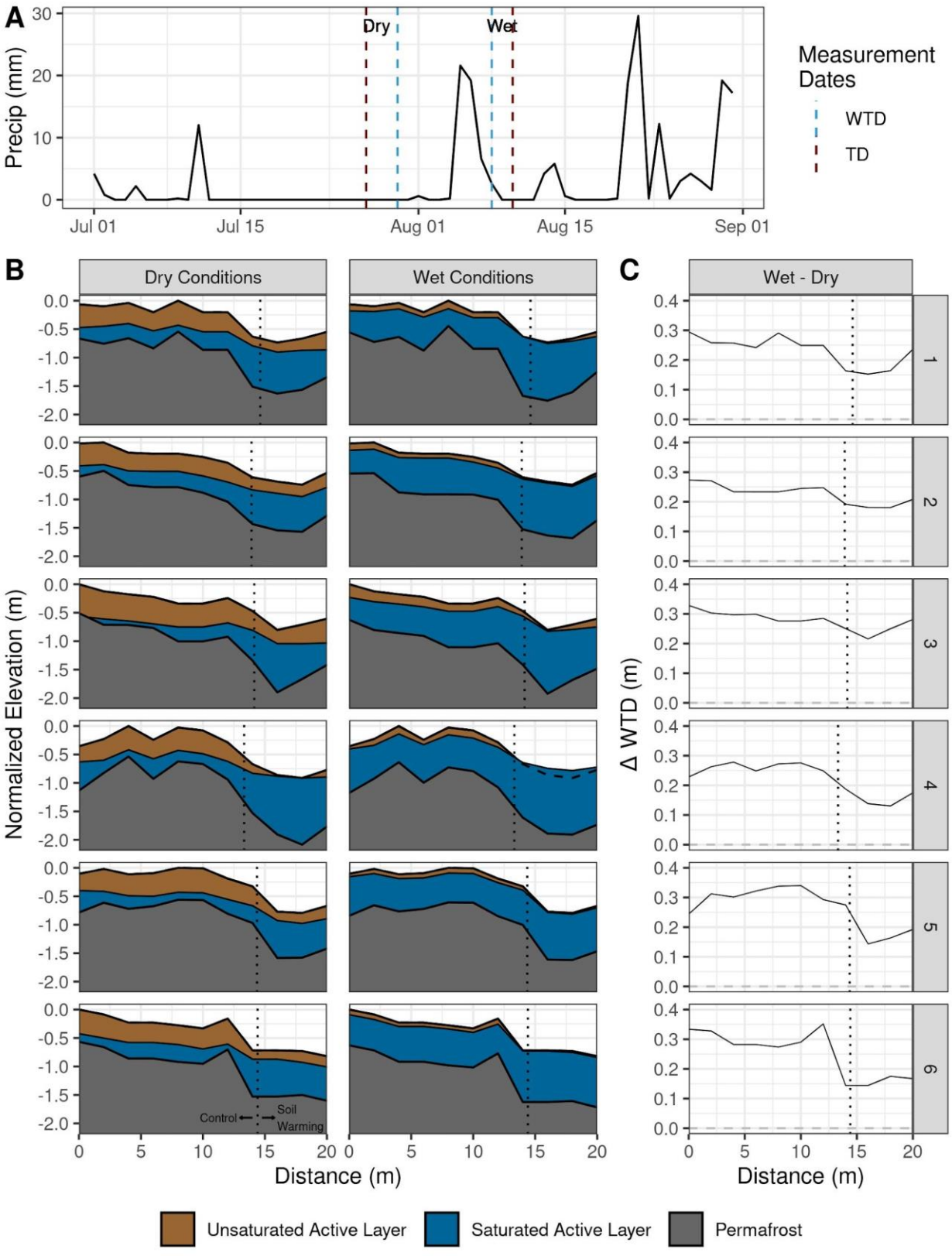
A
Precip (mm)
Dry
Wet
Measurement Dates
WTD
TD
Jul 01
Jul 15
Aug 01
Aug 15
Sep 01
B
Dry Conditions
Wet Conditions
Normalized Elevation (m)
Control
Soil Warming
Distance (m)
C
Wet - Dry
Δ WTD (m)
Distance (m)
Unsaturated Active Layer
Saturated Active Layer
Permafrost

Figure S3. A) July and August precipitation in 2018, with WTD and TD measurement dates marked for a period with dry conditions and a period with wet conditions. B) Elevation, thaw depth, and water table depth (WTD) along control-soil warming transects at each of the 6 replicate snow fences during dry conditions and wet conditions. Gray fill indicates frozen soil (some of which is permafrost and some of which is frozen active layer), blue fill indicates fully saturated soils in the active layer, and brown indicates unsaturated soils in the active layer. The location of the snow fence is indicated with the dotted line with the control side to the left and the soil warming side to the right. C) The difference in WTD before and after the precipitation event. WTD is near, at, or slightly above the soil surface in the thermokarst depressions in the soil warming treatment during both dry and wet conditions, while relatively high relief areas in the control have deeper WTD before the precipitation event and much shallower WTD after the precipitation event.

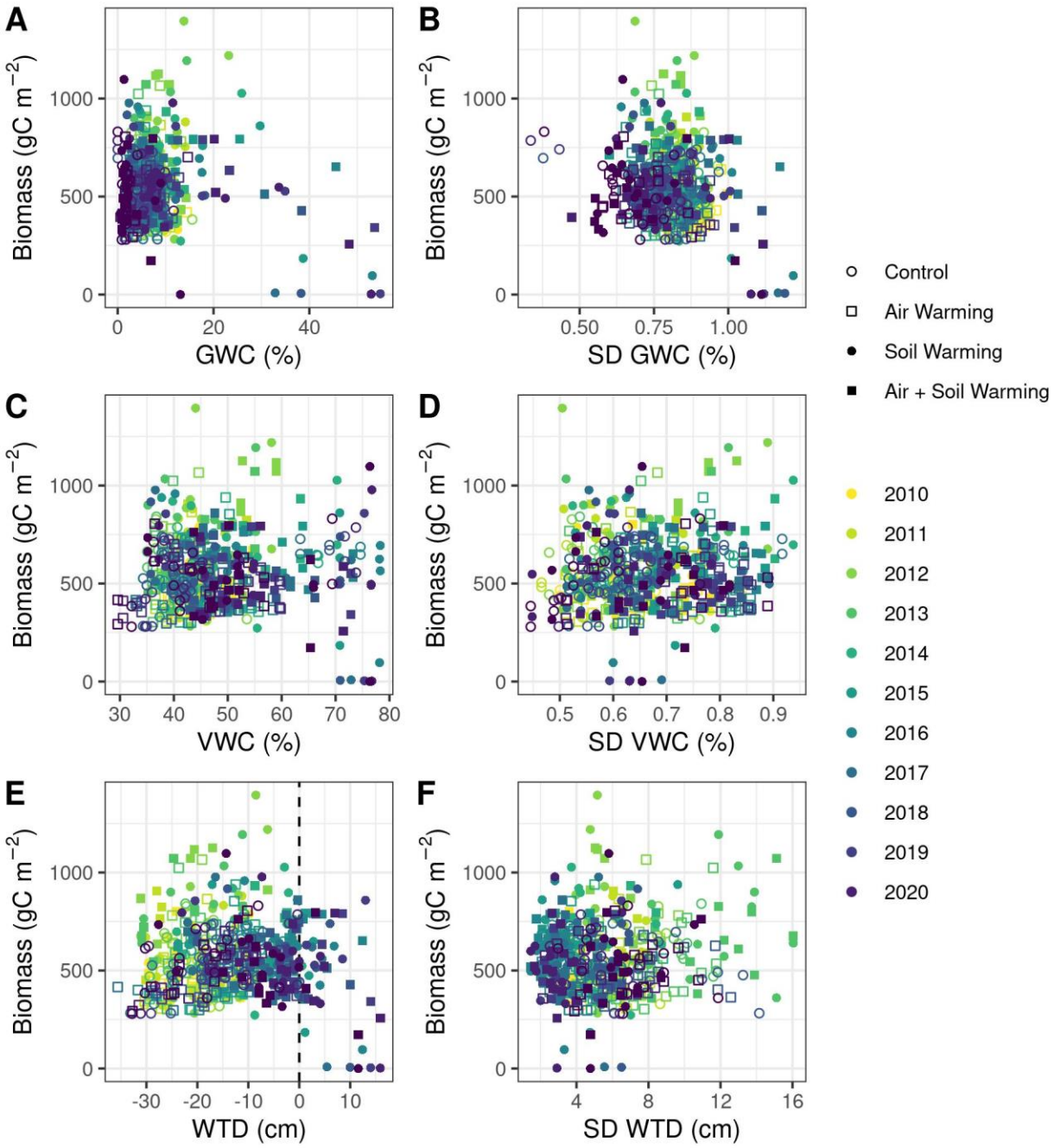

Figure S4. Scatterplots of AGB by A) GWC, B) SD GWC, C) VWC, D) SD VWC, E) WTD, and F) SD WTD. Points reflect annual average values for a single plot, with color indicating year and shape indicating treatment.

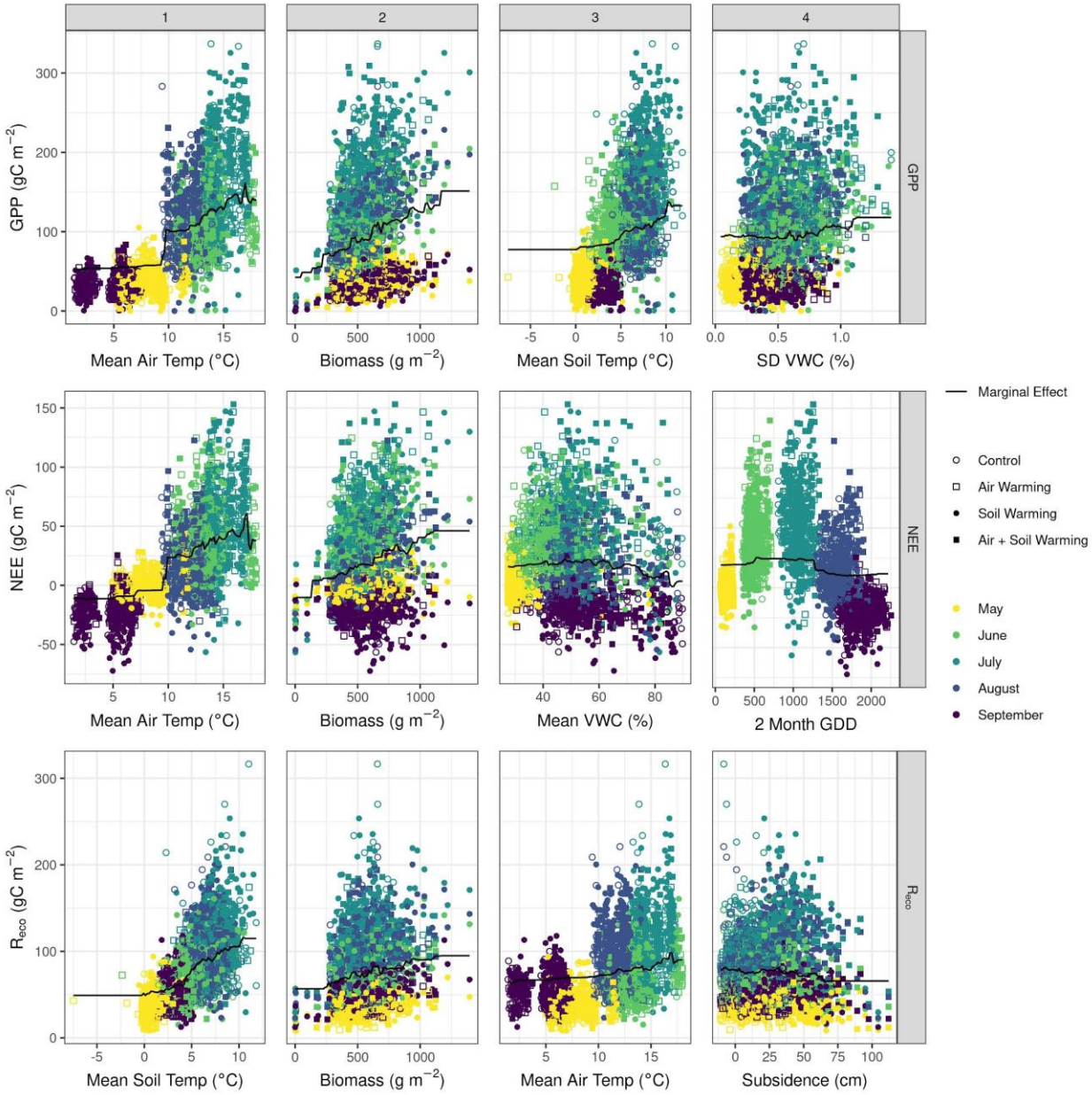

Figure S5. Partial dependence plots overlaid on measured data for the top four predictors of monthly GPP, NEE, and R_{eco} from the GBM. Labels 1 through 4 indicate the order of predictor importance. Each point represents an individual plot over one month of measurements. Color indicates month and shape indicates treatment.

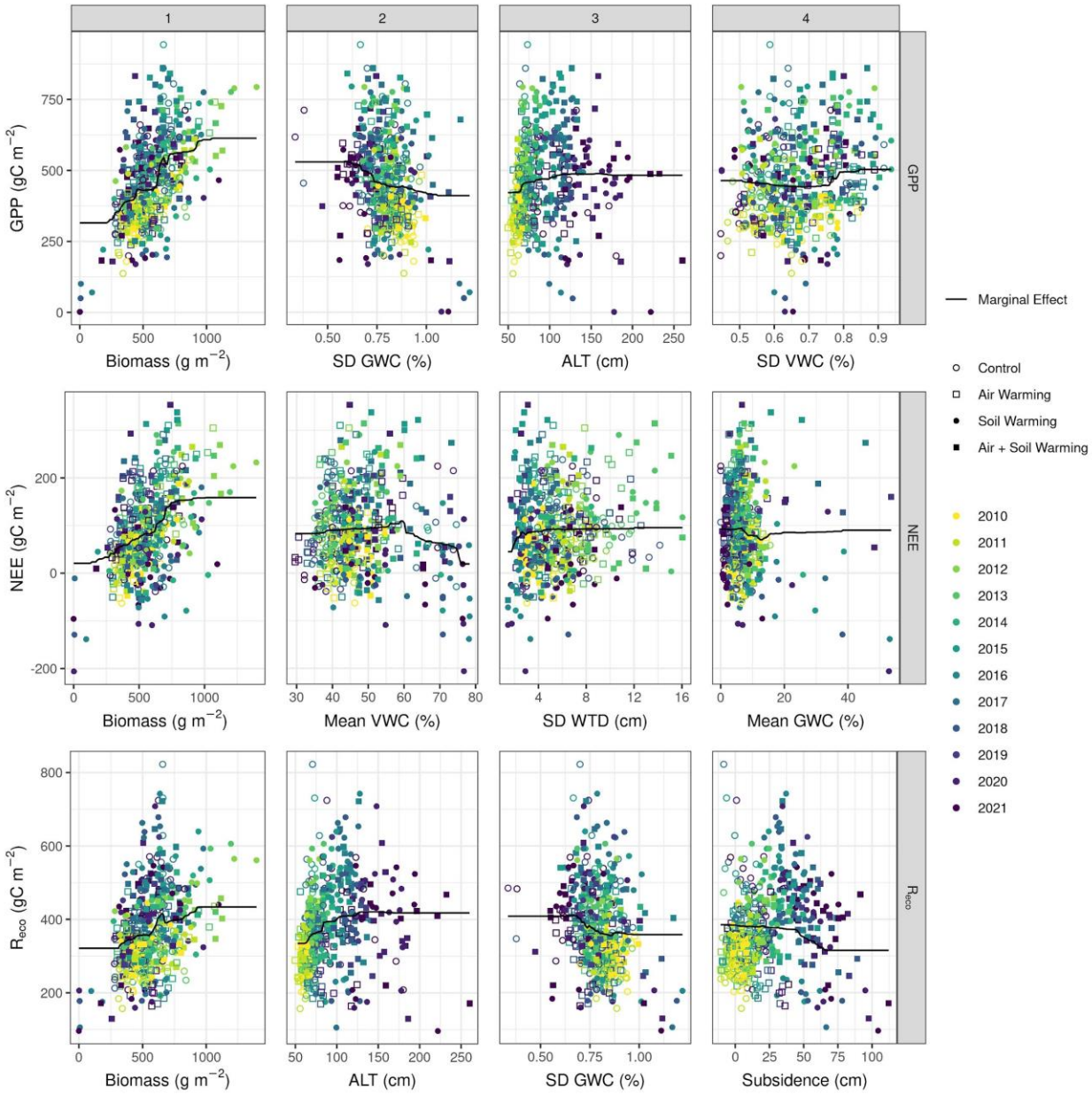

Figure S6. Partial dependence plots overlaid on measured data for the top four predictors of seasonal GPP, NEE, and R_{eco} from the GBM. Each point represents an individual plot over one month of measurements. Color indicates month and shape indicates treatment.

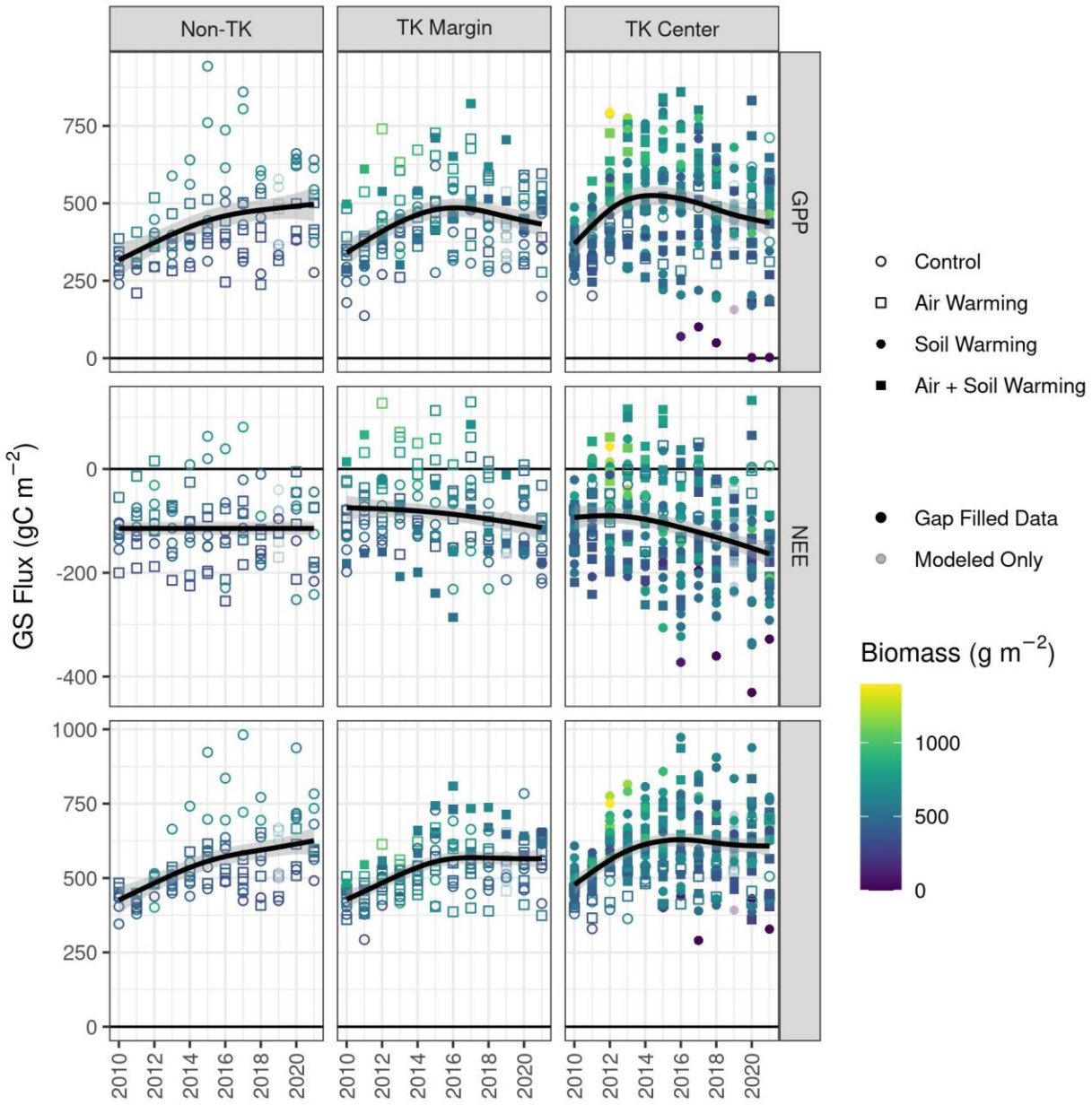

Figure S7. The trajectory of annual CO_2 fluxes throughout the course of the warming experiment in each of the thermokarst classes with generalized additive model (GAM) lines to highlight trends through time. Each plot was assigned to the same thermokarst class in all years based on the thermokarst class in 2021. Each point represents the annual cumulative CO_2 flux for an individual plot. Color indicates plot-level AGB and shape indicates experimental treatment. Solid points indicate GS sums of gap-filled measurements, and transparent points in 2019 indicate GS sums which were modeled using the monthly GBMs of each CO_2 flux and plot-level environmental conditions.

Table S3. GS, NGS, and annual cumulative NEE, R_{eco}, and GPP throughout the course of the permafrost warming experiment. GS values were calculated from gap-filled measurements. Winter NEE was estimated half-hourly using 5 cm soil temperature and the relationship between 5 cm soil temperature and winter NEE measured at an eddy covariance tower located approximately 1 km from the warming experiment. Each point represents the annual cumulative CO_2 flux for an individual plot. Color indicates plot-level AGB. In 2019, only a subset of plots were measured for CO_2 fluxes, so annual sums were gap filled using monthly GBM models of each CO_2 flux and plot-level environmental conditions.

		NEE			Reco			GPP		
Year	Treatment	GS	NGS	Annual	GS	NGS	Annual	GS	NGS	Annual
2009	Control	7	-165	-158	197	165	363	204	0	204
	Air Warming	13	-167	-154	234	167	401	247	0	247
	Soil Warming	-2	-188	-190	212	188	400	209	0	209
	Air + Soil Warming	2	-185	-183	239	185	424	241	0	241
2010	Control	23	-148	-125	267	148	415	290	0	290
	Air Warming	45	-145	-100	303	145	448	348	0	348
	Soil Warming	48	-167	-119	330	167	497	378	0	378
	Air + Soil Warming	47	-162	-115	311	162	473	357	0	357
2011	Control	49	-151	-102	235	151	386	283	0	283
	Air Warming	76	-149	-74	280	149	429	356	0	356
	Soil Warming	102	-184	-82	342	184	526	444	0	444
	Air + Soil Warming	93	-188	-95	302	188	490	395	0	395
2012	Control	76	-166	-90	301	166	467	377	0	377
	Air Warming	98	-164	-66	326	164	490	424	0	424
	Soil Warming	126	-197	-71	446	197	644	573	0	573
	Air + Soil Warming	113	-196	-83	384	196	580	497	0	497
2013	Control	98	-187	-89	299	187	486	397	0	397
	Air Warming	122	-187	-65	311	187	498	433	0	433
	Soil Warming	147	-201	-54	458	201	659	605	0	605
	Air + Soil Warming	129	-197	-68	364	197	561	493	0	493
2014	Control	105	-196	-91	339	196	535	445	0	445
	Air Warming	119	-200	-82	313	200	513	432	0	432
	Soil Warming	83	-219	-136	430	219	650	514	0	514
	Air + Soil Warming	109	-217	-108	411	217	628	521	0	521
2015	Control	104	-186	-82	408	186	594	512	0	512
	Air Warming	129	-190	-62	357	190	548	486	0	486
	Soil Warming	81	-220	-139	405	220	625	486	0	486
	Air + Soil Warming	163	-220	-57	424	220	644	588	0	588
2016	Control	84	-196	-113	415	196	611	502	0	502
	Air Warming	94	-196	-102	322	196	518	419	0	419
	Soil Warming	-4	-228	-232	455	228	683	455	0	455
	Air + Soil Warming	99	-227	-128	463	227	690	565	0	565
2017	Control	96	-163	-66	426	163	588	524	0	524
	Air Warming	126	-169	-43	343	169	512	471	0	471
	Soil Warming	48	-189	-141	465	189	654	516	0	516
	Air + Soil Warming	154	-190	-36	439	190	629	596	0	596
2018	Control	75	-212	-137	363	212	575	440	0	440
	Air Warming	125	-214	-89	308	214	522	435	0	435
	Soil Warming	19	-229	-210	412	229	641	433	0	433
	Air + Soil Warming	101	-229	-128	400	229	628	503	0	503
2019	Control	86	-189	-103	356	189	545	414	0	414
	Air Warming	64	-188	-124	348	188	536	419	0	419
	Soil Warming	63	-211	-148	413	211	624	454	0	454
	Air + Soil Warming	96	-211	-115	390	211	601	489	0	489
2020	Control	105	-202	-98	442	202	644	521	0	521
	Air Warming	147	-205	-58	323	205	527	446	0	446
	Soil Warming	2	-227	-224	403	227	630	399	0	399
	Air + Soil Warming	125	-227	-101	381	227	608	492	0	492
2021	Control	59	-211	-152	389	211	601	452	0	452
	Air Warming	96	-213	-117	363	213	576	463	0	463
	Soil Warming	0	-228	-227	394	228	622	400	0	400
	Air + Soil Warming	71	-224	-154	398	224	623	475	0	475

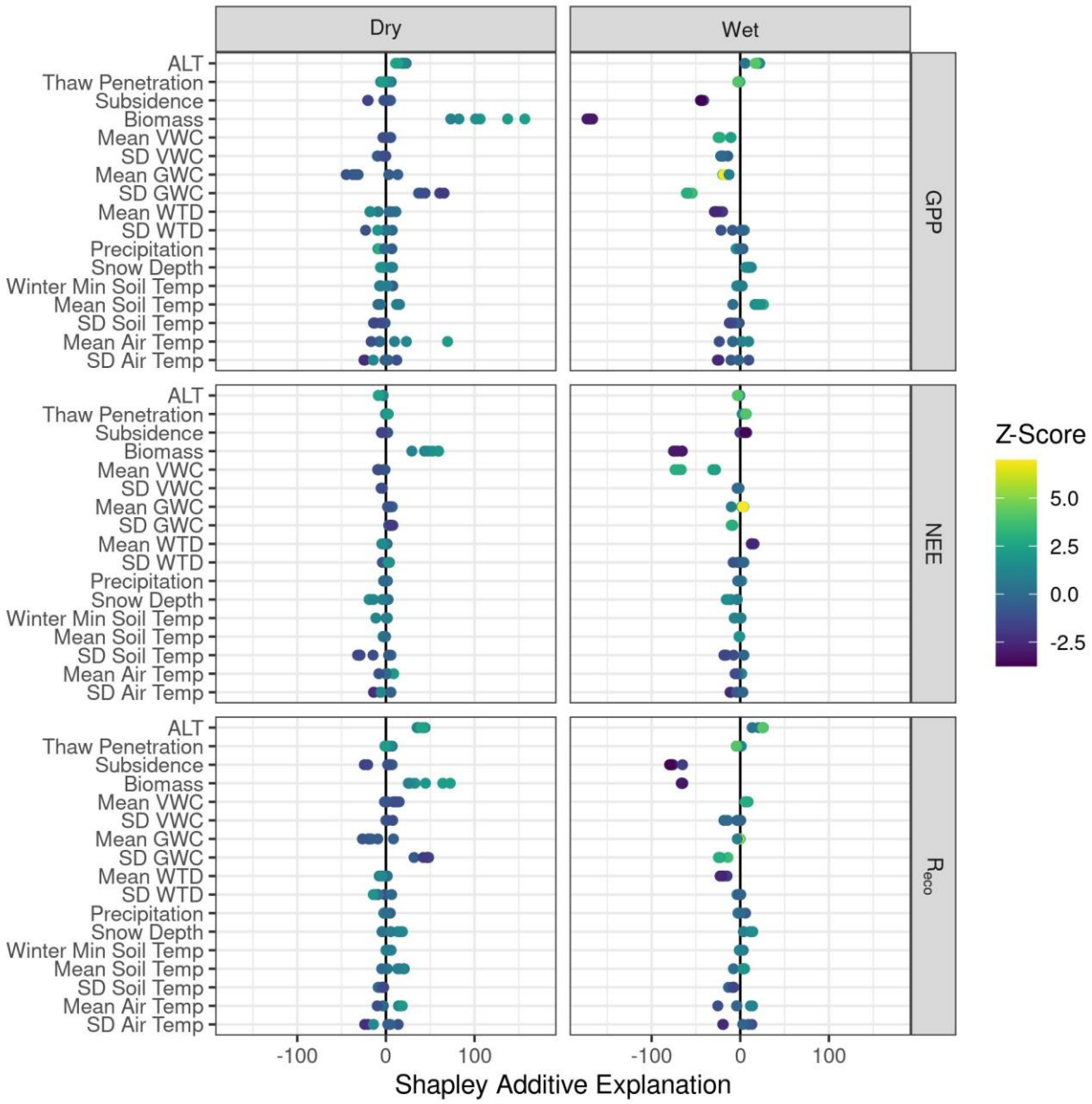

Figure S8. Shapley additive explanation values for cumulative GS fluxes in a deeply thawed and dry (Dry) plot and a deeply thawed and wet (Wet) plot for the years 2016-2021. Shapley values indicate the importance of each variable in a GBMs prediction for a single response value. Z-scores indicate the value of the explanatory variable for that observation.